Doctoral (Ph.D.) Dissertation

Egon Kecsenovity

Photoelectrochemistry of nanocomposite electrodes for the generation of solar chemicals

SUPERVISOR:

Dr. Csaba Janáky

Associate Professor

University of Szeged
Faculty of Science and Informatics
Department of Physical Chemistry and Materials Science
Doctoral School of Chemistry

2022

TABLE OF CONTENTS

LIST OF ABBREVIATIONS

BID – dielectric barrier discharge ionization detector

CB – conduction band

CNT – carbon nanotube

E_{BG} – bandgap energy

E_{CB} – conduction band edge energy

E_F – Fermi-level energy

E_{VB} – valence band edge energy

EIS – electrochemical impedance spectroscopy

EQE – external quantum efficiency

FE – Faradaic efficiency

FTO – fluorine doped tin oxide-coated glass

GC – glassy carbon

GC-BID – gas chromatograph coupled with a barrier dielectric discharge detector

GC-MS – gas chromatograph coupled with a mass spectrometer detector

GO – graphene oxide

GR – graphene

IPCE – incident photon-to-current-conversion efficiency

ITO – indium doped tin oxide-coated glass

MWCNT – multi-walled carbon nanotube

PEC – photoelectrochemical

PL – photoluminescence

RHE – reversible hydrogen electrode

rGO – reduced graphene oxide

SC – semiconductor

SEM – Scanning electron microscopy

SHE – standard hydrogen electrode

TEM – Transmission electron microscopy

VB – valence band

XPS – X-ray photoelectron spectroscopy

XRD – X-ray diffraction

3D-GR – 3D graphene foam

LIST OF FIGURES

1. INTRODUCTION

Only by covering an area four times the size of Hungary (approximately 300,000 km^2) with solar panels in the sunniest part of the world, in the Sahara Desert (which is 92 times the size of Hungary), we would be able to supply the entire world with energy in 2021. This is because Sun delivers around $1.2 \cdot 10^5$ terawatts of solar energy to Earth, which is about 7000 times more than the entire human population produces (currently approximately 18 terawatts) [1,2]. Also sunlight is one of the most valuable resources in the diversified and sustainable renewable energy supply field [3,4]. However, even if such a solar power plant were to be built, the energy produced there would have to be stored somehow and transferred from there to the rest of the world. The generated electricity can be stored in batteries or used to produce useful chemicals or fuels.

The energy of sunlight can also be converted directly to chemicals (without solar panels), to which the oldest, best-known example is photosynthesis, developed to perfection by Nature during the past billion years. Inspired by Nature, researchers created methods, called artificial photosynthesis, which also aims to convert solar energy to useful products, but using totally different approaches and man-made materials [5]. Two major methods are photocatalysis and photoelectrochemistry, which latter constitutes the topic of this dissertation.

Photoelectrochemical (PEC) procedures are based on photoelectrodes, where the charge carriers are generated in a semiconductor (SC) by light excitation, and these photogenerated charge carriers can drive the chemical conversion of the reactants to products on the surface of the electrode. The energy of the incoming light therefore can be stored in the resulting product molecule. PEC procedures have several advantages over photocatalysis: i) the SC nanoparticles can be immobilized on an electrode surface, ii) the two half reactions are isolated (by a membrane) in a typical PEC setup (**Fig. 1**), therefore products form separately and iii) the recombination of the photogenerated charge carriers can be suppressed by applying a small external bias, thus increasing the conversion rate of the substrate(s) to products [6].

Depending on whether an oxidative or reductive chemical reaction is desired, a photoanode (n-type SC) or a photocathode (p-type SC) can be employed (**Fig. 1**). However, as we will presented in this dissertation, making a well-functioning photoelectrode is not so simple.

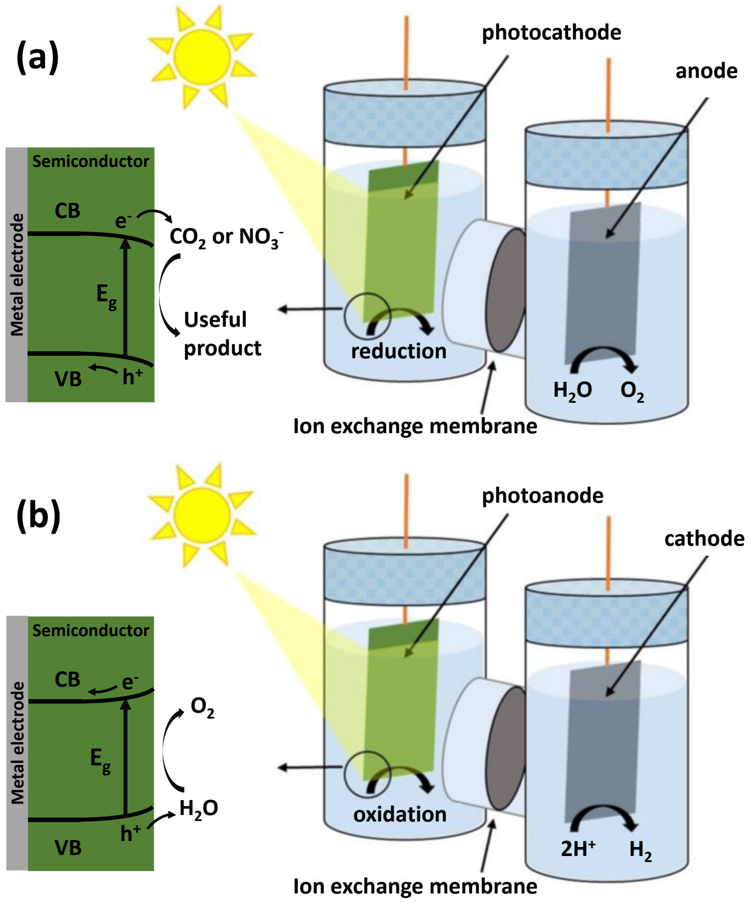

Fig. 1: Two type of solar PEC energy conversion: (a) reduction on p-type SC based photocathode (e.g., CO_2 or NO_3^- reduction), (b) oxidation on n-type SC based photoanode (e.g., O_2 evolution or organic waste oxidation). Also shown in the picture is a typical two-compartment cell, separated by an ion-exchange membrane (own illustrations).

The main and most widely studied half reactions include H^+-reduction (hydrogen evolution reaction, HER), water oxidation, and the reduction of CO_2 to various chemicals, such as CO, C_2H_4, CH_4, HCOOH, CH_3OH, and other alcohols [7]. Reactions to neutralize harmful substances (such as the reduction of nitrate ion (NO_3^-) to less harmful substances) have also come to the forefront in recent years [8,9]. Aspirations in this scientific field are directed to find photoelectrode materials which can be used to drive these reactions efficiently and cost-effectively, and in the long term, ultimately opening an avenue to industrial applications. The present work focuses on the synthesis of this type of new materials, and the investigation of their PEC properties along with their applicability as photoelectrodes in solar fuels and chemicals generation processes.

2. LITERATURE BACKGROUND

2.1 Challenges of photoelectrochemical CO_2 and NO_3^- reduction

The CO_2 molecule is thermodynamically stable and inert (the C=O binding energy is 750 kJ/mol) [10]. Its transformation into other high-energy chemicals, for example, CO, CH_4, HCOOH and CH_3OH, etc. [11,12] typically requires a significant energy input. This includes a high activation energy investment, which translates to high overpotential in electrochemistry. These processes are *multi-electron* in nature (e. g., it requires 8 electrons to reduce CO_2 to methane gas), and typically proceed through multiple *proton-coupled electron transfer reactions*. The formal electrochemical redox potentials for various CO_2 reduction reactions are presented in **Table 1**, the values are given at pH = 7.0, vs. the standard hydrogen electrode (SHE). The formal electrochemical redox potential values $(E^{0'})$ of these are very close to each other, which often results in a mixture of products in the process. However, this is mostly undesirable, as product components must be separated for further use. [13] Multi-electron reduction of CO_2 can be driven at moderately negative potentials (e.g., $E^{0'} = -0.53$ V vs. SHE at pH = 7.0 for the formation of CO, see in **Table 1**), but on the other hand, more negative potential is needed for the one-electron reduction of CO_2. This can be a problematic factor mostly in the case of metal electrodes, where $CO_2^{\cdot -}$ often forms as an intermediate [14]. This very negative formal potential is because of the stability of the CO_2 molecule. It requires the investment of a large-amount of energy to change the hybridization of the central carbon atom from sp^2 to sp^3 [15], and to shift the CO_2 molecule from a very stable linear structure to an unstable, tensed one.

Table 1: Formal electrochemical redox potentials ($E^{0'}$) for the reduction of CO_2 and H^+ in aqueous media (pH = 7.0 vs SHE) [11,12].

#	Reduction reaction	$E^{0'}$/V (vs. SHE)
1	$CO_2 + e^- \rightarrow CO_2^{\cdot -}$	−1.90
2	$CO_2 + 2H^+ + 2e^- \rightarrow HCOOH$	−0.61
3	$CO_2 + 2H^+ + 2e^- \rightarrow CO + H_2O$	−0.53
4	$CO_2 + 4H^+ + 4e^- \rightarrow HCOH + H_2O$	−0.48
5	$2H^+ + 2e^- \rightarrow H_2$	−0.41
6	$CO_2 + 6H^+ + 6e^- \rightarrow CH_3OH + H_2O$	−0.38
7	$2CO_2 + 8H_2O + 12e^- \rightarrow C_2H_4 + 12OH^-$	−0.34
8	$CO_2 + 8H^+ + 8e^- \rightarrow CH_4 + 2H_2O$	−0.24

While generation of hydrogen from water and conversion of CO_2 still dominates the PEC field, there are other avenues to explore [16]: Disinfection of water and air, removal of organic and inorganic contaminants from water and biosensing are a few among them. Reduction of nitrate ions is another subject of this research area because the high content of nitrate ions in fertilizers easily contaminate surface and groundwater.

The existing methods for nitrate removal are ion exchange, reverse osmosis, and electro-dialysis, but these processes have limitation due to their expensive operation and subsequent disposal problem of the generated nitrate waste brine. Chemical-based denitrification includes a few steps, where reduction of nitrate to nitrite is considered as the rate determining step of the whole process, and the nitrite is further reduced to N_2, and/or ammonia depending on the selectivity of the catalyst. Thus, promoting this rate determining step can led to the alternate ways of nitrate reduction.[8,17] Though photocatalysis and electrocatalysis have been already applied in this area, both approaches have their own limitations.[18,19] There are only a few reports on well worked PEC nitrate reduction, based on p-$GaInP_2$ [9] and Si [8]. p-$GaInP_2$ photoelectrode exhibited high PEC activity (10 mA cm^{-2} and high Faradaic efficiency (FE) of 80 %) in converting nitrate to nitrite, however p-$GaInP_2$ electrodes have high cost and require complicated fabrication process. Affordable Si photoelectrode also generated high current density (17 mA cm^{-2}) and showed 65 % FE in nitrate reduction, although with limited stability. Furthermore, the parasitic HER is an issue to be solved in most of the cases [20,21] in the electrochemical and PEC nitrate reduction.

In light of these difficulties there are several requirements that a good photoelectrode material must fulfill *simultaneously* [22]:

- *The bandgap* has to be narrow enough to effectively utilize a broad range of solar spectrum, but wide enough to avoid the fast recombination of the photogenerated charge carriers.
- *Band edge positions* should be optimal to drive the desired redox processes.
- Good chemical-, electrochemical- and photo*stability* over the desired or a wide pH-, and potential window.
- *Facile charge transport,* which ensures that most of the photogenerated charge carriers can be extracted both toward the electrode/electrolyte junction and toward the back contact, without excessive recombination. This means, that the higher the mobility of the photogenerated electrons and holes inside the photoelectrode, the higher the harvested photocurrent.

- *Facile charge transfer* from the SC/liquid junction to the substrate molecules: the thermodynamic criteria only provide appropriate band positions and bandgap. There is a vital kinetic criterion since these investigated reactions are multi-electron in nature.
- High *selectivity* towards the formation of the targeted products.
- Low *toxicity*, which is also strongly related to chemical stability.
- Reasonable *production cost* and not a very complicated *production method.*

One single material, however, according to best of our current knowledge, cannot meet all these criteria. For this reason, the scientific attention shifted to composite materials to reach this goal. In these hybrid systems, each constituent has a well-defined role, potentially covering all previously listed requirements.[23]

2.2 Electrodeposition of inorganic oxide semiconductor / nanocarbon composites

2.2.1 Semiconductor electrodeposition

Unlike metal electrodeposition, which is an ancient art, SC electrodeposition has a relatively recent history dating back only to the 1970s. The variant methods for electrodepositing thin films of inorganic SCs can be categorized under: i) cathodic electrodeposition, ii) anodic deposition, and iii) multi-step strategies (e.g., metal deposition followed by anodic stripping in the presence of the second component in the electrolyte), iv) chemically assisted electrodeposition (where the oxidation state of the metal ion remains unchanged). Other more esoteric methods employing non-aqueous electrolytes and molecular precursors have more limited applicability.[24]

It is pertinent to note that in the vast majority of the cases above, the electrochemical step(s) are intimately connected with the chemical step associated with the in situ precipitation of the SC on top of the support electrode. This is because the electrogenerated precursor products are most often characterized by very low solubility product (K_{sp}) values that drive the precipitation process. This is true even in the case of cathodic electrodeposition of metal oxide films which are formed in the reaction of the metal-ions with the electrogenerated hydroxide. In view of this, it should hardly be surprising that many of the solution parameters (pH, temperature etc.) have a profound influence on the dynamics of these interfacial processes. [25,26]

How do the variant methods compare in terms of versatility? In general cathodic methodologies are more versatile than their anodic counterparts in that the film thickness in the latter is controlled by mass transport restrictions through a growing film. An exception is when compact film growth is anodically disrupted by applying high voltages such that film growth now occurs in the post-dielectric breakdown regime.[27,28] When reagents such as fluoride ions (along with other electrolyte modifiers) are used, the film morphology can be tuned to assist nanotube array growth.[27,28] A minor revolution following this direction in SC electrodeposition has been the advent of approaches to grow a variety of SC nanoparticle and nanostructure morphologies (**Fig. 2**). The parallel developments in nanotechnology have undoubtedly catalyzed this corresponding growth in the allied electrodeposition discipline.

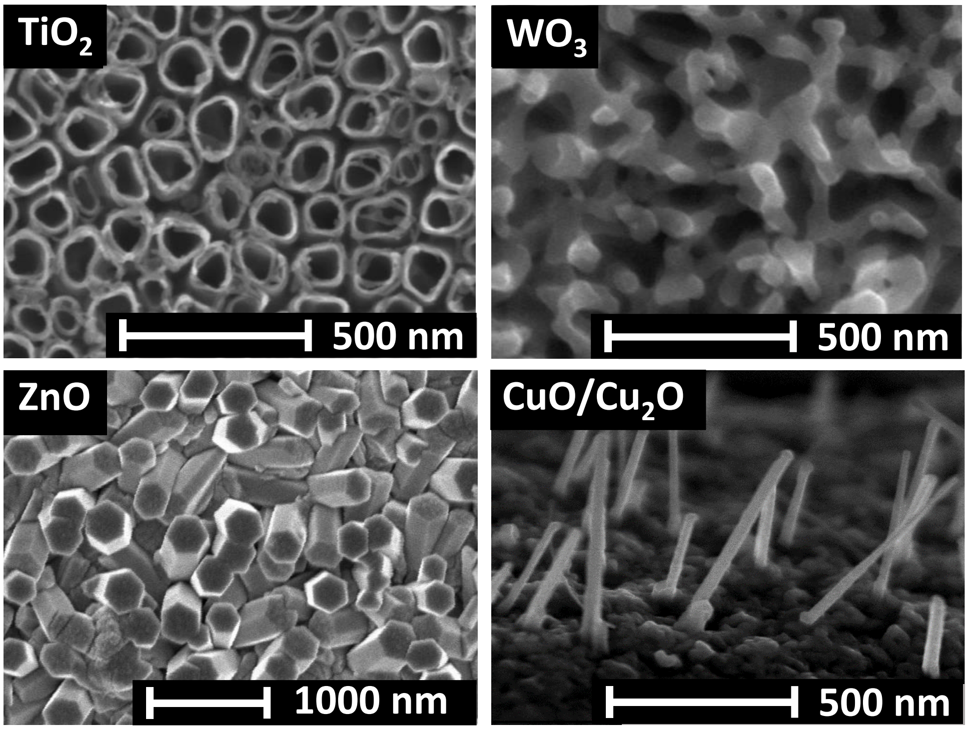

Fig. 2: Representative snapshot of advances in SC electrodeposition gained from our group earlier studies [29–31], illustrating the degree of control that is now possible on the deposited material's morphology.

The electrodeposition approach is not restricted to oxide SCs. Generally, any electronically conductive oxide (or hydroxide) may be electrodeposited by relying on high pH-induced interfacial processes. The electrodeposition of nickel, manganese, or noble metal (e.g., Ru, Ir) oxides are cases in point. [32]

2.2.2 Composition and related properties of the electrodeposited metal oxides

There is ample precedence in the literature for electrodeposition parameters (deposition potential/current, pH, electrolyte, etc.) strongly influencing the morphology of the deposited SC. Also, the possibility to precisely control the composition of a SC containing hybrid materials is among the most charming feature of electrodeposition. In most of the cases simply by changing the deposition charge the amount of electrodeposited oxide can be controlled. For example, in a study, MnO_2 was grown on MWCNTs, with increasing deposition time (2-6 min).[33] SEM images and XPS studies indicated a linear increase in the deposited MnO_2 amount. In addition, the mass-specific and areal capacitance was also determined as a function of MnO_2-loading, thus uncovering structure-property relationships for these hybrid materials. In another investigation, the electrodeposition of ZnO on carbon nanofibers was systematically studied.[34] Four different parameters were examined: 1) chemical identity of the precursor; 2) precursor concentration; 3) electrodeposition time; 4) the presence of additives. As a result, because of the variation of the hybrid composition and structure, their electrochemiluminescence properties were also varied.

The composition of the oxide component can also be controlled. For example, electrodeposition of not exactly stoichiometric p- and n-type Cu_2O was achieved on reduced graphene oxide coated polyethylene terephthalate (PET). At alkaline pH-values (e.g., pH = 9), a copper-deficient, p-type SC Cu_2O was formed, while the formation of n-type semiconducting Cu_2O was witnessed at neutral pH-values.[35] As amplified here, minor changes in the composition cause major differences in the electronic properties, which determine the applicability of the electrodeposited material in various energy oriented reaction schemes. In this study, compositional change was also coupled with a change in the crystal structure: while the p-type Cu_2O exhibited a pyramidal shape, this morphological feature was much less pronounced for the n-type oxide. This study also highlighted the effect of current density on the dominant crystal facet,[35] as it was also demonstrated for Cu_2O electrodeposited on conventional substrates.[36]

The above shown compositional and structural changes are often coupled with the alteration of the optical and electronic properties of the electrodeposited SCs. For example, the electronic properties of n-type semiconducting Cu_2O were tailored via controlling the Cl^- ion content of the electrodeposition solution.[37] As deduced from the recorded Mott-Schottky plots, the charge carrier concentration was varied within a range of over two orders of magnitude.[37]

In summary, the main charm of electrodeposition is rooted in the wealth of properties (both physical and chemical) that can be tailored for a targeted application. However, it is pertinent to underline that many of these materials attributes are not independent of one another (e.g., crystallinity and morphology have a deep influence on the electronic conductivity of the material). This further highlights the importance of careful adjustment of the electrosynthetic conditions. Finally, if the non-carbon component of a nanocomposite is a SC, the synthetic scope is further expanded by the ability of this component to prepare photoelectrodes from it.

2.2.3 Carbon nanomaterials as electrode supports

Application of nanocarbons as electrode support materials is a complex topic, especially because many fundamentally different aspects have to be considered. For example, in the case of carbon nanotubes (CNTs), their type (SWCNT or MWCNT), the purity (i.e., the presence of residual metal catalyst nanoparticles), number of defects, the electrode preparation process, all affect the electrochemical behavior.[38] The electrochemistry of graphene (GR) has also been reviewed,[39] and it was found that the rate of heterogeneous electron transfer does not solely depend on the electrode reaction, but also on the quality of GR. In this vein, the amount of defects, functional groups, and impurities present on the GR sheets are all of prime importance.[39] This is especially important because in most of the studies, the materials are obtained by the chemical exfoliation of graphite (Hummers method),[40] and subsequently reduced to a variable extent. Graphene oxide (GO), has a C/O ratio of ∼2 and a subsequent reduction step can increase this ratio up to the range of ∼3-15.[39]

Simply from an electrical conductivity perspective, CNTs have significantly different properties based on their structure (SWCNT or MWCNT) and even the configuration for SWCNT (armchair, zigzag, and chiral). Depending on these attributes, the CNT can behave as a metal or as a SC. Crystallographic defects (e.g., atom vacancies) together with different functional groups, complicate the behavior even further. For example, the electrical conductivity of reduced graphene oxide (rGO) spans a broad range between 0.5 to 10000 S m^{-1} depending on the degree of reduction (i.e., the ratio of the graphitic regions (sp^2) to oxidized regions (sp^3)).[41] It was also demonstrated that if the sp^2 fraction is increased over 0.9, the conductivity of rGO can be close to that of pristine GR.[42] Additionally, the film thickness (the number of GR layers) also affects the rate of electron transfer, as demonstrated for different model redox processes.[43] Finally, notably different electrical conductivity values can be obtained for the same carbon allotrope, depending on the form of the studied sample (compact pellet, paper, isolated single particle).[44] Indeed, many of the differences reported in the literature may well be rooted in the variation of the electrical properties of the employed nanocarbon template (see a few examples in **Table 2**).

Beyond the electrical conductivity, the actual surface area (or equivalently, the surface roughness factor) is another important factor to consider when choosing a suitable electrode material. Electrochemical impedance spectroscopy (or even cyclic voltammetry) can provide a rapid assessment of the electrochemically active surface area via measurement of the double-layer capacitance of the nanocarbon/electrolyte interface. The roughness factor can drastically differ depending on the preparation of the modified electrode. Spray-coating, spin-coating, or drop-casting are all viable options to obtain either a film or a 3D nanostructure on an inert electrode surface. Ordered structures of CNTs or GR are even more attractive alternatives. In the case of these self-standing and self-supporting materials no additional supporting electrode is needed: the self-supported films of the carbon nanomaterials are themselves deployed as the working electrode.[45,46] In such superstructures however, the electronic properties may be dominated by the interfaces between the individual nanoobjects, and thus be massively different.

Table 2: Comparison of the most important properties of various nanocarbon electrode materials.

Type of carbon	**Surface area (m^2 g^{-1})**	**Electrical conductivity (S m^{-1})**	**Other features**	**Ref.**
SWCNT	Up to 1200 (typically 400-800)	Up to 10^6 for metallic	Can be metallic or semiconducting, based on the configuration.	[47]
MWCNT	50-800 (typically 100-300)	Up to 10^5	The specific surface area decreases drastically as the wall-number increases	[47,48]
GR	Up to 2600	Up to 6x10^5	For bulk samples, however, graphite shows higher electric conductivity.	[44]
GO	Typically 600-900	~0.02	Very low electric conductivity, due to the wealth of O-functions.	[41,42]
rGO	Typically 600-900	Up to 10^4	The achieved electrical conductivity depends on the sp^2/sp^3 ratio of the carbon atoms.	[41,42]
Carbon black	Up to 900	100-200	It has a less ordered structure and can be produced in bulk quantities.	[49]

Long range alignment of CNTs or GR flakes offers further application-oriented research avenues, stemming from the unique anisotropic properties (e.g., electronic conductivity) of these materials. For example, in a study, one of my colleagues demonstrated a possible route for homogeneously infiltrating an organic SC (conjugated polymer) into macroscopic arrays of vertically aligned MWCNTs via electrodeposition.[50] These composite materials showed a huge anisotropy in the thermal and electrical properties.

2.2.4 Electrodeposition of metal oxide/carbon-nanotube and metal oxide/graphene composites

The cardinal rule in the development of any composite or hybrid material is that its properties have to be superior to those of its components. In this regard, carbon nanomaterials have a unique set of properties which makes them attractive candidates for mating with inorganic SCs. Large surface area, high electronic conductivity, mechanical robustness, the ease of chemical modification, and earth abundancy all facilitate applicability of the resultant nanocomposites for energy conversion devices. Electro- or photocatalytic deposition of metal nanoparticles is a well-established route for preparing carbon-metal nanocomposites[51,52] especially on carbons that are routinely employed for fuel cell applications such as carbon blacks. On the other hand, electrodeposition of inorganic SC (or conductive oxide) nanoparticles and films on morphologically ordered *nanocarbon* supports is only now evolving and forms a central theme for this dissertation. This trend is somewhat surprising considering that electrodeposition is a well-established methodology for preparing thin films of many SCs (e.g., TiO_2, Cu_2O, and Fe_2O_3). **Fig. 3** provides a snapshot of the parallel growth of interest in SC electrodeposition and SC/nanocarbon hybrids. Interestingly, while SC electrodeposition is now a rather mature area with an approximately linear growth in the number of publications, the field of hybrid materials is undergoing a nearly exponential development.

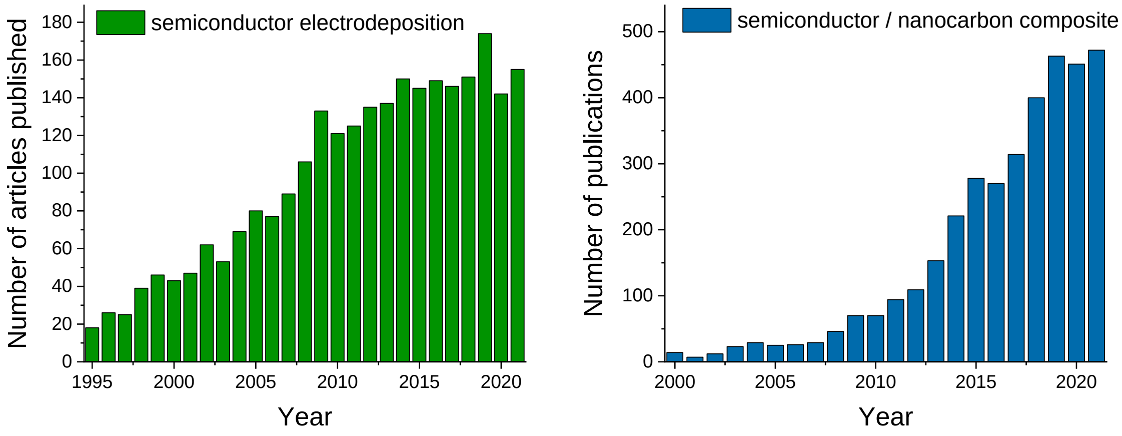

Fig. 3: Results from a literature survey using the ISI Web of Knowledge database on the number of articles published on SC electrodeposition, and on the SC/nanocarbon hybrid materials in general.

One of the most typical examples of oxide electrodeposition is the formation of ZnO in a CNT matrix. Note that the oxidation state of the metal ion does not change; the oxide-hydroxide deposition is sustained by proton consuming electrochemical reactions, which increase the local pH [32] (e.g., reduction of dissolved O_2). As another example of cathodic deposition, ultralong CNTs were coated on TiO_2 via slow potentiostatic electrodeposition followed by thermal treatment to obtain anatase.[53] **Fig. 4** demonstrates the evolution of the nanocomposite structure, where the parallel nature of the nanotubes is maintained in the hybrid configuration. Prior to electrodeposition, the as-prepared CNTs were electrochemically activated to improve their hydrophilicity. This provides added advantages for the candidate material in various applications.[53] As an example of the two-step strategy, Cu nanoparticles were first deposited on MWCNTs employing a constant negative potential; they were subsequently transformed to CuO via potential cycling.[54]

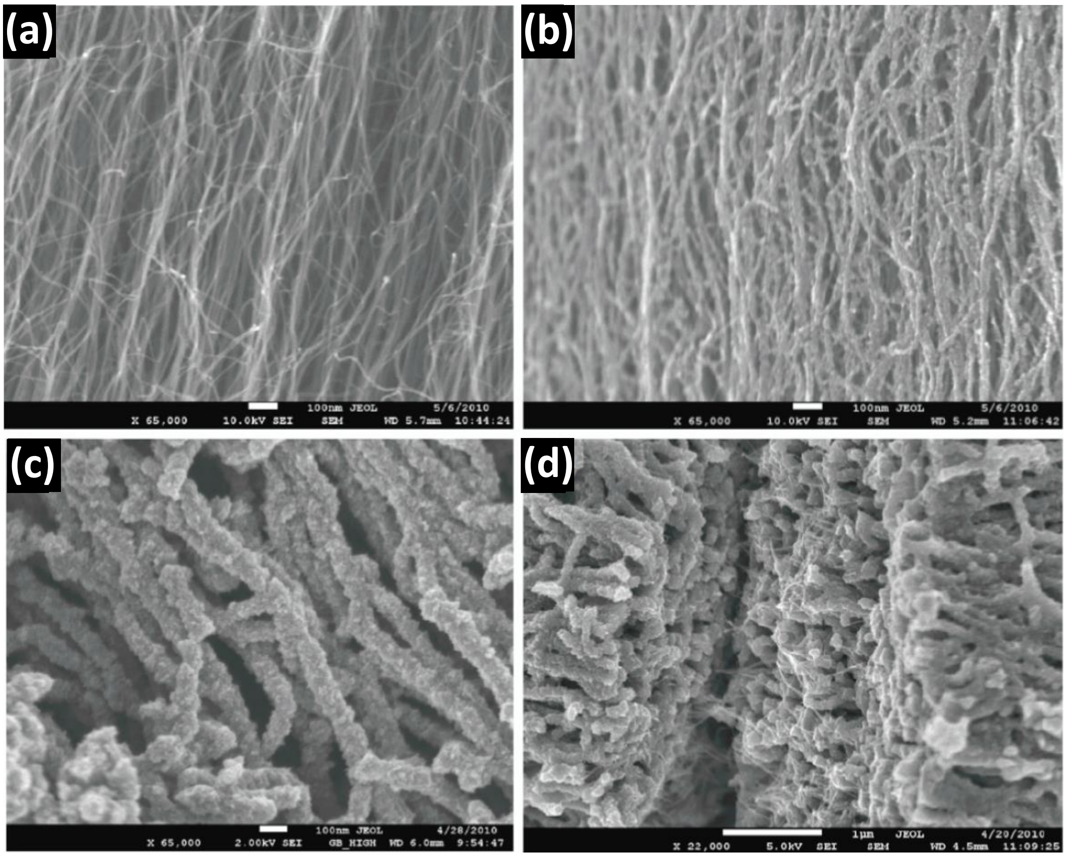

Fig. 4: SEM images of super-long CNT arrays after electrodeposition of TiO_2 for different times: 0 min (a), 5 min (b) and 15 min (c), and a cross-section view of (c) broken deliberately (d). [53]

Table 3 provides a compilation of selected examples of electrodeposited inorganic oxide/CNT composites and their applications. In most cases, oxide SCs were one of the components; however, MnO_2 has also been a popular candidate because of its large charge storage capacity. Other oxides/hydroxides such as Co or Ni compounds, that are not SCs, have been studied from a sensor perspective. As for the employed electrosynthetic strategies, both dynamic and static methods were employed. [33]

Table 3: Selected examples of electrodeposited inorganic oxide/CNT assemblies.

Carbon	Oxide	Electrosynthesis method	Application(s)	Ref.
CNT paper	MnO_2	Potentiodynamic cycling	Supercapacitor	[55]
MWCNT array	MnO_2	Potentiostatic anodic deposition	H_2O_2 sensor	[56]
Graphenated CNTs	MnO_2	Potentiodynamic cycling	Supercapacitor	[33]
MWCNT array	CuO	Two step electrochemical procedure (Cu nanoparticle electrodeposition is followed by electrooxidation)	Glucose sensing	[54]
MWCNT array	CoO/ $Co(OH_2)$	H_2O_2-assisted electrodeposition	Glucose sensing	[57]
MWCNT array	Cu_2O	Multi-step potentiostatic electrodeposition	Li-ion battery	[58]
MWCNT array	MnO_2	Potentiostatic/galvanostatic	Supercapacitor	[59]
MWCNT	MoO_x	Potentiodynamic cycling	Bromate detection	[60]
SWCNT	NiO	Electrochemical co-deposition	NO-sensor	[61]
MWCNT	Ti-Fe_2O_3	Electrochemical co-deposition	PEC water splitting	[62]
MWCNT	TiO_2	H_2O_2-assisted potentiostatic electrodeposition	Photodetector, sensing	[53]
MWCNT	ZnO	Potentiostatic electrodeposition	Optoelectronics	[63]
MWCNT	ZnO	Potentiostatic electrodeposition	Amperometric sensing	[64]
Carbon fiber	ZnO	Potentiostatic electrodeposition	Optoelectronics	[34]

Table 4 provides a compilation of selected examples of SC/GR nanocomposites that have been prepared by electrodeposition. In the vast majority of cases in **Table 4**, GO was synthesized from graphite powder by the Hummers' method. [40] During the cathodic electrodeposition, GO gets electroreduced in situ to rGO. Interestingly, in one study, [65] the deposition sequence was reversed from the usual one of electrodepositing the oxide phase on top of the GR layer. Thus, the GR film was cathodically electrodeposited instead on the TiO_2 nanotube array. The residual oxygen-containing groups on the electrodeposited GR film were subsequently removed by photo-assisted reduction of the underlying TiO_2 nanotube array layer.

Table 4: Selected examples of electrodeposited inorganic oxide/GR assemblies

Carbon	Oxide	Electrosynthesis method	Application(s)	Ref.
rGO	TiO_2 nanotube arrays	GO was electroreduced from a dispersion to form rGO/TiO_2 nanotube array hybrid.	Photocatalysis	[65]
3D graphene	$Co(OH)_2$/ Co_3O_4	Co_3O_4 nanosheets were grown on N-doped GR foam	Supercapacitor	[66]
GR	MnO_2	GR film first prepared on stainless steel substrate by electrophoretic deposition. The oxide was subsequently anodically deposited on it.	Supercapacitor	[67]
GR coated textile microfibers	MnO_2	Galvanostatic deposition.	Supercapacitor	[68]
rGO on silane-modified polyethylene terephthalate.	ZnO nanorods, Cu_2O	Both oxides cathodically grown on GR film by base electrogeneration.	Flexible photovoltaic solar cell	[35]
rGO on SiO_2 substrate	Cl-doped Cu_2O	Potentiostatic deposition from $CuSO_4$/$CuCl_2$ solution	-	[37]
rGO supported on quartz	ZnO nanorods	Oxide cathodically grown by base electrogeneration.	Photovoltaic solar cell	[69]
rGO supported on GC	ZnO flower-like structures	Oxide cathodically grown from nitrate bath.	Amperometric H_2O_2 sensor	[70]
GR support on Cu foil	ZnO NTAs	Same method as above.	Transparent optoelectronic devices	[71]
GR on SiO_2/Si substrate	ZnO nanostructures	Same method as above.	Same as above	[72]
Electrodeposited GR	ZnO	ZnO nanoparticles were grown via potentiodynamic cycling on electrodeposited GR.	Acetaminophen and phenacetin sensor	[73]

In general, nanocarbons enhance the electronic, mechanical, and thermal properties of the composite by their presence. In addition, materials such as GR impart good optical transparency that makes the overall composite to be adaptable to many optoelectronic applications. Another very useful attribute of nanocarbons is their excellent electron acceptor property in redox scenarios; the injected electrons rapidly delocalize in the electronic manifolds of the nanocarbon matrix. [52,74]

2.3 Photoelectrode materials

As we have seen so far, plenty of combinations can be formed using various SC materials with different nanocarbons, which can be also used in many fields. In what follows, I would like to narrow the literature, focusing on the materials I used in my doctoral work, in particular to demonstrate their PEC properties.

2.3.1 Cu_2O based photoelectrodes

Since my supervisors proof-of-concept studies on the solar photoelectrosynthesis of methanol using hybrid CuO/Cu_2O nanorod arrays, [30,75] different laboratories employed p-type Cu_2O as a photocathode material in CO_2 reduction. [76,77] In addition, further progress has been achieved in terms of (i) analyzing the potential dependent product distribution,[78] (ii) realizing the reaction in a continuous-flow reactor, [79] and (iii) gaining mechanistic understanding of CO_2 adsorption using quantum chemical calculations. [80] The instability of Cu_2O towards PEC corrosion (i.e., metallic copper formation), however, was already found to be a major problem in earlier reports on PEC water splitting using this material. [37,81] Application of surface coating was demonstrated as a possible strategy to increase photoelectrode lifetime, either by employing a carbon coating [81] or via atomic layer deposition of Al-doped ZnO and TiO_2 nanolayers [82,83], or by over-coating with tungsten carbide and carbide-derived carbons. [84] Employing a surface coating on the Cu_2O surface however, is not necessarily useful in CO_2 reduction, where Cu atoms on the surface play a specific catalytic role in the reaction as was shown in different electrocatalytic reaction schemes. [85]

In addition to instability, two other factors: namely, surface area and charge carrier mobility, are also critical issues limiting the performance of the photocathodes. To address the above challenges together as a whole, nanostructuring of the electrode may offer a viable avenue of solve these problems. [86] Inorganic SC/nanocarbon hybrids offer a promising platform in this regard, by uniting the high electrical conductivity of the carbon component with the photoactive behavior of the inorganic material. [87] There are different studies in the literature, proving the above concept in both binary [88] and ternary hybrid configurations. [52,74] As for Cu_2O specifically, it has been combined with both carbon quantum dots [89] and rGO sheets [90] recently, to perform the photo-driven (sometimes also referred as photocatalytic) reduction of CO_2 to fuels.

To the best of our knowledge, before the work presented in this dissertation, there was no precedence in the literature at that time, where Cu_2O/nanocarbon hybrids were employed as photocathodes in a PEC cell for CO_2 reduction.

2.3.2 TiO_2 based photoelectrodes

Even several decades after the first reports on its photocatalytic and PEC properties,[91] titanium dioxide (TiO_2) is still one of the most intensively studied SCs for photo(electro)catalytic applications. Because of its high photoactivity (although restricted to the UV-region of the solar spectrum) and (photo)chemical stability, it has been frequently employed in photocatalytic processes, PEC water splitting, as well as in dye-sensitized and perovskite solar cells.[92,93] Different synthetic protocols have been developed to obtain high-quality TiO_2 with controlled structure, doping level, and crystal phase composition. These include hydrothermal/solvothermal synthesis, [94] sol–gel method, [95] and flame pyrolysis [96]. To achieve high crystallinity, the synthesis usually employs high temperatures as well. To apply the nanoparticles as a thin film within solar or PEC cells, they must be transferred to a conductive substrate. This transfer is usually carried out by a physical method (e.g., spray-coating or spin-coating), followed by a long sinter step at an elevated temperature. This thermal treatment aims (i) to enhance the adhesion of the film to the underlying support and (ii) to improve the electronic connectivity among the nanoparticles (NPs). However, this prolonged heat exposure, might result in unintended NP aggregation and fusion. In summary, these methods are both time- and energy-consuming; therefore, there is a strong need for green, sustainable and sophisticated synthetic approaches which at the same time can control the properties of such materials with high precision and reproducibility. [97,98]

One-step methods, such as electrochemical deposition, where TiO_2 forms directly on the substrate, are very attractive. [29] Different studies published on the electrochemical deposition of TiO_2 always involve two steps. First, a Ti(IV) oxide/hydroxide layer is formed on the electrode surface by either electrochemical oxidation and hydrolysis of a Ti(III) precursor,[99,100] or by the electrochemical hydrolysis of a Ti(IV) precursor. [101] The *crystalline* TiO_2 is typically formed in a subsequent thermal anneal step. It was demonstrated recently that the amorphous electrodeposit can be turned into crystalline anatase by long-term aging of the electrodes at 80 °C in an ammonium fluoride solution. [102] Although these approaches consist of multiple steps, they do demonstrate the most important benefits of electrochemical deposition techniques in the case of TiO_2: (i) control over the thickness and morphology of the layer, (ii) the possibility to homogeneously coat rough and complex-shaped surfaces (iii) direct formation of the layer on the conductive substrate (iv) intimate connection between the supporting electrode material and the deposited layer.

There is one example on the low-temperature, solution-phase synthesis of TiO_2 *nanocrystals* in the literature, [103] where O_2 gas was introduced into the aqueous solution of $TiCl_3$ precursor. Surprisingly, one-step, direct electrochemical deposition of crystalline TiO_2 was only reported in one isolated occasion. [104] In this study, the authors were able to deposit crystalline rutile from an aqueous $TiCl_3$ solution using sodium dodecyl sulfate as a structure-directing agent. Although the product was partly crystalline, an additional anneal step was necessary to generate reasonable photoactivity.

Immobilizing (not with electrodeposition) TiO_2 on GR or CNT substrates led to notably improved PEC activity, compared to the regular TiO_2 films.[105,106] As the conductivity of the anode is a decisive parameter in Li-ion batteries, TiO_2/nanocarbon composites are also attractive candidates for this application. [107]

2.3.3 Fe_2O_3 based photoelectrodes

One of the most extensively studied n-type SC photoelectrodes is hematite (α-Fe_2O_3 denoted as Fe_2O_3 in the followings), due to its narrow bandgap (E_{BG} = 2.0–2.2 eV), and appropriate valence band (VB) position to drive the PEC water oxidation process. [108,109] Additionally, it is non-toxic, abundant, and stable in alkaline solutions. [110,111] Although, a maximum of 16.8% solar-to-hydrogen conversion efficiency can be calculated from the bandgap,[108,112] real device performances are still far behind.[113] The low charge carrier mobility (< 1 cm^2 V^{-1} s^{-1}), [110] and short charge carrier lifetime[112] together result in small charge carrier diffusion length (2–4 nm). [114] This means that the majority of photogenerated charge carriers are lost before they could reach the substrate in the electrolyte solution. On top of this, low absorption coefficient [115] and sluggish water oxidation kinetics further limits the efficiency of the overall PEC process.

Several strategies have been employed to overcome these issues, among which doping and nanostructuring are the two most prominent. For example, doping of Fe_2O_3 with various elements – such as Si, [116] Ti, [110] Mo [117] and Sn [118] – can significantly increase the charge carrier mobility and concentration. Nanostructured hematite architectures improved the relative volume of the space-charge layer in comparison to the bulk, which resulted in reduced charge carrier recombination and thus in higher photocurrents. [119]

There are a few examples, where Fe_2O_3 was combined with nanocarbons, such as rGO, [120,121] GR, [109,122] CNTs[88] and carbon quantum dots [123]. Interestingly, in most of these studies, the nanocarbon component is located on top of the Fe_2O_3 layer, [109,120,121] thus the enhanced PEC behavior is rooted in the passivation of the surface states of Fe_2O_3 by the nanocarbon overlayer. The sluggish water oxidation kinetics can be alleviated by the deposition of co-catalyst overlayers such as Co-Pi [114], FeOOH, [124] NiOOH, [125] $NiFeO_x$, [126] IrO_2 [119]. Notably, the term "co-catalyst" is used in a broader sense here, as a surface layer that helps to improve the performance of the photoelectrode. Its contribution can be either accelerating the kinetics of the water oxidation reaction; or the passivation the surface states suppressing recombination. Irrespective from the mechanism, both of these contribution results in higher photocurrent density compared to the pristine SC counterpart. As a result of the complex structural-, and surface modifications, PEC performance of hematite photoelectrodes has been greatly improved over the years. The state-of-the-art systems are presented in **Table 5**.

Table 5: PEC performance of state-of-the-art hematite photoelectrodes and PEC performance of the best electrodeposited hematite photoelectrodes.

Name	**Synthesis method**	**Photocurrent density**	**IPCE (λ = 500 nm)**	**Ref.**
α-Fe_2O_3 nanorods with TiO_2 overlayer and Co-Pi catalyst	Chemical bath deposition	6 mA cm^{-2} at +1.23 V vs. RHE in 1 M KOH, 100 mW cm^{-2} AM 1.5G	≈ 5%	[127]
Ru-doped α-Fe_2O_3 nanorods	Doctor blading	5.7 mA cm^{-2} at +1.23 V vs. RHE in 1 M NaOH, 100 mW cm^{-2} AM 1.5G	43%	[128]
Interconnected α-Fe_2O_3 nanosheets with Ag NPs and Co-Pi	Anodization	4.68 mA cm^{-2} at +1.23 V vs. RHE in 1 M NaOH, 100 mW cm^{-2} AM 1.5G	≈ 10%	[129]
Nanostructured α-Fe_2O_3 with IrO_2 NPs	Atmospheric pressure chemical vapor deposition	≈ 3 mA cm^{-2} at +1.23 V vs. RHE in 1 M NaOH, 100 mW cm^{-2} AM 1.5G	≈ 22%	[119]
Nanostructured Zn-, and Ti-doped α-Fe_2O_3	Electrodeposition	1.5 mA cm^{-2} at +1.23 V vs. RHE in 1 M NaOH, 100 mW cm^{-2} 300 W Xe lamp	≈ 2.5%	[110]
Nanostructured Ti-, and Zr-doped α-Fe_2O_3 with $Co(NO_3)_2$	Electrodeposition	≈ 0.6 mA cm^{-2} at +1.23 V vs. RHE in 1 M KOH, 100 mW cm^{-2} AM 1.5G	≈ 3%	[115]

2.3.4 Metal - iodide based photoelectrodes

Metal halide SCs are considered as new class of materials with favorable combination of optical and electronic properties, and with the ease to be solution processed into films.[130,131] These SCs received particularly great attention in metal halide perovskite based solar energy conversion devices.[132–134] Among the metal halides, lead iodide (PbI_2) occupies a creditable place owing to its narrow direct bandgap of 2.3 eV,[135] long carrier life-times and high collection efficiency [136], and it is also the basis of most perovskite type metal halide materials. Another halide SC of special interest is copper iodide (CuI) because of its high hole mobility (>40 $cm^2\ V^{-1}\ s^{-1}$ in bulk).[130] CuI exist in different forms, zincblende structure below 643 K (γ-CuI), wurtzite structure between 643 and 673 K (β-CuI), and rock salt structure above 673 K (α-CuI). CuI is a direct SC, with a bandgap of 3.1-3.2 eV, already employed in PEC processes.[133,134]

There are references in the literature in which a mixture of CuI and PbI_2 has been studied, but they are contradictory. Studies published from the 1980s, but even more recently (one in 2017), show that these two substances form a common compound ($CuPbI_3$). [137–139] However, as early as the 1970s, a research team measured a phase diagram of the CuI-PbI_2 system and they found that it did not contain a mixed iodide compound. [140] We wanted to resolve this contradiction, so we started working with this system. From a PEC point of view, CuI photoelectrode is able to reduce CO_2 in aqueous media [133], however, PbI_2 is not stable because of the carbonate formation. So, we looked for another industrially relevant reaction to study the PEC performance of the individual compounds and the mixtures formed from them. In this vein a less researched area, the PEC nitrate ion reduction was chosen because both materials are stable in nitrate ion containing aqueous solution.

2.4 Charge carrier dynamics of photoelectrodes

After light excitation with larger energy than the bandgap of the SC, charge carriers are generated. These charge carriers can go through various processes such as recombination, trapping, extraction at different interfaces (**Fig. 5**). It is worth noting that after excitation these carriers cannot be considered stationary and they diffuse (or in the presence of electric field, migrate) within the material, which process is called charge carrier transport. If interfaces between different materials are also present (e.g., charge collection layers, electrolytes) the carriers can pass through this barrier, which process is termed charge carrier transfer. By accelerating both processes the photoconversion efficiency can be enhanced.

It is important to determine the fate of charge carriers at the SC/liquid interface. If the transfer of the minority carriers (electrons in the case of a p-type SC) through this interface transfer easily to the redox active species in the electrolyte, the desired PEC reactions can be efficiently driven (**Fig. 5a**). Contrastingly, if the transfer of the photoexcited electrons or holes toward the redox active species is slow, charge carriers tend to recombine or get trapped at the surface states of the SC. These surface states are typically caused by grain boundaries or by the termination of the crystal lattice at the SC surface [11]. Importantly, electron-hole recombination processes (occurring at the ps-ns timescale) are several orders of magnitudes faster than interfacial charge carrier transfer (μs-ms) processes [141], which makes PEC processes particularly challenging.

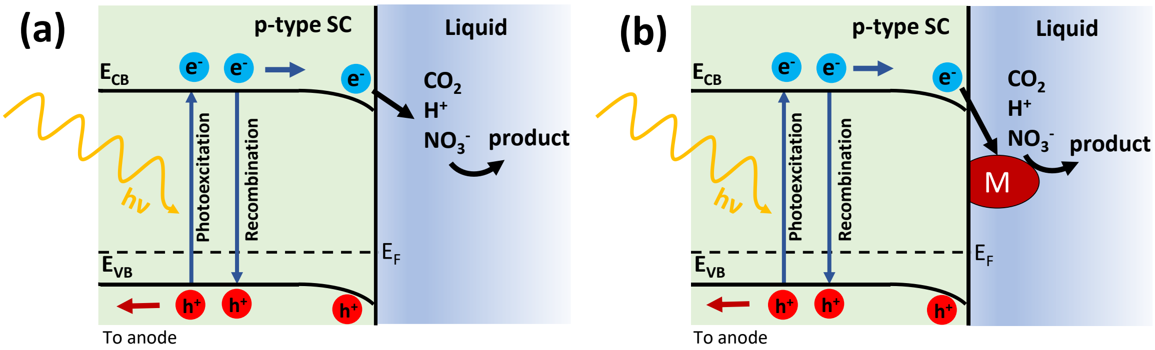

Fig. 5: Schematic diagrams of two different schemes for PEC-assisted $CO_2/H^+/NO_3^-$ reduction on a p-type SC photocathode: on a SC electrode (a), on a co-catalyst decorated SC electrode (b).[12].

Combination of a SC with a co-catalyst is a promising avenue to enhance the solar-to-chemical-conversion efficiency through improving the charge carrier transfer properties (**Fig. 5b**). In these cases, the SC only acts as a light absorber. After charge separation, the photogenerated charge carriers are transferred to the co-catalyst, where the redox processes occur. Co-catalysts can be 1) metal or metal oxide nanoparticles, 2) inorganic complexes, or 3) organic molecules, etc. Importantly, in most cases the Fermi-level of the applied co-catalyst must lie below the E_{CB} of the SC and above the redox potential of the desired reaction to act as an electron shuttle (in the case of p-type SC) [142]. One of prototypical metal co-catalyst is Pt, which is still considered as the state-of-the-art electrocatalyst for the electrochemical H_2-evolution. The effect of depositing Pt nanoparticles on a surface of a nanostructured NiO has been investigated in our research group recently [143]. Overall, twenty times increase was measured in terms of photocurrents and H_2 evolution rates, compared to the bare nanostructured NiO photocathode. This concept was applied for other

SC photocathodes utilized in PEC CO_2 reduction processes, for example p-type Si, where the surface was decorated with Cu, Ag, and Au. On the modified electrodes methane, ethylene, and carbon monoxide formed (depending on the used metal) during PEC CO_2 reduction, similarly to the pristine metal electrodes, but at approximately 0.5 V more positive potential and with higher efficiencies [144].

Low charge carrier mobility results in extensive recombination, which can be one of the main reasons behind small photocurrents. A possible solution to overcome the limited conductivity of inorganic SCs is to deposit them on a highly conductive nanostructured scaffold. Thus, the distance that charge carriers have to travel towards the solution and the current collector is reduced. Furthermore, a significant increase in conductivity can be achieved if an inherently conductive scaffold is used, as demonstrated later in the dissertation.

3. MOTIVATION AND AIMS

When I have started my PhD studies in 2016, our first goal was to ***prepare SC/nanocarbon photoelectrodes with electrodeposition to improve the charge carrier transport properties, study their PEC behavior and applicability in the PEC reduction of CO_2***. However, as time and research progressed, new issues and opportunities arose, therefore the goals of my doctoral work have gradually become clearer. These aims can be listed according to the following points:

- To **find an electrodeposition method** by which p-type Cu_2O can be synthesized on different nanocarbon electrode surfaces, including CNT networks, spray-coated GR films (using liquid-phase exfoliation few-layer GR platelets), and 3D graphene foams, thereby creating Cu_2O / nanocarbon composite electrodes for PEC CO_2 reduction. After that we aimed to uncover the **reasons behind the improved PEC performance** of nanocarbon based photoelectrodes, compared to the bare SC counterpart.
- Another goal was to create nanocarbon based photoelectrodes with an n-type SC. We first chose the well-known TiO_2, but we had to find a simple electrochemical method for the deposition of nanocrystalline TiO_2 films on GR substrates. Since we did not find one in the literature (without the post-deposition anneal), we took advantage of this opportunity, and the new **goal was to develop a simple, well-controlled, one-step TiO_2 electrodeposition method** that could be used to obtain nanocarbon-based composite photoelectrodes.
- We also aimed to study another n-type SC. **Hematite** (α-Fe_2O_3) was selected, and the **goal was to form nanocomposite electrodes via electrodeposition**. We also aimed to explore the reasons behind the improved PEC performance, and **to solve the photooxidation of the GR layer**, using an electrodeposited co-catalyst.
- Due to the contradiction in the literature, we started to study the non-nanocarbon-based CuI-PbI_2 system in nitrate ion reduction. The goal was to **find out if the bimetallic compound really exists, or just a mixture of the two iodides is present**. We also had to **find a synthesis method** to make this mixed iodide photoelectrodes. Furthermore, we aimed to answer the question **why the mixture performs better in PEC nitrate ion reduction** compared to the monometallic counterparts, and **what products form** during this process.

4. CHEMICALS AND EXPERIMENTAL TECHNIQUES

4.1 Materials

Spray-coating

- Indium tin oxide coated glass (ITO; 20 Ω/sq.; Präzisions Glas & Optik GmbH)
- Fluorine doped tin oxide coated glass (FTO; TEC15; 7 Ω/sq.; Sigma-Aldrich)
- Glassy carbon (GC; 2mm thick; Alfa Aesar)
- Graphene (GR; Premium-quality, powder, exfoliated graphene platelets, Elicarb®)
- Ethanol (C_2H_6O; $M_r = 46.07$; absolute; Sigma-Aldrich)
- Compressed air (20.5 % O_2, 79.5% N_2; Messer)

Synthesis of SC thin films and nanocomposites

- Copper-sulfate pentahydrate ($CuSO_4 \times 5H_2O$; $M_r = 249.68$; Alfa Aesar)
- DL-Lactic acid ($C_3H_6O_3$, ~90%; $M_r = 90.08$; Sigma-Aldrich).
- Anhydrous sodium-carbonate (Na_2CO_3; $M_r = 105.99$; Fluka)
- Titanium (III) chloride solution (HCl stabilized, $TiCl_3$ (12%); Sigma-Aldrich)
- Iron (III) chloride hexahydrate ($FeCl_3 \times 6H_2O$; $M_r = 270.295$; Sigma-Aldrich)
- Nickel (II) chloride hexahydrate ($NiCl_2 \times 6H_2O$; $M_r = 237.69$; Sigma-Aldrich)
- Sodium chloride (NaCl; $M_r = 58.44$; WVR),
- Sodium fluoride (NaF; $M_r = 41.99$; VWR),
- Potassium chloride (KCl; $M_r = 74.55$; VWR),
- Hydrogen peroxide (H_2O_2, 30%; $M_r = 34.015$; VWR),
- Titanium tetrachloride ($TiCl_4$; $M_r = 189.68$; Honeywell)
- Lead acetate trihydrate ($(CH_3COO)_2Pb \times 3H_2O$; $M_r =379.33$; Reanal)
- Copper acetate monohydrate($(CH_3COO)_2Cu \times H_2O$; $M_r =199.65$; Sigma-Aldrich)
- Hydroiodic acid (HI, 57 wt %; $M_r =127.91$; VWR)
- Oxygen 99.995% (O_2; $M_r = 32.00$; Messer)

(Photo)electrochemical characterization and product quantification

- Sodium sulfate (Na_2SO_4; $M_r = 142.04$; VWR)
- Sodium sulfite (Na_2SO_3; $M_r = 126.04$; Sigma-Aldrich)
- Sodium nitrate ($NaNO_3$; $M_r = 84.99$; VWR)
- Sodium nitrate - ^{15}N labeled ($Na^{15}NO_3$, 98 atom% ^{15}N; $M_r = 85.99$; Sigma-Aldrich)
- Sodium hydroxide (NaOH; $M_r = 39.997$; VWR)

- Sodium acetate (CH_3COONa; $M_r = 82.03$; VWR)
- Nitrogen 99.995% (N_2; $M_r = 28.02$; Messer)
- Carbon dioxide 99.995% (CO_2; $M_r = 44.01$; Messer)
- Helium 99.9999% (He; $M_r = 4.00$; Messer)
- Argon 99.999% (Ar; $M_r = 39.95$; Messer)

All materials were of analytical grade and used without further purification. All solutions were prepared using ultrapure deionized water (Millipore Direct Q3-UV, 18.2 MΩ cm).

4.2 Experimental techniques

4.2.1 Preparation of nanocarbon based electrodes

Spray-coating of nanocarbons

Premium-quality GR powder (exfoliated GR platelets from Elicarb®) or MWCNTs arrays (high quality, ultra-long (1-1.5 mm) , grown chemical vapor deposition (CVD) process [145] at the Applied & Environmental Chemistry Department, University of Szeged, were dispersed in absolute ethanol by ultrasonic treatment. The formed dispersion (GR: $c = 1$ mg cm^{-3}, CNT: $c \approx 100$ μg cm^{-3}) was spray-coated on ultrasonically cleaned (5-5 min in acetone and ethanol) and preheated indium doped tin oxide-coated glass (ITO) or fluorine doped tin oxide-coated glass (FTO) electrodes, or preheated glassy carbon (GC) electrode surface (which were polished on 50 nm alumina powder prior to spray-coating) using an Alder AD320 type airbrush with a custom-made fully automated spray coater machine (**Fig. 6**) (operated with 0.5 bar compressed air). During the spray-coating process, the electrodes were masked with the used sample holder to have an exposed surface area of 1 cm^2.

To remove ethanol traces and to enhance adhesion of the GR platelets or the CNTs, the electrodes were kept in an oven (180 °C) for 30 min. GR and CNT loading was controlled with the number of spray steps (GR1-6, 30-560 μg cm^{-2}, CNT: 35-690 μg cm^{-2}, see **Table 6** in the Results section) which was quantified by quartz crystal microbalance measurements using a Stanford Research System QCM-200 type instrument. During the studies concerning TiO_2 and Fe_2O_3 photoelectrodes, the precise and fixed amount of spray-coated nanocarbons on GC and FTO was monitored by a Mettler Toledo XPE-26 type analytical microbalance.

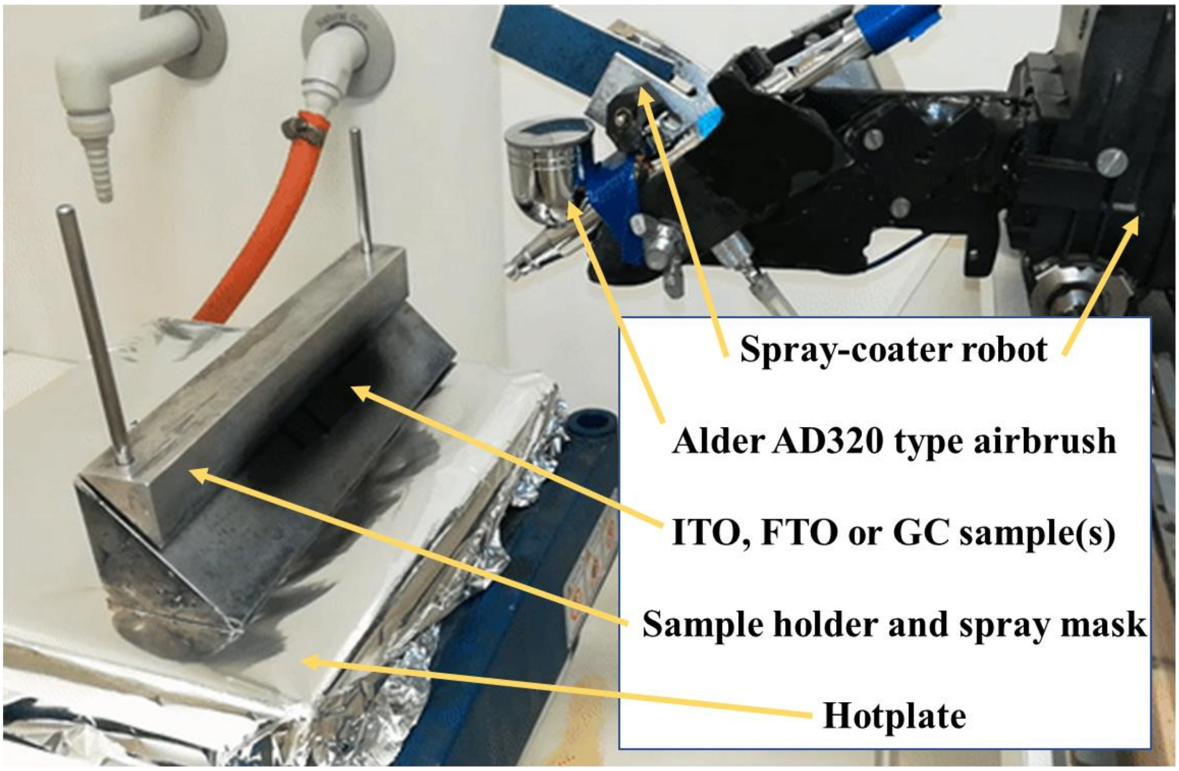

Fig. 6: Photo of the spray-coater robot, used to prepare all nanocarbon and iodide based composite electrodes.

3D graphene foam synthesis

3D graphene foam (3D-GR) was prepared at the University of Manchester via a CVD process using methane as the carbon source.[146] The 3D-GR samples were fixed on a glass sheet by a small piece of a double-sided tape and were contacted at the top by graphite adhesive to form the working electrode.

The morphology of the spray-coated CNT and GR films, together with the CVD synthesized 3D-GR are presented in **Fig. 7**.

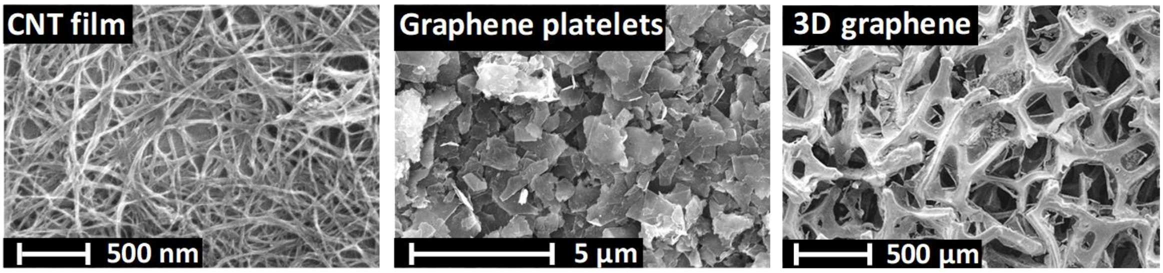

Fig. 7: SEM images of the used nanocarbon scaffolds before electrodeposition.

Electrodeposition

Electrodeposition was performed in either a cathodic (**Fig. 8a**) or anodic (**Fig. 8b**) manner, depending on the deposited material. All electrochemical syntheses were performed using an Autolab PGSTAT302 potentiostat/galvanostat. The **Fig. 9** shows the two-compartment cell (separated with a Nafion-117 membrane) with a heated jacket.

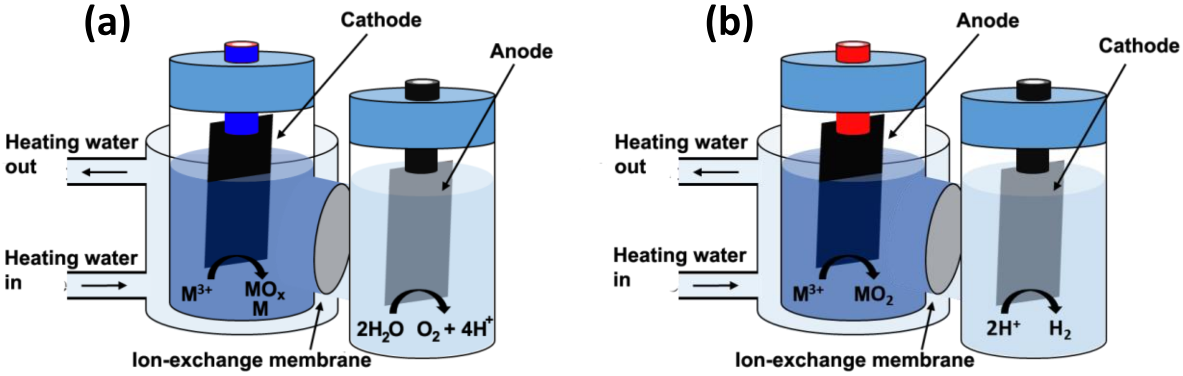

Fig. 8: Schemes of the cells employed in cathodic (a) and anodic (b) depositions.

Fig. 9: Photograph of the divided two-compartment cell with a heated jacket, applied during the electrodeposition of different oxide SCs.

Cu_2O: The nanocarbon electrodes were employed as working electrode (in the cathodic deposition arrangement), while a Pt sheet and a Ag/AgCl/3M NaCl were used as counter and reference electrodes, respectively. Cu_2O was electrodeposited from an alkaline solution of lactate-stabilized copper sulfate, containing 0.4 mol dm^{-3} cupric sulfate and 3 mol dm^{-3} lactic acid in deionized water. [147] The pH was adjusted to 9 by the addition of concentrated sodium hydroxide solution. The electrodeposition was performed in a temperature-controlled classical three electrode electrochemical cell (showed previously in **Fig. 9**). The temperature of the solution was maintained at 60 °C, and the solution was constantly stirred by a magnetic stirrer during the electrodeposition. After recording linear sweep voltammetry data, multiple step potentiostatic electrodeposition protocols were employed (see more details in the Result section).

TiO_2: Polished GC sheets and electrodes formed by the immobilization of the GR platelets were used as working electrode (in the anodic deposition arrangement). Pt sheet and Ag/AgCl/3M NaCl were used as counter and reference electrodes, respectively. TiO_2 electrodeposition was realized from a 50 mM $TiCl_3$ solution. The solution was deaerated by continuous Ar purging, and its pH was subsequently adjusted (pH = 1.5, 2, 2.5 and 3) by the dropwise addition of 0.25 M Na_2CO_3 solution. Note that the addition of strong alkaline solutions (e.g., NaOH) leads to immediate precipitate formation. To avoid hydrolysis of the precursor, the solution was kept under inert atmosphere with a continuous Ar purge above the solution during the synthesis. The two compartment cell also allowed to avoid the hydrolysis of the Ti^{3+} precursor in the close vicinity of the counter electrode, where the electrochemical H_2 evolution leads to increased pH. The deposition temperature was varied stepwise from room temperature to 80 °C (the optimal regime for producing directly crystalline material). To achieve proper wetting of the layers potentiodynamic cycling was performed on the GR electrodes in the deposition solution in a narrow potential range (E = −0.7 V - (−0.8 V)) prior to the electrodeposition. The synthesized photoelectrodes were carefully washed with deionized water and dried under air at room temperature.

Fe_2O_3: Nanostructured Ti-doped Fe_2O_3 thin films were synthesized using a cathodic electrodeposition procedure adapted from the literature.[110,148] FTO or GR-coated FTO was used as a working electrode, a Ag/AgCl/3M NaCl as a reference, and a Pt sheet as a counter electrode. The deposition electrolyte solution contained 5 mM $FeCl_3$, 5 mM NaF, 0.1 M NaCl, 0.1 M H_2O_2 and 2 at% Ti^{4+} (added from the aqueous solution of 1 M $TiCl_4$), which was gently stirred during the synthesis. To protect the spray-coated GR layer from peeling off from the FTO substrate, the concentration of H_2O_2 was reduced from 1 M to 0.1 M, compared to the originally published recipe. Potentiodynamic electrodeposition of Fe_2O_3 was carried out at 50 °C, by cycling the potential between –0.2 V and 0.4 V, using 200 mV s^{-1} sweep rate. The thickness of the deposited thin films was controlled by the passed charge during the synthesis. After electrodeposition, thin films were thoroughly washed with deionized water and dried under air at room temperature. β-FeOOH was converted to crystalline α-Fe_2O_3 by annealing at 520 °C under air (ΔT = 5 °C min^{-1}) for 30 min, which was followed by another heat treatment under Ar at 700 °C (ΔT = 5 °C min^{-1}) for 30 min.

The purpose of this second heat treatment step was to enhance crystallinity, and it was carried out under Ar to protect the underlying GR layer from oxidation.

FeNiOOH catalyst layer: To prepare FeNiOOH-decorated Fe_2O_3 and Fe_2O_3/GR electrodes, a modified version of the previously described cathodic electrodeposition procedure was employed.[124] The deposition electrolyte solution contained 5 mM $FeCl_3$, 3 mM $NiCl_2$, 5 mM NaF, 0.1 M NaCl, and 0.1 M H_2O_2, stirred gently during the synthesis. The potential was cycled between –0.49 V and +0.41 V using 200 mV s^{-1} sweep rate. Temperature of the deposition solution was kept at 50 °C. Three deposition cycles gave the highest enhancement in the PEC performance.

4.2.2 Preparation of metal-iodide based electrodes

CuI: 2.0 g of copper acetate was dissolved in 400 cm^3 ultrapure deionized water. 12-14 cm^3 of 57 wt % hydroiodic acid (HI) was diluted by 200 cm^3 deionized water. The copper acetate solution was added dropwise to the diluted (~ 3.5 wt %) HI solution slowly, under stirring. CuI formed as pale pink precipitate, which was separated by vacuum filtration and was washed with absolute ethanol until it became white (eliminating iodine contamination). This solid product was dried at 80 °C for 20 min to yield a white powder.

PbI_2: 2.0 g of lead acetate was dissolved in 380 cm^3 deionized water + 20 cm^3 absolute ethanol solution (the added ethanol reduces the solubility of the resulting PbI_2 in water). To further dilute the 3.5 wt % HI solution, this lead acetate solution was added to it using a dropping funnel, then the bright yellow PbI_2 was separated and dried, similarly to the case of Cul preparation.

Preparation of CuI-PbI_2 hybrid photoelectrodes: Different molar ratios of CuI and PbI_2 were prepared by dispersing both compounds in absolute ethanol by ultrasonic treatment. The total weight of all the composition was kept 0.4 g in 20 cm^3 absolute ethanol (in the case of 1:1 molar ratio it was 0.117 g CuI + 0.283 g PbI_2). The formed dispersion was spray-coated on cleaned (5-5 min ultrasonication in acetone and ethanol) and preheated FTO electrodes, using the previously presented spray-coater equipment (**Fig. 6**). During the spray-coating process, the electrodes were masked to have a surface area of 1×1 cm^2 (2×1.5 cm^2 for long term PEC measurements). The loading on the supporting electrodes was quantified by a Mettler Toledo XPE-26 type analytical microbalance. Pure PbI_2 and CuI films were also prepared similarly. The mixture was melted on the FTO surface at 400 °C for 5 min under argon gas (thin film melting method). Schematic representation of sample preparation is shown in **Fig. 10** and the photographs of the samples are given in **Fig. 11**.

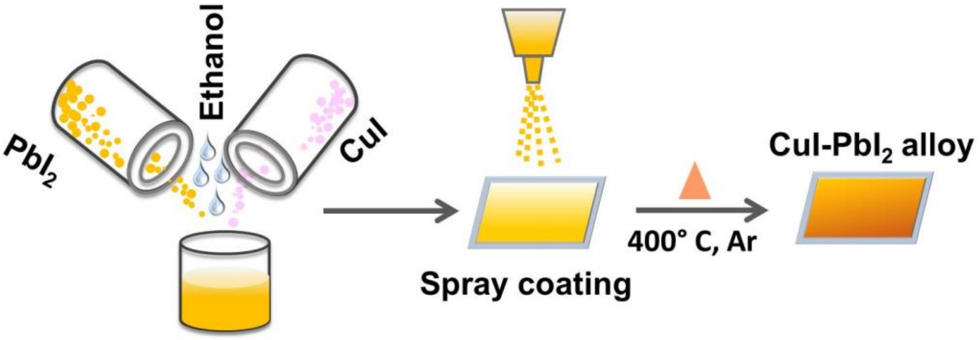

Fig. 10: Illustration of sample preparation via spray-coating. The yellow and pink colors represent PbI_2 and CuI, respectively. The film is deposited in 1x1 cm on FTO substrate (or 1.5 × 2 cm^{-2} for long term measurement).

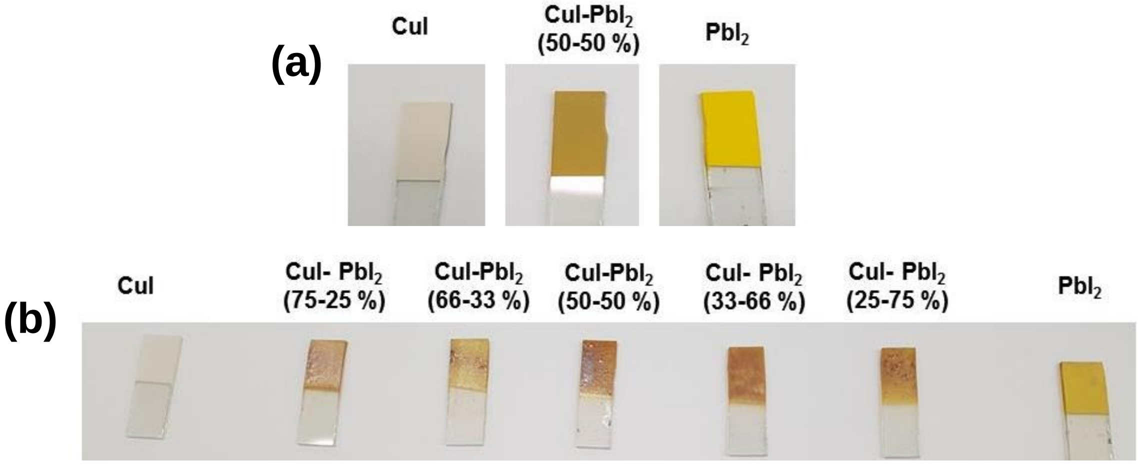

Fig. 11: Appearance of CuI, CuI-PbI_2 (50-50 %), and PbI_2 films before heat treatment. (a) Photographs of photoelectrodes after heat treatment. (b)

4.2.3 Physical characterization

Raman spectroscopy

Raman spectroscopy was employed to verify the formation of the deposited SC thin films and the SC-based nanocomposites. Furthermore, specific interactions can be suspected from any shift of the bands characteristic to the measured components. Raman spectra were recorded using a DXR Raman microscope (Thermo Scientific, Waltham, USA) using a λ = 532 nm green laser, operating at typically 5 − 10 mW laser power.

Scanning electron microscopy (SEM)

Top-down and cross-sectional scanning electron microscopic (SEM) images were captured to characterize the morphological features of both the synthesized nanohybrids, and their constituents. This technique was also used to estimate the thickness of deposited SCs in the case of different nanocomposites. A Hitachi S-4700 field emission scanning electron microscope was used for the SEM measurements coupled with a Röntec EDX detector, operating at an accelerating voltage of 10 kV.

Transmission electron microscopy (TEM)

The morphology of the samples was studied using transmission electron microscopy (TEM), FEI Tecnai G^2 20 X-Twin, operating at an acceleration voltage of 200 kV. Samples for TEM imaging were prepared by scratching the film from the ITO, FTO or GC substrate and dispersing it in ethanol. This suspension was then dropped onto copper grid for analysis. TEM lamellae of the mixed iodide samples were prepared with a Thermo Scientific Scios 2 SEM-FIB instrument. Briefly, to protect the surface a 12 x 5 μm^2 Pt pad was deposited on the surface of the sample with a 2 μm thickness. Two trenches with a depth of 7 μm were cut with ion beam on both sides of the Pt pad. The EasyLift high-precision needle was welded to this Pt pad. With an undercut a 5 μm deep slice of the sample was removed. This was transferred and attached to a half-moon TEM grid, where it was gradually thinned down and finally polished with the ion beam, to the point where it was transparent for electrons.

TEM images were used to estimate the average size of the deposited SC crystals, CNTs and GR flakes. This tool was applied also in conjunction with SEM to prove that the SC were deposited on the surface of the nanotubes or nanoflakes. Size distribution histograms were constructed from at least 300 measurement points from TEM images.

X-ray photoelectron spectroscopy

X-ray photoelectron spectroscopy (XPS) was performed to measure the surface composition and the distinct chemical states of elements on the photoelectrode surface, using a SPECS instrument equipped with a PHOIBOS 150 MCD 9 hemispherical analyzer. The analyzer was in FAT mode with 40 eV pass energy (survey scans) and 20 eV pass energy (high resolution scans). The Al K α radiation ($h\nu$ = 1486.6 eV) of a dual anode X-ray gun was used as an excitation source and was operated at 150 W power. Approximately 20-30 scans were averaged to get a single high-resolution spectrum, while one scan was recorded to get a single survey scan. For spectrum evaluation, CasaXPS commercial software package was used.

X-ray powder diffraction

X-ray diffraction (XRD) provides information about the crystal structure and phase composition of the photoelectrodes. XRD experiments were carried out on a Rigaku SmartLab diffractometer (Cu KR1 radiation λ = 1.5406 Å).

Optical absorption spectroscopy

Optical properties of the photoelectrodes were studied by optical absorption spectroscopy (UV-vis spectroscopy). Optical absorption spectra were recorded using Avantes AVASpec-2048 type instrument, equipped with an AvaSphere-30 type integrating sphere.

Photoluminescence spectroscopy

Photoluminescence (PL) spectroscopy is a form of light emission spectroscopy to determining the electronic structure and properties of materials via light emission, comes from photo-excitation. PL of the samples is measured using Jobini Yuou Fluorolog-3 spectrometer.

Kelvin probe microscopy-coupled ambient UV photoelectron spectroscopy

Kelvin probe microscopy (KP Technology APS04 instrument) was used to measure the Fermi level position [149] while ambient pressure photoemission spectroscopy was employed to detect photoelectrons emitted from VB, and thus determining VB positions. [150].

4.2.4 (Photo)electrochemical measurements

Linear sweep photovoltammetry

During linear sweep photovoltammetry measurements, the potential of the working electrode is scanned with a constant speed to one direction in a potential window, while the surface of the working electrode is irradiated periodically (examples are shown in **Fig. 12**). The most important advantages and parameters which can be obtain from this type of measurements:

- The value of the dark-, and photocurrent can be measured and visualized on one plot (**Fig. 12**).
- The type of SC can be immediately judged from the sign of the photocurrent; cathodic photocurrents – p-type SC, anodic photocurrents – n-type SC (**Fig. 12a** and **b**).
- The flatband potential can be obtained from the onset of the photovoltammogram, which can be correlated to E_{VB} in the case of a p-type SC and to E_{CB} in the case of an n-type SC [151].
- The shape of the transients during illumination period can imply if significant recombination occurs on the SC/electrolyte interface (spikes).

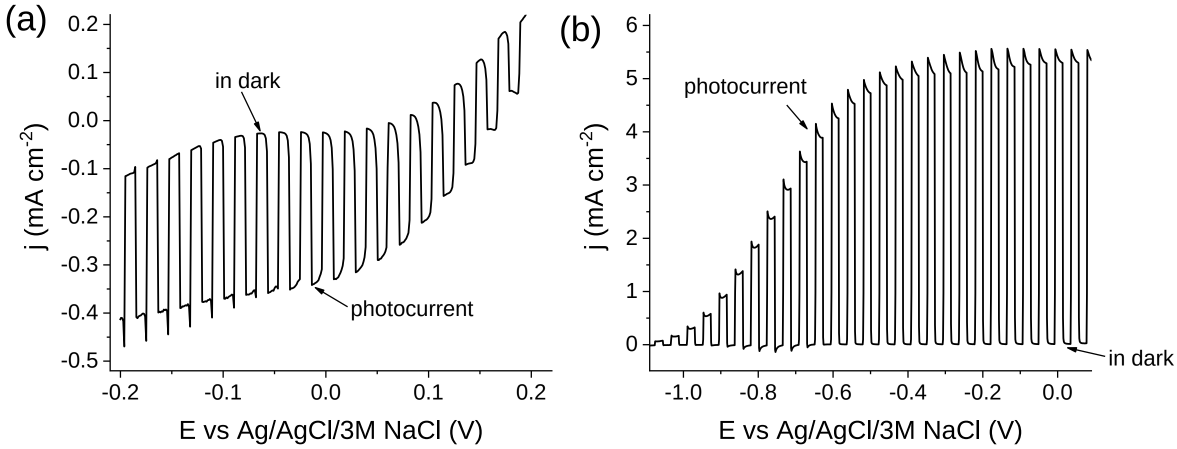

Fig. 12: Examples to a linear sweep photovoltammogram, recorded for a p-type SC (a) and n-type SC (b).

All PEC measurements were performed using a Metrohm Autolab PGSTAT302 type potentiostat/galvanostat. Linear sweep photovoltammograms were recorded in a sealed, custom-designed one-compartment, three-electrode quartz cell. The working electrode was always covered with the SC or nanocomposite to be examined, while a Pt sheet and Ag/AgCl/3M NaCl were employed as the counter-, and reference electrode respectively.

Two light sources were applied during these measurements:

- A Newport LCS-100 type *solar simulator* operated at full output. The solar simulator source was placed 5 cm and 18 cm away from the illuminated working electrode surface (5 suns, 500 mW cm^{-2} flux for CuI-PbI$_2$ nanocomposite system and 1 sun 100 mW cm^{-2} flux for Cu$_2$O/nanocarbon and Fe$_2$O$_3$/GR composite systems), which was irradiated through a quartz window.
- A Hamamatsu L8251 300 W *Hg-Xe arc lamp*, operated at full output. The lamp was placed 5 cm away from the illuminated working electrode surface (180 mW cm^{-2} flux), which was irradiated through a quartz window. The irradiation spectra of both lamps are presented in **Fig. 13**.

The sealed cell was saturated with Ar, N$_2$ or CO$_2$ as needed, by 20 minutes of continuous bubbling prior to each measurement. Linear sweep photovoltammograms were recorded using a slow potential sweep (2 mV s^{-1}) in conjunction with periodically interrupted irradiation (0.1 Hz).

The potential values were converted to the reversible hydrogen electrode (RHE) scale in some cases, using the following equation:

$$E(RHE) = E\ (\mathrm{Ag/AgCl/3M\ NaCl})\ + 0.059 \cdot pH\ \ + E^0\ (\mathrm{Ag/AgCl/3M\ NaCl}) \qquad (1)$$

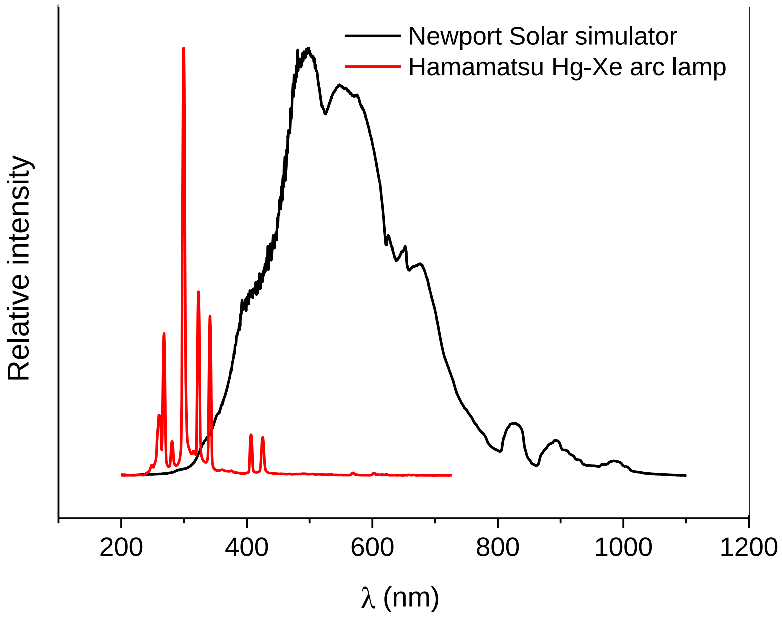

Fig. 13: Irradiance spectra of the lamps employed in all PEC experiments.

Photoaction spectra, incident photon-to-current efficiency

Incident photon-to-current-conversion efficiency (IPCE) or external quantum efficiency (EQE) is one of the most important diagnostic figures of merit for PEC systems. It describes the photoelectrons collected per the incident photon flux as a function of the illumination wavelength (Eq. 2). IPCE combines the efficiencies of three fundamental processes, involved in photoelectrochemistry [152]:

- photon absorptance – the fraction of the electron-hole pairs generated per incident photon flux,
- transport of the photogenerated charge carriers toward the electrode/electrolyte interface and finally,
- efficiency of the interfacial charge transfer.

$$IPCE = EQE = \eta_{e^-/h^+}\eta_{transport}\eta_{interface} = \frac{Number\ of\ photo\ e^-/t}{Incident\ photon\ flux} \times 100\% \qquad (2)$$

In a PEC system, IPCE data are usually derived from chronoamperometric measurements. A constant bias potential is applied to the working electrode (typically at which the photocurrent is high enough, but the investigated system is still stable) followed by the periodic illumination of its surface with a monochromatic light at various wavelengths. When Eq. 2 used in experiments, IPCE corresponds to the photocurrents, derived from the chronoamperometric curve (converted to an electron rate) versus the rate of incident photons, converted from the calibrated power of the employed light source.

Several useful parameters can be obtained from IPCE measurements:

- The wavelength-range, where the studied sample is photoactive – ideal if this window and the maximum of the curve overlaps with the absorption spectrum of the material,
- device efficiency in terms of "electrons out per photons in", also considering the spectral variation of incident photons at each energy,
- the bandgap of the investigated SC by fitting a linear to the cutoff-region of the IPCE curve and
- the total solar-to-electron-conversion efficiency by integrating the IPCE data over the solar spectrum.

IPCE measurements were performed on a Newport Quantum Efficiency Measurement System (QEPVSI-B) in a single compartment, three-electrode quartz electrochemical cell. The resolution was kept at $\Delta\lambda$ = 10 nm.

Electrochemical impedance spectroscopy

The electric properties of the nanocomposites were studied by electrochemical impedance spectroscopy (EIS). EIS data were recorded in the 10 Hz to 100 kHz frequency range, using a sinusoidal excitation signal (10 mV RMS amplitude). Modulus weighted fitting was performed using the Nova Software of the Autolab Instrument.

EIS data were quantified by fitting an equivalent circuit to the experimental data (**Fig. 14**). The circuit consists the following elements: an equivalent solution resistance (R_s), a charge transfer resistance (R_{ct}), double layer capacitance related to the high surface area of the porous electrode (C_1), a diffusion related Warburg element (W) and another capacitance (C_2) completed the modified RRC-circle. (C_2) [153].

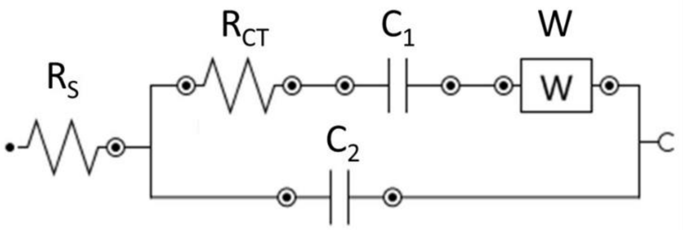

Fig. 14: Equivalent circuit fitted to the measured EIS data.

Fast photocurrent transient measurements

To study the charge carrier recombination process occurring at the SC/electrolyte interface, transient PEC measurements were also performed [154,155]. During these measurements, the photocurrent was traced after the illumination was turned on. To fit the most precise model to the experimental data the resolution of the detection must be as high as possible. In our current instrumental setup, the highest possible resolution was around 50 μs (100,000 point in a 5 second measurement). Two examples to a transient photoresponse are presented in **Fig. 15**. A transient photoresponse can be divided in two parts: 1) a fast increase, where the maximum photocurrent evolves, and 2) a slower decaying section, where the photocurrent decreases up to point where it reaches its steady-state value. The first part is related to the hole-transport through the electrode assembly, while the second one can be correlated to the surface recombination process [156].

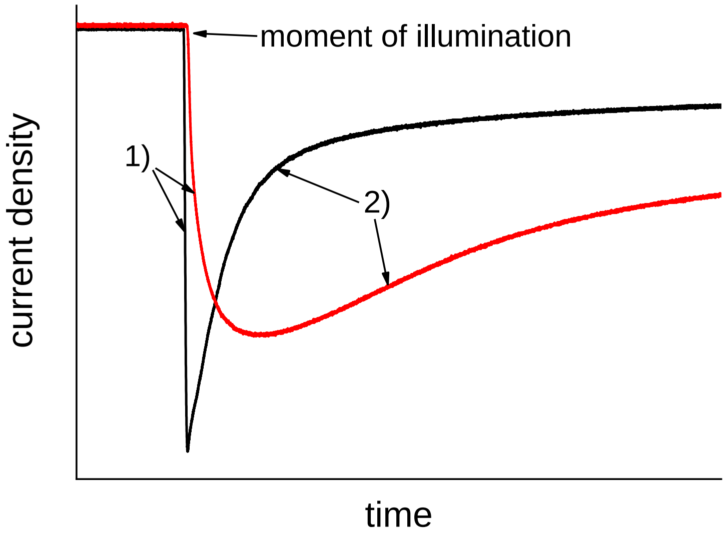

Fig. 15: A typical transient photoresponse. 1) and 2) shows the two parts where the photoresponse can be divided.

To quantify the above two processes observations, the experimental data was fitted, and time constants were determined. The transient photoresponse curves can be modeled by a simple binomial exponential function [157]:

$$j = A_1 \cdot \left(\exp\left(-t/\tau_1\right) - 1\right) + A_2 \cdot \left(\exp\left(-t/\tau_2\right) - 1\right) \qquad (3)$$

The first exponential is related to the transport of the majority carriers (in the case of p-type semiconductors, these are holes) through the electrode assembly, which is characterized by a time-constant called τ_1. The second exponential is corresponded to the surface recombination process, which is characterized by another time-constant, τ_2. The two pre-exponential factors provide numerical information about two extreme situations. A_1 gives the value of the maximum harvestable photocurrent, when no recombination occurs, and A_2 gives the harvestable photocurrent, when maximal recombination occurs.

Fast transient measurements were performed in the same, custom-designed, sealed three-electrode quartz cell as the one which was used during the linear sweep photovoltammetry experiments. Measurements were carried out in 0.1 M Na_2SO_4 saturated with Ar or N_2 and CO_2 in the case of Cu_2O/nanocarbon photoelectrodes. The duration of illumination was three seconds, while the current was traced for four seconds.

4.2.5 Product detection and quantification

Long-term PEC measurements were carried out in a sealed two-compartment cell ($V_{solution}$ = 35 cm^3) where the compartments were separated by a Nafion117® membrane. The working electrode was the prepared and investigated photoelectrode (A = 1 cm^2 or 3 cm^2). A Pt sheet was applied as a counter, and a Ag/AgCl/3 M NaCl as a reference electrode. Measurements were carried out in 0.1 M Na_2SO_4 (saturated with CO_2) and in 0.1 M $NaNO_3$, (saturated with Ar). During the reactions, gas samples were taken at every hour via an on-line detection system, which was coupled to the cathode compartment of the cell (see later). Liquid phase aliquots were taken from the cathode compartment of the cell at the same time as gas phase samples with a Hamilton-syringe, via a septum-sealed hole on the top of the cell.

Gas chromatography equipped with a dielectric barrier discharge ionization detector

Gas phase samples were analyzed via an on-line detection system, using a gas chromatograph, equipped with a dielectric barrier discharge ionization detector (BID). The use of an on-line system is essential to obtain accurate quantities and Faradaic efficiencies, especially if H_2 is among the formed products. Schematic illustration of the whole on-line setup is presented in **Fig. 16**.

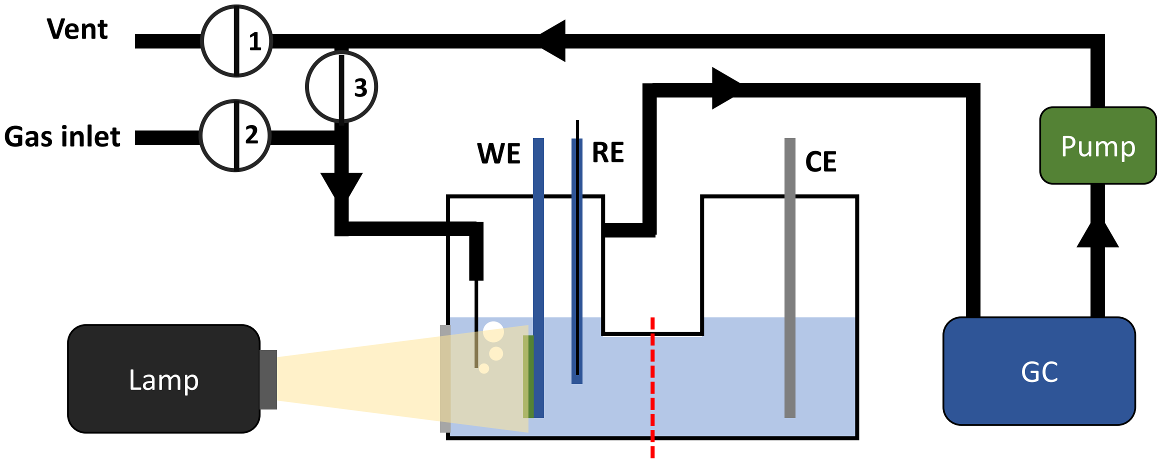

Fig. 16: Schematic illustration of the GC-BID on-line setup used during the long-term photoelectrolysis experiments. (Own illustration)

As a first step, the PEC cell was saturated with either Ar or CO_2 as needed. To achieve this, valve 1 and 2 are in an open position and the valve 3 is closed (**Fig. 16**). In this way, the electrolyte and the gas chamber above the solution can be saturated. After purging the solution for at least 20 mins, valve 1 and 2 are closed, and the valve 3 is opened (this results the closed loop status). As a next step, the measurement can be started and before the sampling, the gas in the closed loop has to be circulated by a peristaltic pump in few minutes (mixing the gas space). To inject the sample, the 6-port external volume sample injector automatically turns, and the sample is automatically injected to the column.

Products in the gas phase were separated with a ShinCarbon ST column and analyzed with a Shimadzu GC-2010 Plus gas chromatograph equipped with a BID detector. The optimized sampling parameters were the following: carrier gas: helium; oven program: T_{start} = 35°C (2.5 min), ΔT_{ramp} = 20 °C min^{-1}, T_{end} = 270 °C (3 min); injection temperature: T = 150 °C; linear velocity was controlled by the pressure p_{start} = 250 kPa (2.5 min) Δp_{ramp} = 15 kPa min^{-1} p_{end} = 400 kPa (7.5 min); and split ratio: 10. Prior to evaluate the amount of the formed product, calibration measurements were performed, using a gas mixture containing H_2, CO, CH_4 and C_2H_4, in concentrations, ranging from 0.1 V/V% up to 10 V/V%.

After measuring and calculating the amount of the products in the gas phase, Faradaic efficiencies (FE) can be obtained using Eq. 4 [11]:

$$FE\% = \frac{Q_{product}}{\Sigma Q} \times 100\% = \frac{n_{product} \times F \times z}{\Sigma Q} \times 100\% \qquad (4)$$

where n_{product} is the moles of product evolved, F is the Faraday-constant and z is the number of electrons needed for the formation of the given product. ΣQ can be derived by integrating the chronoamperometric curve, recorded during the long-term photoelectrolysis experiment. FE is one of the most important figures of merit for a PEC system as it describes the selectivity. In an ideal system, ΣFE% is close to 100%, however, values below 100% can be measured if i) not a well-sealed system is used for product detection or if ii) the amount of the formed products lower than the detection limit of the given analytical technique and finally, if iii) any side-reaction occurs during the long-term PEC measurement (photocorrosion, unexpected by-product, etc.).

Gas chromatography equipped with a mass spectrometer detector

The liquid or gas aliquots were injected into a Shimadzu GC-MS 2010SE chromatograph coupled with a MS QP2010 detector. The chromatographic column was Stabilwax-DA (30 m length and 0.32 mm inner diameter) set at 40 °C, the gradually reached injection temperature was 220 °C. The MS detector was set at 200 °C, and helium was used as the carrier gas. Qualitative detection was afforded by selective ion monitoring (SIM)-MS, while the total ion chromatogram was used for the quantification of methanol and ethanol.

For the qualitative detection of nitrogen gas formation from NO_3^- ion reduction, Ar-saturated 0.1 M ^{15}N labeled (98%) $Na^{15}NO_3$ solution was used. During the photoelectrolysis, samples were taken from the gas space (with a Hamilton needle through a septum built into the cell) and were analyzed by GC-MS. Because the natural occurrence of $^{15}N_2$ gas is low (0.0016%), contamination from the air does not interfere with detecting $^{15}N_2$ produced through the reduction of nitrate ions (see more details later in **Fig. 82**)

Ion chromatography

The most likely products of NO_3^- ion reduction are NO_2^-, N_2 and NH_3. The amount of nitrite formed via nitrate reduction was quantified using ion chromatography (IC). All IC measurements were performed with a Dionex DX300 gradient chromatographic system (Dionex, Sunnyvale, CA, USA) that consisted of a CHA-6 high pressure chromatographic module, Dionex EDM eluent degas module and an Advanced Gradient Pump module. Suppressed conductivity detection was used during chromatographic runs. The injection unit (Model 9125, Rheodyne, Rohnert Park, CA, USA) contained 50 µl injection loop. Separations of cations were carried out by a Dionex IonPac CS16 columns (3×250 mm). 12.5 mM methanesulfonic acid was used as eluent at 0.5 cm^3/min flow rate. Anions were separated by a Dionex IonPac AS15 column (2×250 mm) using 35 mM KOH eluent at 0.3 cm^3/min flow rate.

Colorimetric analysis

Presence of ammonia in the product was tested by modified Berthelot test (Indophenol method). [158] Liquid aliquots for the test were taken regularly during photoelectrolysis and the aliquots were tested using colorimetric method.

Proton nuclear magnetic resonance (^{1}H-NMR)

To prove that the measured ammonia in Indophenol method was indeed derived from the reduction of the nitrate ion, an Ar-saturated 0.1 M ^{15}N labeled (98%) $Na^{15}NO_3$ solution was used during the photoelectrolysis, where the extent of possible $^{15}NH_3$ formation in the taken aliquots was monitored by ^{1}H-NMR.

5. RESULTS AND DISCUSSION

5.1 Photoelectrochemical properties of p-type Cu_2O/nanocarbon composite photoelectrodes

Before the electrochemical synthesis of the Cu_2O/nanocarbon composites, consecutive potentiodynamic cycling was performed until stable capacitive electrochemical behavior was reached; this ensured proper wetting of the CNT and porous GR structures. The potential window for this pre-conditioning step was chosen so that no Faradaic process occurred in this regime (neither with the electrolyte, nor with the electrode itself, see **Fig. 17a**).

Similar measurements were performed on a carefully polished, flat GC electrode, which had the same electroactive and geometrical surface area (i.e., its surface roughness is 1), and thus served as the basis of normalization. The ratio of the charge capacitance (or the charging currents, recorded at E = +0.2 V vs Ag/AgCl/3M NaCl in our case) values directly yielded the ratio of the electroactive surface areas. The used GR platelets had about six-times higher *specific* surface area than the CNT films (in line with typical surface area data for such materials, **Table 6**); therefore smaller loadings were enough from the GR platelets to have the same actual electrode surface area. Interestingly, the electroactive surface area of the 3D-GR electrode was considerably smaller than that of the spray coated samples, which will be considered in what follows. These measurements were performed for each nanocarbon substrate individually and the measured current values were normalized with respect to the derived surface area where normalized data are presented.

The automated spray-coating resulted in scalable immobilization of the GR flakes on the ITO surface (**Fig. 17b**). Both the mass and the charge capacitance scaled linearly with the number of spray-coating cycles (**Table 6**).

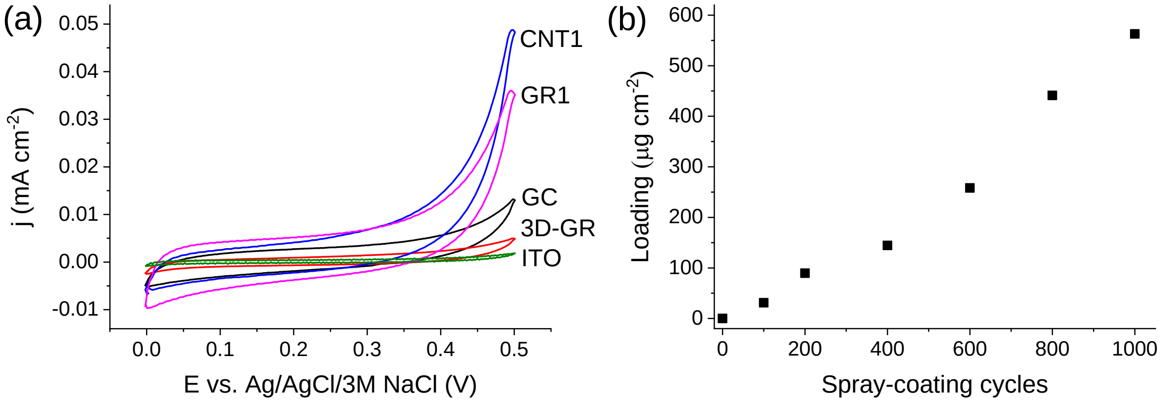

Fig. 17: (a) Cyclic voltammograms of the nanocarbon electrodes in 0.1 mol dm^{-3} Na_2SO_4 solution (scan rate: 50 mV s^{-1}). (b) Surface coverage of the GR coated electrodes as a function of the spray-coating cycles.

Table 6: Annotation and properties of the studied nanocarbon substrates.

Designation	Spray-coating cycles	Mass (μg cm^{-2})	Electrode charge capacitance (mC cm^{-2})
GR1	100	30	0.078
GR2	200	90	0.238
GR3	600	250	0.661
GR4	1000	560	1.44
CNT1	200	170	0.063
CNT2	800	690	0.257
3D-GR	-	-	0.014

5.1.1 Electrodeposition Cu_2O on spray-coated carbon-nanotube film

Prior to electrodeposition of the Cu_2O crystals, an electrochemical conditioning step was carried out in the Cu-lactate solution, to remove any entrapped gas and to ensure proper wetting of the CNT film. This step consisted of multiple cyclic voltammetry scans in a potential window (between E = 0.0 V and +0.5 V), where the lower vertex potential was more positive than the potential required for the reduction of Cu^{2+}. During these cycles we also observed the evolution of the capacitance dominated electrochemical behavior of the CNTs (as we showed in the previous chapter), with parallel desorption of the entrapped gases (N_2 and O_2).

Based on earlier literature studies, [30,36,147] we aimed to employ slow potentiostatic deposition, to minimize the metallic Cu content of the deposited oxide phase. To determine the deposition potential, linear sweep voltammetry curves were recorded. As seen in **Fig. 18a**, the two curves have a very similar pattern, but the cathodic currents start to develop at markedly less negative potential values ($E \approx -0.2V$) on the CNTs than at the bare ITO coated glass electrode. This shift indicates that oxide formation is favored on the CNTs, and by appropriately selecting the potential value, Cu_2O crystals could be exclusively deposited on the CNTs (this was also confirmed by the SEM images, **Fig. 19**).

It was found that simple potentiostatic growth results in homogeneous films on a microscopic level without, or even with very small amounts of CNTs (less then 50 μg cm^{-2}). In the case of thicker CNT films, similar homogeneity was no longer present, so more sophisticated deposition methods were required. Therefore, we developed an approach consisting of multiple potentiostatic deposition steps, as well as rest periods interspersed among them, to allow for continuous supply of the copper ions from the bulk solution (**Fig. 18b**). An initial nucleation step at a more negative potential (–0.35 V) was also found to be beneficial for achieving homogeneous coating on the CNT/ITO electrode. The length of this nucleation step, however, cannot be too long, because formation of metallic copper also could occur at this potential. Accordingly, the subsequent Cu_2O growth was performed at less negative potential (–0.25 V). This protocol is summarized in **Fig. 18b**, whereas the observed response is shown in **Fig. 18c**. where can be observed the rapid nucleation step during in the first several second (as deduced from the high currents), while a steady growth is indicated during the subsequent phase.

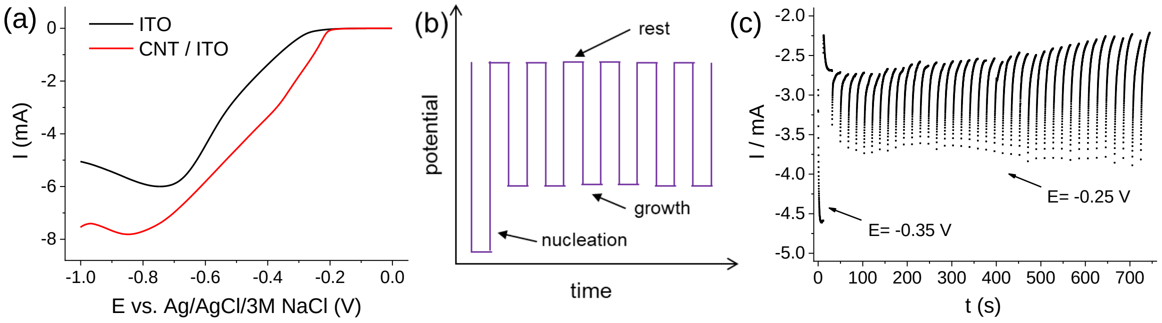

Fig. 18: (a) Linear sweep voltammograms recorded in 0.4 M Cu-lactate solution (pH = 9), at a sweep rate of 25 mV s^{-1}, on both ITO and CNT/ITO electrodes. (b) schematic illustration of the multiple potential-step protocol, employed for the electrodeposition. (c) current response of a CNT/ITO electrode (170 µg cm^{-2}) while applying the potential waveform shown in (b).

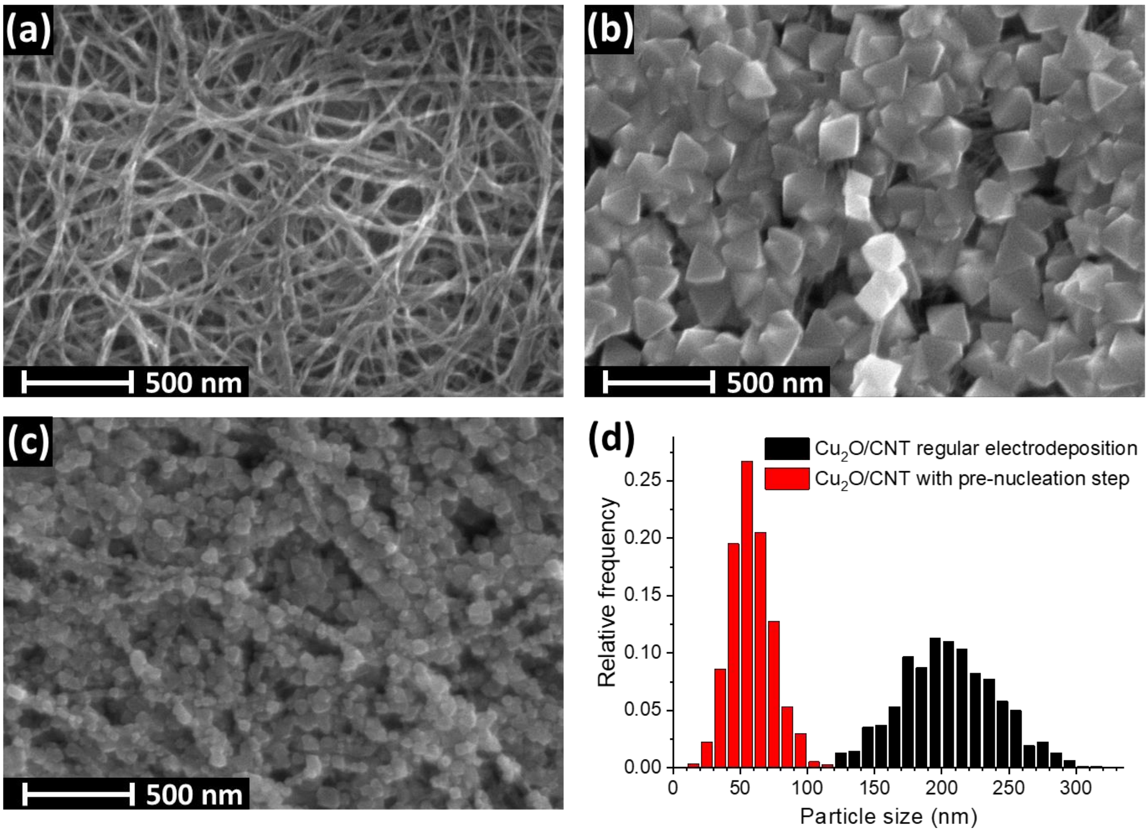

Fig. 19: SEM images of the bare CNT film (a), a Cu_2O/CNT composite obtained at constant E = –0.25 V potential, Q = 200 mC cm^{-2} (b), and with a short pre-deposition step at E = –0.35 V potential Q = 200 mC cm^{-2} (c). Particle size distribution (d) based on the samples of (b) and (c) with the deposited the same amount of Cu_2O on the CNT film.

The above observations were also confirmed at the sub-microscopic level. SEM studies visualized the bare spray-coated CNT film on ITO (**Fig. 19a**) and the formation of typical octahedral Cu_2O crystals on the CNT surface (**Fig. 19b** and **c**). Importantly, while some bare CNTs can be spotted on the sample synthesized without the pre-nucleation step (**Fig. 19b**), perfect coverage is seen when the optimized protocol (with the pre nucleation step and the rest times) was employed (**Fig. 19c**). This better homogeneity was a general trend, observed in all the cases when the pre-nucleation step was applied. In addition, a striking difference can be seen in the size of the Cu_2O particles deposited, namely they are much smaller in the latter case. This is not a surprise considering equal amount of deposition charge (200 mC cm^{-2}), and the larger number of nuclei formed during the nucleation step at a more negative potential. This difference was also quantified by obtaining the particle size distributions. As the histograms in **Fig. 19d** show, the particles are massively larger in the first case (d_{av} = 200 nm vs. 60 nm). We note here that these particle sizes serve only for comparative purposes, since they can be widely tuned by the deposition charge. TEM images (**Fig. 20a** and **b**) also confirmed the above conclusions, and very similar particle sizes were obtained.

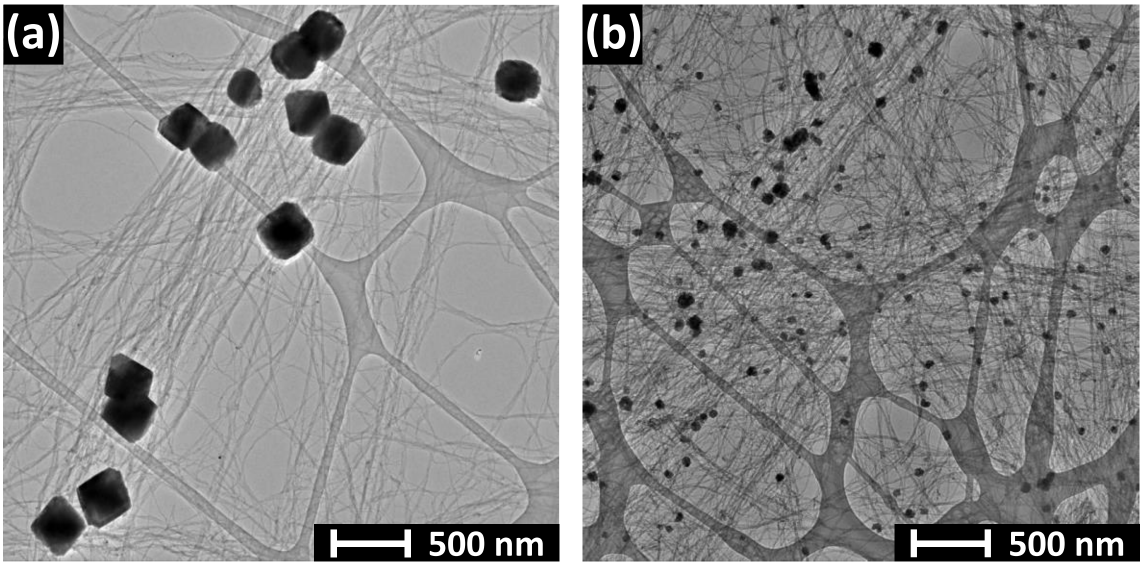

Fig. 20: TEM images of the electrodeposited Cu_2O on CNT sample obtained at constant E = –0.25 V potential, Q = 200 mC cm^{-2} (a), and with a short pre-deposition step at E = –0.35 V potential Q = 200 mC cm^{-2} (b).

Structural properties of the Cu_2O/CNT composite were investigated using Raman spectroscopy and XRD, and both techniques confirmed the formation of Cu_2O nanocrystals on the CNTs (**Fig. 21a** and **b**, respectively). The Raman spectrum of the CNT film shows the typical D and G-bands at 1346 and 1588 cm^{-1} respectively. The bands at 150, 212, and 630 cm^{-1} all confirm the formation of cuprite (Cu_2O) crystals. [159] Importantly, the absence of the phonon peak around 300 cm^{-1} proves the absence of CuO in the film. On the spectrum of the hybrid sample, beyond the obvious appearance of the bands of its constituents, an interesting phenomenon can be spotted. The decrease in the D/G band ratio after the cathodic synthesis indicates an improved quality (most likely because of the electrochemical reduction of certain oxygen-functional groups). XRD data furnished further evidence for the formation of Cu_2O. Comparison of the XRD patterns for two Cu_2O/CNT samples (with and without a nucleation step) is provided in **Fig. 21b**. Both patterns are consistent with the presence of a Cu_2O phase [160], except two minor diffractions (marked with asterisks) which originate from the presence of metallic copper traces. The Scherrer equation was employed to estimate the size of the crystalline domains using the most intensive reflection (111). As seen in **Fig. 21b**, in line with the electron microscopic observations (see above), a markedly smaller value was obtained for the sample obtained with a pre-nucleation step (21 nm vs. 30 nm).

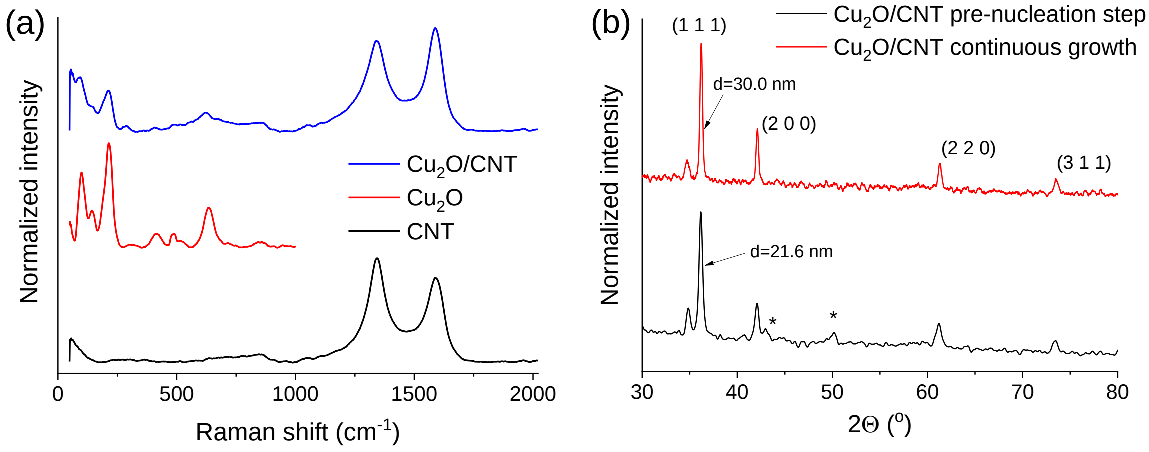

Fig. 21: (a) Raman spectra of a CNT film, an electrodeposited Cu_2O film, and a hybrid CNT/Cu_2O sample. (b) XRD patterns of two different Cu_2O/CNT samples synthesized with and without a pre-nucleation step respectively. *indicates the reflection from metallic Cu phase.

5.1.2 Electrodeposition of Cu_2O/ graphene composites

Electrodeposition of the Cu_2O nanoparticles on the different GR substrates was realized using a multiple-step potentiostatic method (**Fig. 23**), similar to what we used in the case of CNT scaffold. Based on linear sweep voltammetric data (**Fig. 22**), a first nucleation step was also conducted at E = –0.35 V to initialize the formation of small seed particles, followed by one or more slow crystal growth steps at a less negative potential (E = –0.25 V). For the spray-coated GR samples, multiple growth steps were applied to introduce rest periods allowing for continuous supply of copper ions from the bulk solution, but it was not applied in the case of 3D-GR. We emphasize that although the pre-nucleation step leads to some copper traces in the formed Cu_2O, it was found to be essential to reach homogenous coverage of the nanocarbon supports.

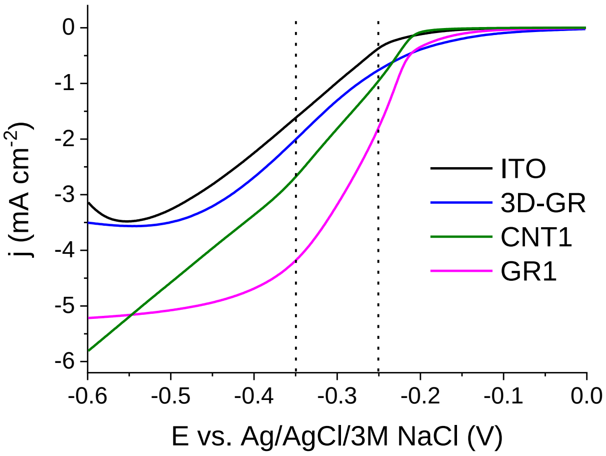

Fig. 22: Linear sweep voltammetry curves, recorded in a basic solution of lactate-stabilized copper sulfate, containing 0.4 mol dm^{-3} cupric sulfate and 3 mol dm^{-3} lactic acid in deionized water at pH = 9. The temperature was kept at T = 60 °C, and the solution was vigorously stirred during the synthesis. The sweep rate was 25 mV s^{-1}. The vertical dashed lines indicate the used deposition potentials.

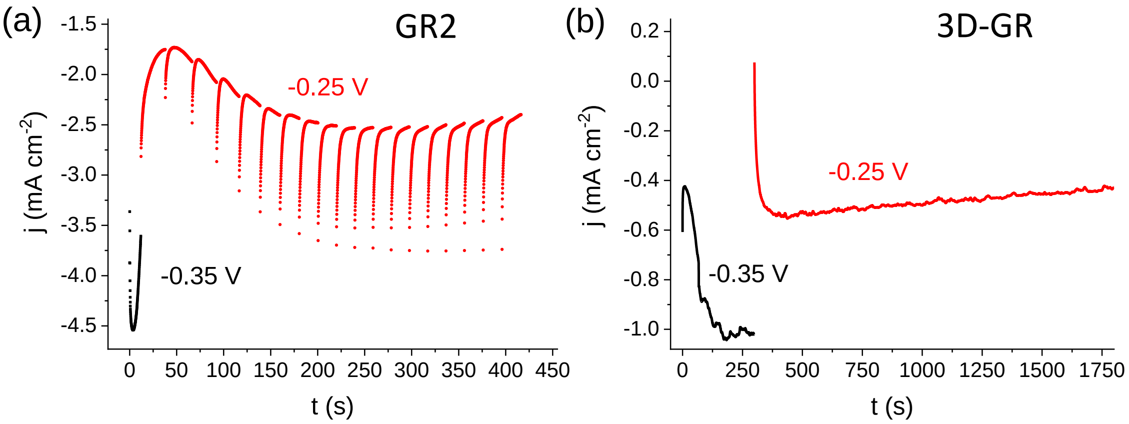

Fig. 23: (a) Current response of a GR2/ITO electrode, while applying the multiple-potential step protocol. (b) Current-time curves, registered during the two-step potentiostatic electrodeposition of Cu_2O on a 3D-GR electrode. Both syntheses were performed in 0.4 mol dm^{-3} cupric sulfate and 3 mol dm^{-3} lactate solution, at pH = 9 and T = 60 °C.

When the pre-nucleation step was omitted, crystal formation occurred *exclusively* on the edges of GR sheets (see the inset in **Fig. 28d later**). In agreement with our earlier results on Cu_2O decorated CNTs, we can conclude that homogenous coverage of carbon nanostructures necessitates the application of a larger driving force (i.e., deposition potential), otherwise only the energetically preferred defect places (e.g., edges, amorphous carbon traces, and grain boundaries) are covered by the electrodeposited Cu_2O.

Electron microscopy images were taken for the hybrid Cu_2O/GR samples with various compositions to probe their morphological attributes. TEM images confirmed that the Cu_2O

nanocrystallites are evenly dispersed on the GR flakes (**Fig. 24** and **Fig. 26** for more images at both lower and higher magnifications). Additionally, it was also demonstrated that both the size and density of the nanoparticles can be effectively controlled by tuning the deposition protocol (i.e., the transferred charge). As seen in **Fig. 24** (from left to right), the growing deposition charge (from 200 mC cm^{-2} to 1 C cm^{-2}) resulted in a gradual increase in both the surface coverage and the particle size. Specifically, the mean particle diameter shifted from 50 to 110 nm as deduced from the histograms in **Fig. 25**.

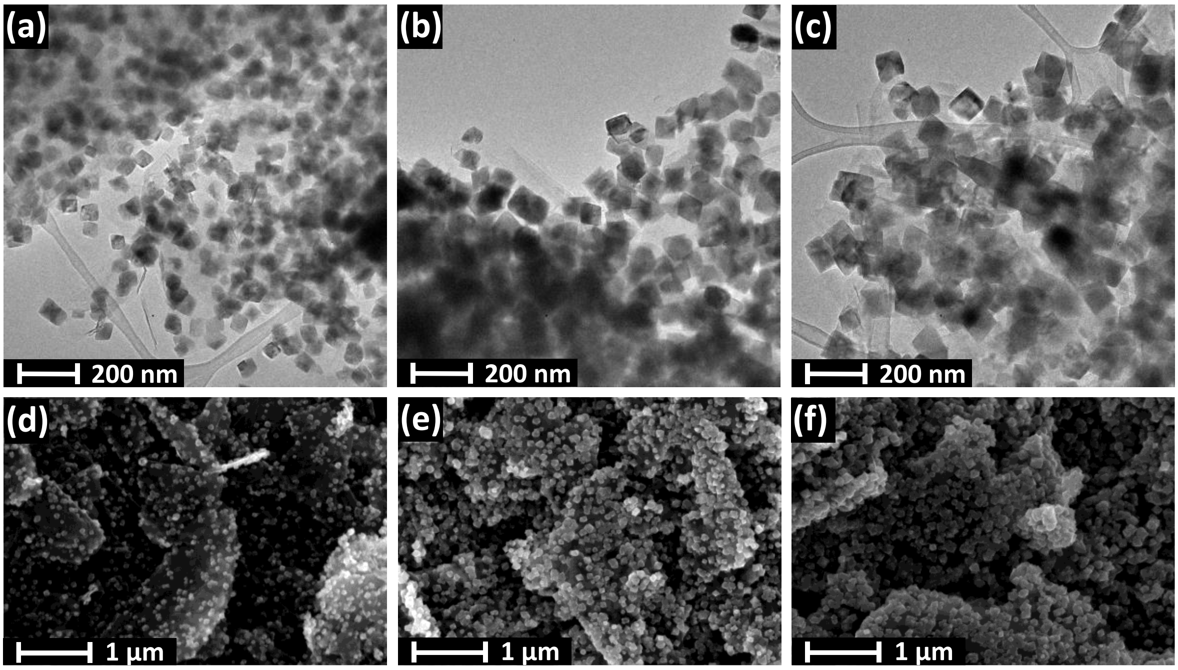

Fig. 24: TEM images of Cu_2O/GR3 hybrids obtained with the deposition protocol shown in the **Fig. 23a**. The deposition charges were (a) 200 mC cm^{-2}, (b) 600 mC cm^{-2}, and (c) 1000 mC cm^{-2}. SEM images are also shown for the same samples (d-f).

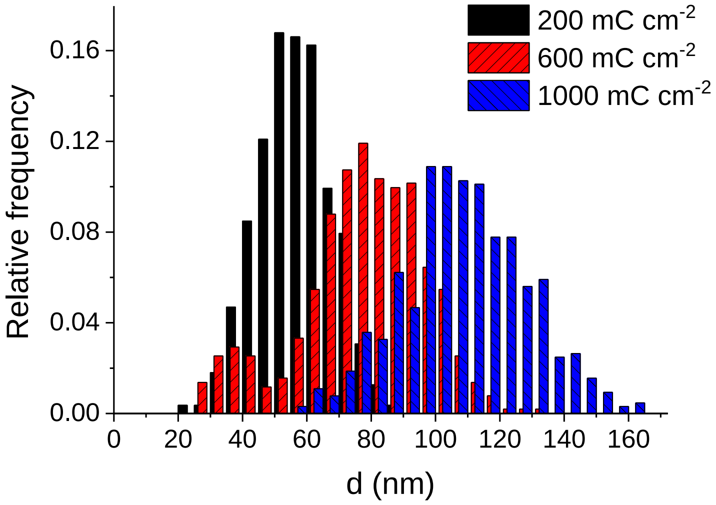

Fig. 25: Particle size distribution for the same samples presented in **Fig. 24**. The data were gathered from the TEM images, by measuring the size of 300 particles in each case.

SEM images further confirmed the even dispersion of Cu_2O nanoparticles on the GR platelets (**Fig. 24d-e).** SEM images were taken for the bare Cu_2O film on an ITO electrode (**Fig. 27**) for comparison with Cu_2O/GR3 on **Fig. 24d-e** (same deposited charge steps were apply). Most importantly, the crystallite sizes were much larger in this case, due to the smaller electrode surface area (note that the amount of the deposited Cu_2O was identical).

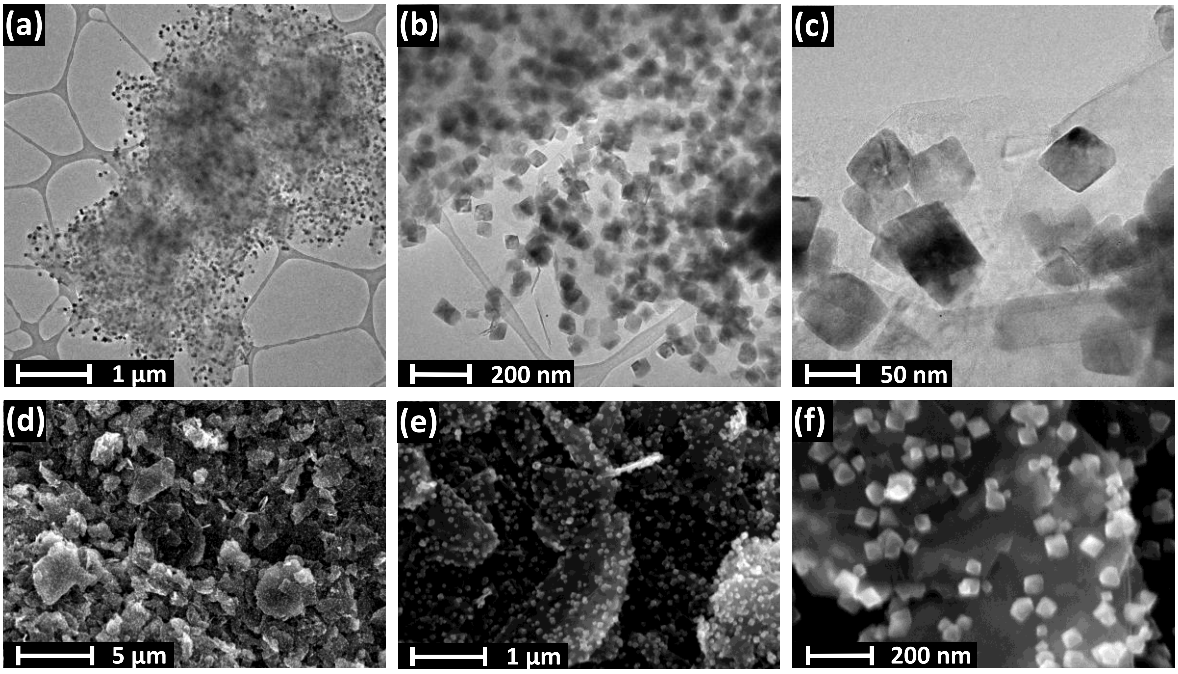

Fig. 26: TEM (a-c) and SEM (d-f) images of a Cu_2O/GR hybrid (200 mC cm^{-2}, GR3) captured at various magnifications.

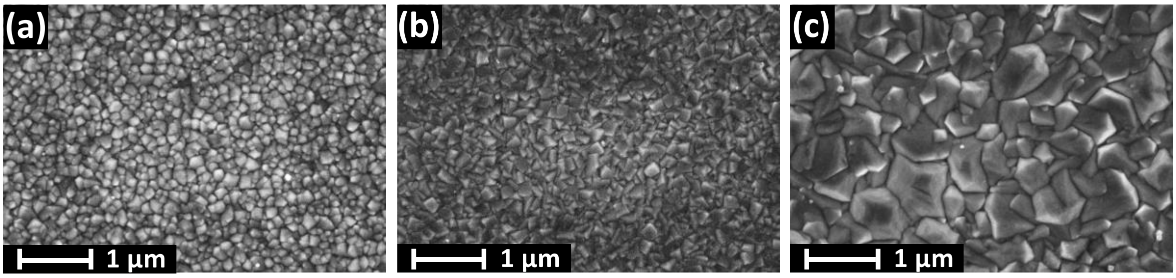

Fig. 27: SEM images of Cu_2O films on ITO, deposited with 200 mC cm^{-2} (a), 600 mC cm^{-2} (b), and 1000 mC cm^{-2} (c), for comparison with Cu_2O/GR3 samples on **Fig. 24d-e**.

For the 3D-GR based hybrids, the GR platelets were homogenously and almost completely covered with octahedral Cu_2O nanoparticles (see also **Fig. 29** for elemental mapping by EDX), having a size in the range of 100-150 nm (**Fig. 28c**). For this system, the initial nucleation step was indeed required to avoid specific deposition at the edge of the GR platelets (compare with the inset in **Fig. 28d**). Finally, we note that the original structure of the 3D-GR support was preserved in the nanocomposite; it did not suffer any major damage during the electrochemical deposition.

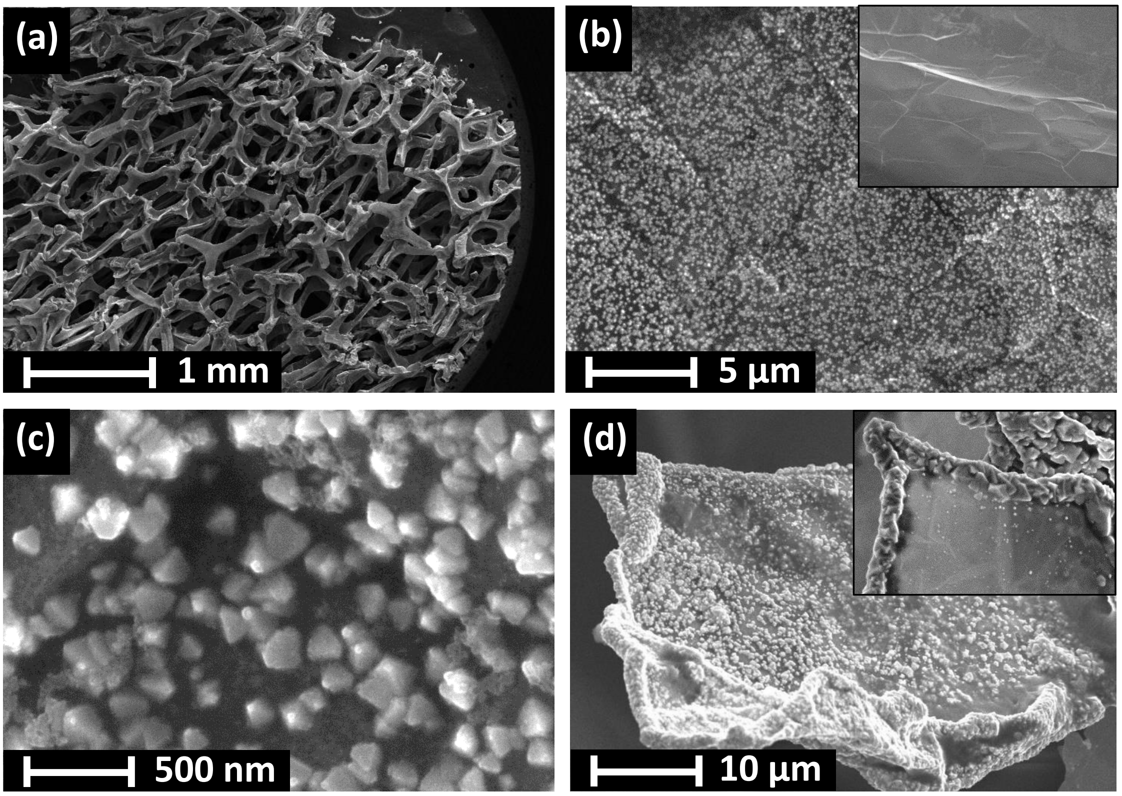

Fig. 28: SEM images of a Cu_2O/3D-GR composite (deposited with 1 C cm^{-2} charge density) at different magnifications. The inset on (b) shows the bare GR surface while in (d) it shows the structure of the composite formed without the pre-nucleation step.

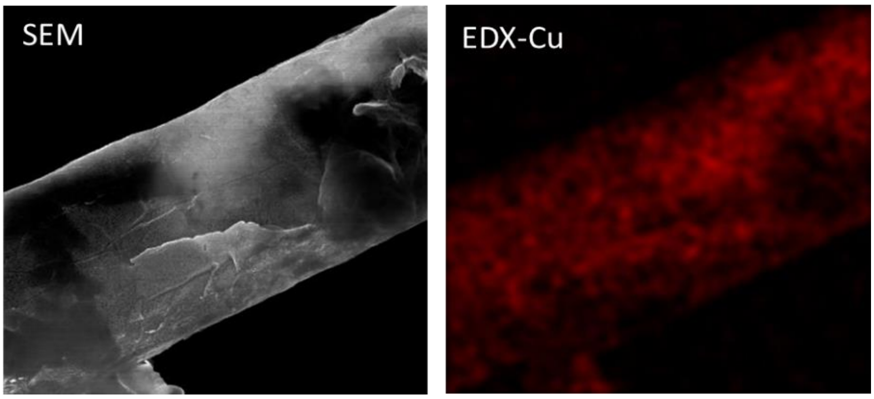

Fig. 29: SEM and EDX images of a Cu_2O/3D-GR composite deposited with 1 C cm^{-2} charge density.

Physical characterization was performed for all the prepared composite systems. The results were very similar for all the samples, confirming that there is no difference in the physico-chemical properties of the deposited Cu_2O in the different hybrid configurations. For the sake of brevity, we only present the results obtained for the Cu_2O/3D-GR composite and emphasize any differences for the other hybrids. XRD patterns of the Cu_2O/GR composites were recorded to identify the crystal structure and composition of the deposited oxide. The four most intense reflections of the Cu_2O can be recognized (**Fig. 30a**).[160]

Although the presence of some copper traces cannot be completely excluded, the fact that reflections related to copper cannot be identified confirmed that this amount was negligible, if any. XPS data also confirmed that no Cu was formed during electrodeposition of Cu_2O (see the lack of Cu (0) peak around 918.6 eV at the Auger spectrum, **Fig. 31**, and interestingly indicated the presence of some CuO (~20%), which might be the result of incipient oxidation of the sample surface in contact with air after synthesis).

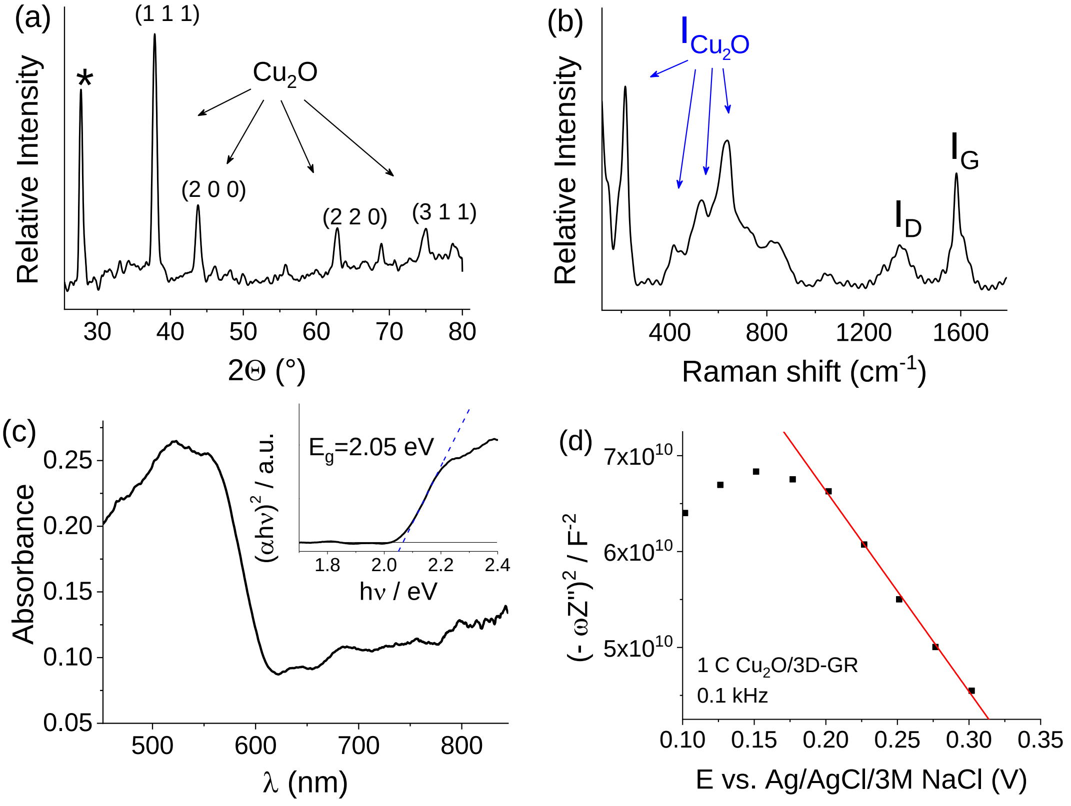

Fig. 30: (a) XRD pattern, (b) Raman spectrum (also for the bare 3D-GR sample), (c) Diffuse-reflectance UV-vis spectrum (together with Tauc representation as inset), and (d) Mott-Schottky plot (recorded in 0.1 M Na-acetate solution), of a Cu_2O/3D-GR composite, deposited with 1 C cm^{-2} charge density. The diffraction marked with asterisk in (a) corresponds to the GR substrate.

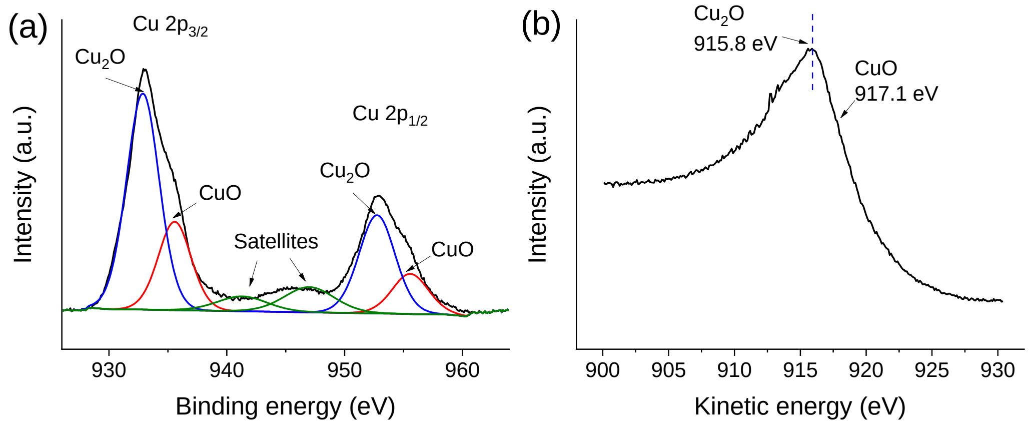

Fig. 31: Cu XPS (A) and LMM Auger (B) spectra, recorded for a Cu_2O/GR2 sample.

The appearance of the diffraction at 2θ = 27.8° (marked with asterisk in **Fig. 30a**) indicated that we have a multi-layer GR structure instead of a GR monolayer, as the CVD-grown 3D-GR samples typically consist of both one- and few-layer domains.[146] This observation is typical for CVD-grown 3D-GR samples and contributes to the mechanical stability of the 3D electrode.[161]

The Raman spectrum of the composite showed all the characteristic Raman active vibration modes of Cu_2O (**Fig. 30b**). The appearance of the peaks at 145, 220, 416, 532, and 631 cm^{-1} proves that Cu_2O was formed during the deposition.[159] The lack of the characteristic vibration modes of CuO at 297 and 350 cm^{-1} proved that the formed oxide is exclusively Cu_2O and not CuO (confirming XRD results).[162] At 1582.5 cm^{-1}, the G-band of the GR substrate, associated to the E_{2g} vibration mode of the sp^2 framework,[163] can be discerned on the Raman spectrum.[164] The presence of a very small D-band at 1374 cm^{-1} indicated that only trace amounts of defects were present. Importantly, these defects were already present before synthesis of the composites, as seen from the spectrum of the bare 3D-GR sample. The intense 2D band centered at 2698 cm^{-1} confirmed the few-layer character of the 3D-GR sample.

The optical bandgap of the Cu_2O/3D-GR composite was determined by diffuse reflectance UV-vis spectroscopy, and the spectrum was analyzed using a Tauc plot (see an example for the 3D-GR support in **Fig. 30c**). The determined E_g = 2.05 eV was in good agreement with values reported for Cu_2O.[165] Similar data were collected for all Cu_2O/nanocarbon samples (not shown here). The most important conclusions were the following: (i) the absorption of the samples did not alter with the varying GR content and (ii) there was a massively increased non-characteristic absorption related to GR (especially in the vis-NIR region[120,166]).

EIS measurements were carried out to determine the flatband potential of the composite (**Fig. 30d**). By performing the Mott-Schottky analysis on the measured data, a flatband potential of E = +0.51 V (vs. Ag/Ag/3M NaCl) was obtained for the Cu_2O/3D-GR sample, a value slightly higher compared to data reported for electrodeposited Cu_2O at neutral pH.[147,167] To compare the flatband potential (and thus the apparent Fermi level) of the various photoelectrodes, **Table 7** summarizes the onset potential of the photovoltammetry profiles, the open circuit potentials with and without illumination, and the flatband potential obtained from the Mott-Schottky plots. The most important trend observed in these comparisons was the slight positive shift in the flatband potential (apparent Fermi level) in the case of the composite samples (compared to the bare Cu_2O). The magnitude of this shift increased with increasing nanocarbon loading and had a maximum of 100 mV for the spray-coated carbons and 200 mV for the 3D-GR sample. These shifts indicate the intimate contact between the constituents, similar to trends in other studies in the literature on different SC/nanocarbon assemblies.[106,166]

Table 7: Comparison of the flatband potential obtained via different methods. For easier comparison, the potentials are compared at the RHE scale.

Support	OCP (dark) E vs. RHE (mV)	OCP (light) E vs. RHE (mV)	Photovoltammetry onset E vs. RHE (mV)	Flatband potential from Mott-Schottky E vs. RHE (mV)
ITO	447	622	747	1015
GR2	445	623	703	1016
GR3	436	618	717	1020
GR4	465	605	728	1104
CNT	415	620	696	1084
3D-GR			755	1230

5.1.3 Photoelectrochemical properties of the Cu_2O/nanocarbon electrode

To evaluate the PEC properties of the Cu_2O/GR composites, the photoreduction of CO_2 was performed as a model reaction of practical significance (**Fig. 32a**). The most important conclusions to be drawn from these initial measurements are the following: (i) The nanocomposite showed PEC activity towards CO_2 reduction, as confirmed by the enhanced photocurrents in the presence of CO_2 (note that the pH-effect was deconvoluted by performing control measurements in N_2 saturated solution, adjusted to pH = 4.0 with H_2SO_4, the pH of the CO_2 saturated solution); (ii) There was an increased photocurrent for the GR containing samples as compared to the bare oxide (**Fig. 32b**), and (iii) The overall shape of the photovoltammograms was similar in the presence/absence of the carbon scaffold, except the development of a dark current in the case of the hybrids. The photocurrent did not decrease after a certain potential; it was stable in the presented potential regime. Photoaction spectra (IPCE) vs. wavelength) were also recorded, and a massive increase in the IPCE values was observed on the photoaction spectrum (**Fig. 32c**). The identical wavelength threshold value confirmed that the enhanced photocurrents were not related to some new absorption or bandgap shift, but indeed to the better charge carrier extraction in the hybrid (note that the amount of Cu_2O was the same).

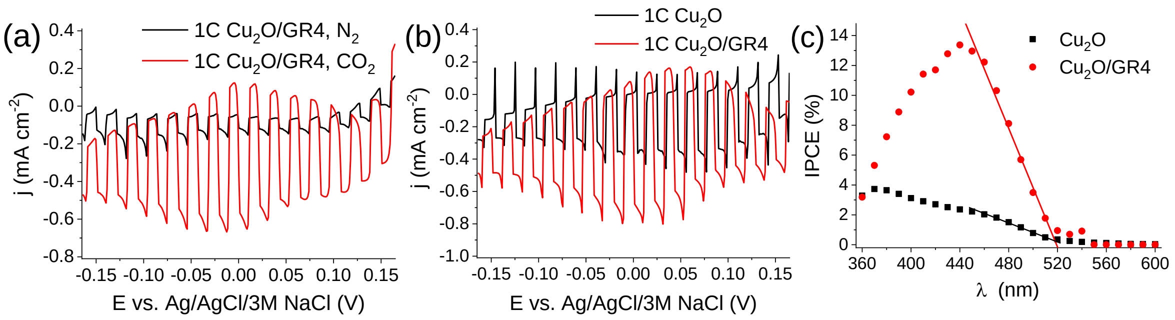

Fig. 32: Linear sweep photovoltammograms recorded for (a) a Cu$_2$O/GR4 hybrid sample (1 C cm^{-2} Cu$_2$O) in CO$_2$ or N$_2$ saturated 0.1 mol dm^{-3} Na$_2$SO$_4$, and N$_2$ saturated buffer solution, having the same pH as CO$_2$ saturated aqueous solutions (pH = 4.0). (b) Photovoltammetry curves for a Cu$_2$O/GR4 hybrid and a Cu$_2$O film (1 C cm^{-2} Cu$_2$O) in CO$_2$ saturated 0.1 mol dm^{-3} Na$_2$SO$_4$ solution. The sweep rate was kept at 2 mV s^{-1}, while the light-chopping frequency was 0.2 Hz. A solar simulator was used employing a UV cut-off filter (<400 nm). (c) Photoaction spectra for the two electrodes presented in (b), recorded at E = 0.0 V (vs. Ag/AgCl/3M NaCl) in CO$_2$ saturated 0.1 mol dm^{-3} Na$_2$SO$_4$ solution.

Long-term photoelectrolysis was performed at different potentials to assess the stability of the Cu$_2$O/GR electrode. As shown in **Fig. 33a**, even a 100 mV shift in the external bias potential can cause a massive alteration in the overall shape. Specifically, at E = –0.05 V, the rapid cessation of the photocurrents was seen, as a result of photocorrosion (i.e., formation of metallic Cu).[168] On the other hand, at E = +0.05 V, stable photoactivity was reached after an initial decrease. This enhanced PEC behavior is attributed to the dark re-oxidation of metallic copper moieties, formed via photocorrosion.[168] This hypothesis is supported by the initially observed dark anodic currents at this potential. Notably, a steady state was reached after 2.5 h, with stable photocurrents and minor dark currents.

To verify that the increased photocurrents in the presence of CO$_2$ (see **Fig. 32a**) were related to its conversion to useful products, aliquots were taken periodically both from the liquid and gas phases. Importantly, in the gas phase only minor traces of H$_2$ were detected and no CO formation was confirmed. As for the liquid phase, methanol, ethanol and minor amounts of formic acid were detected; similarly to earlier studies on Cu$_2$O-containing photoelectrodes. [169] Interestingly, while the ethanol concentration increased continuously, the methanol formation only started after the steady-state PEC behavior was reached (**Fig. 33b**). Quantitatively, the two alcohols accounted for a FE of 50-60% (with a 2:3 ratio for methanol/ethanol) while the rest of the charge was related to H$_2$ and formate production, and the photoreduction of Cu$_2$O to Cu as detailed above. Comparative studies were performed with a bare Cu$_2$O electrode, deposited with identical charge density. The formation of methanol and ethanol was witnessed, although with a different ratio. The relative amount of ethanol (vs. methanol) was smaller in the case of the bare oxide most likely because of the shorter residence time of the intermediate reduction products (vs. the case of the nanohybrid electrode). However, this process is complex, and several other factors (most importantly local potentials) may affect the product distribution, and this is not the focus of the dissertation.

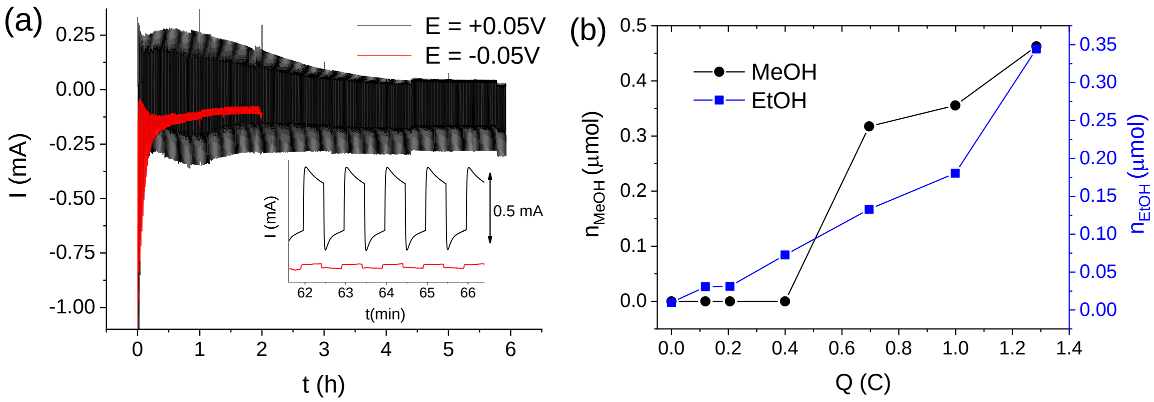

Fig. 33: (a) Long-term chronoamperometry data of two Cu_2O/GR4 electrodes with identical Cu_2O content (1 C), registered at E= +0.05 V and E= –0.05 V potential (vs. Ag/AgCl/3 M NaCl), in CO_2 saturated 0.1 M Na_2SO_4 solution. A solar simulator was used employing a UV cut-off filter (<400 nm). (b) Formation of alcohols during the photoelectrolysis presented in (a) at +0.05V potential. The x-axis shows the amount of charge passed during photoelectrolysis.

Degradation of the Cu_2O/3D-GR electrode structure during long-term photoelectrolysis is a relevant concern. We found that major degradation of the 3D structure only occurred when the photoelectrolysis was performed at more negative potentials, where water splitting (and thus H_2 bubble formation) also occurred. SEM images were taken for samples after photoelectrolysis (**Fig. 34**).

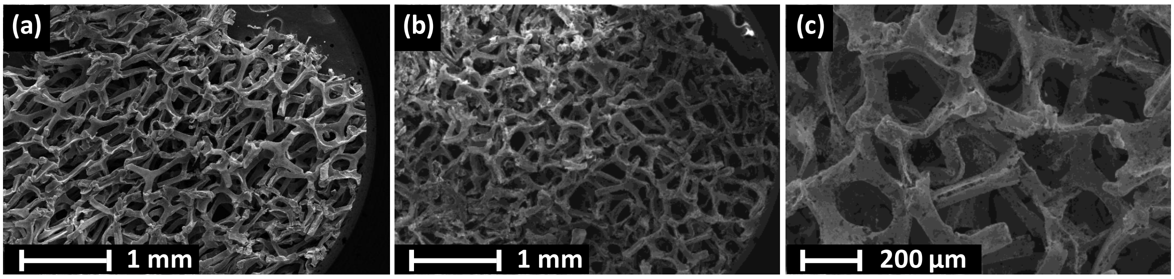

Fig. 34: SEM images of a Cu_2O/3D-GR photoelectrode before (a) and after (b, c) photoelectrolysis.

5.1.4 Factors behind the improved PEC properties

To explore a broad range of the composition and morphology, the effect of the GR thickness and the deposited Cu_2O amount were both varied systematically. **Fig. 35** compares the measured photocurrents (both the initial current spike and the stationary plateau; as shown in the inset of **Fig. 35a**) for the bare Cu_2O/ITO electrode and composites (GR supports of two different thicknesses and five different Cu_2O loadings for each support). As for the bare Cu_2O, there was a huge difference between the initial- and the stationary photocurrent values. This observation suggests the insufficient charge carrier extraction in the case of the bare oxide (see below for detailed discussion on this point). In addition, the stationary photocurrents seemed to be independent of the Cu_2O loading (film thickness), at least in the studied regime. This constant current suggests that the reacting photoelectrons come from a distinct surface region of the Cu_2O film, independently from the thickness. The overall pattern was totally different for the Cu_2O/GR composites: (i) The transient and the stationary values were much closer to each other, confirming our assumption that the highly conductive GR support facilitates effective charge separation and charge carrier extraction; (ii) The maximum photocurrent gradually shifts to higher Cu_2O loadings with increasing GR thickness. Similar experiments were carried out with the 3D-GR samples and the composition dependent PEC behavior was also confirmed. These trends suggest that there is in optimal composition (i.e., Cu_2O/GR ratio) in the hybrid configuration.

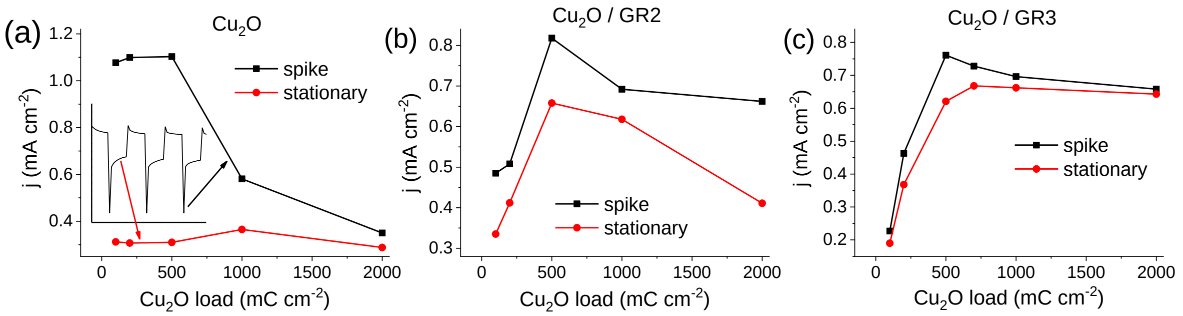

Fig. 35: Comparison of the transient and stationary photocurrents at E= +0.05 V, for five different Cu_2O loadings (100-2000 mC cm^{-2}), on (a) a bare ITO and (b-c) two different GR/ITO supports. The inset in (a) shows how the data points were determined. The lines among the data points serve only to guide the eye.

While the effect of GR thickness can be studied by comparing samples with identical Cu_2O content, their optical behavior might be different. In fact, this increased light absorption with higher GR thicknesses explains the decrease in the photocurrents at high GR thicknesses, where light absorption of Cu_2O is hindered by the presence of GR. This trend is also reflected in **Fig. 37**.

The question however, still holds: what are the reasons behind the improvement in the PEC properties? EIS measurements were performed to scrutinize the electronic properties of the synthesized photoelectrodes. From qualitative analysis of the Nyquist plots depicted in **Fig. 36a**, one can see the large decrease of semicircle size for the GR containing composites. Additionally, there is a higher series resistance for the Cu_2O/ITO sample compared to its GR containing counterparts (most likely rooted in the resistance of the Cu_2O/ITO interface). To quantify these trends an equivalent circuit (see the circuit and its description in the experimental, **Fig. 14**) was employed to fit the measured data (**Fig. 36b** and **c**). The most important conclusions are the following: (i) There was a huge decrease (from 500 Ω to 10 Ω) in the charge transfer resistance (R_{ct}) when Cu_2O was electrodeposited on the GR support instead of the bare ITO; (ii) When the GR thickness was increased the R_{ct} value also increased to 30 Ω, and then remained constant at higher GR thicknesses; (iii) The very high surface area of the hybrid electrodes was reflected in the high double-layer capacitance values (C_1, 10-30 mF cm^{-2}). Overall, these results confirm that the improved electrical conductivity, facilitating better charge carrier transport, is an important contributor to the superior PEC properties of the hybrid electrodes.

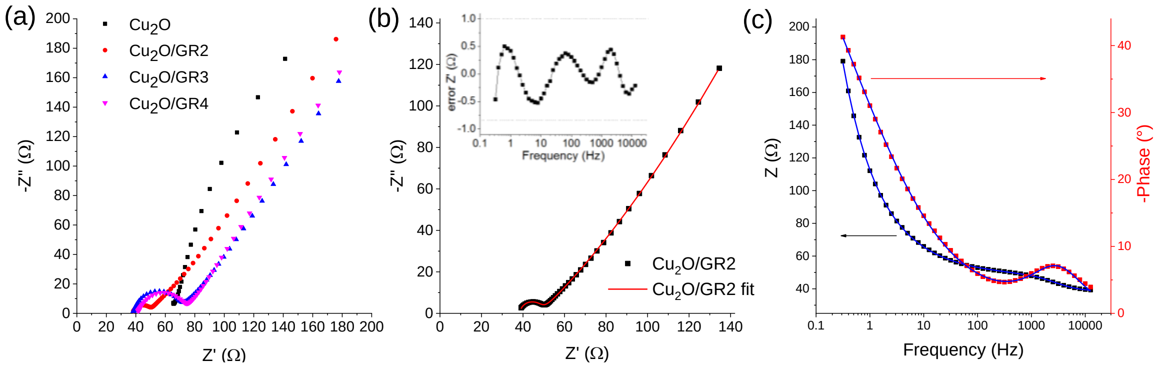

Fig. 36: (a) Nyquist plots recorded for pristine Cu_2O and three different Cu_2O/GR composites deposited with 1 C cm^{-2} charge density, in 0.1 M sodium acetate solution at open circuit potential, in the 0.1 Hz - 10 kHz frequency range. (b) Measured (points) and simulated (solid lines) Nyquist and (c) Bode-plots of a Cu_2O/GR electrode. The inset in (b) shows the error associated with the Bode plot fit (i.e., difference between the measured and calculated value).

To get a better understanding on the charge carrier recombination process, transient photocurrent measurements were performed.[111,154,170] In these measurements the photocurrent was followed after the light was switched on (chopped illumination). The first important observation in all experiments was the slow relaxation of the cathodic photocurrents (on the order of seconds, see **Fig. 37**). Similarly to previous water oxidation studies[111,154], this slow charge transfer can be attributed to the kinetically hindered, multi-electron nature of CO_2 reduction (i.e., it involves 6 e^- and 6 H^+ to form methanol). The competition between electron transfer to CO_2 at electrode/electrolyte interface and electron-hole recombination within the space charge layer and at the surface means that only a portion of the photogenerated electrons can react with CO_2. Consequently, the achieved solar-to-chemical conversion efficiencies are much smaller than what could be expected form the optoelectronic properties of Cu_2O. Extensive recombination is particularly problematic close to the Fermi level, and while higher external bias potentials can help to suppress it, there is a trade-off because of the needed additional energy input. Also note that the stability of the photoelectrode was much lower at higher bias potentials, see also in **Fig. 33**.

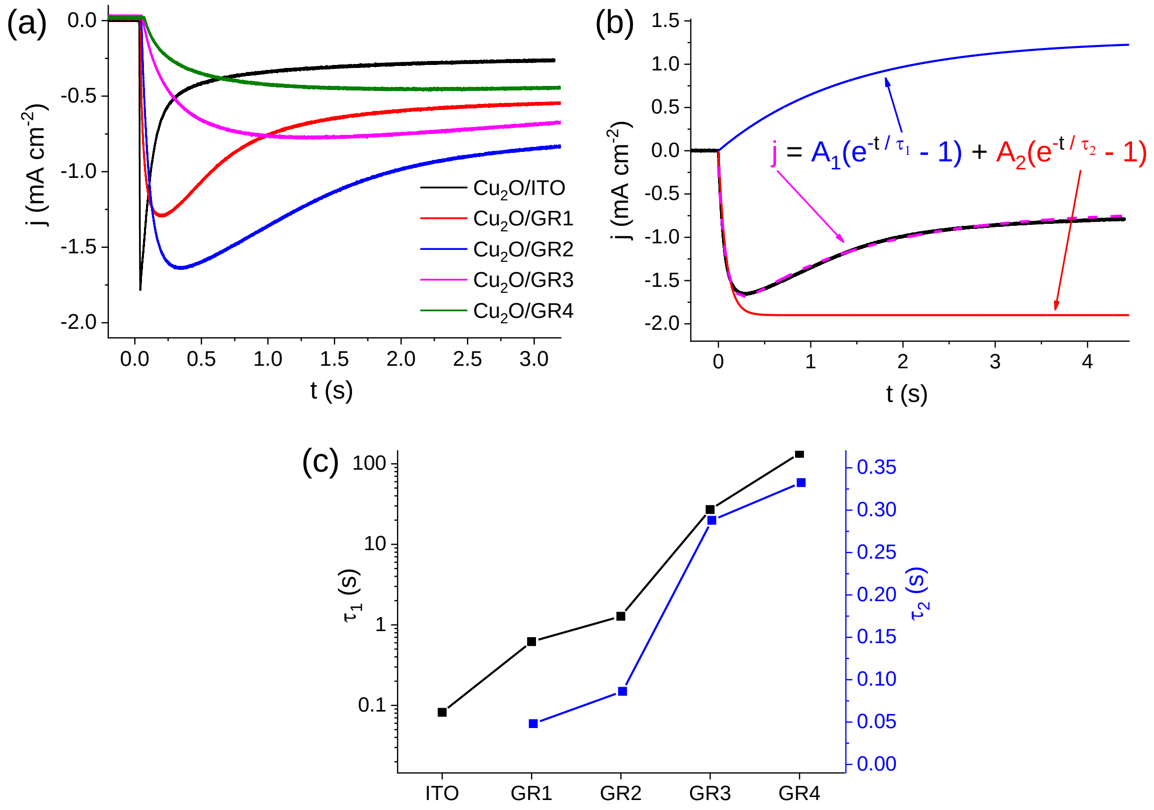

Fig. 37: (a) Photocurrent transients of a pristine Cu_2O/ITO film and four different Cu_2O/GR composites deposited with 0.5 C cm^{-2} charge density, in CO_2 saturated 0.1 M Na_2SO_4 solution at E = +0.05 V potential. A solar simulator was used employing a UV cut-off filter (<400 nm). (b) Dual exponential fit of a transient photocurrent response of the Cu_2O/GR2 sample. (c) Time constant values obtained for the samples shown in (a). The lines among the data points serve only to guide visualization.

Transient photocurrent curves recorded for the different samples are compared and contrasted in **Fig. 37a**. While for the bare Cu_2O there was a sharp transient, this feature gradually disappeared in the series of Cu_2O/GR samples with progressively higher GR content. As for Cu_2O, the photocurrent developed instantaneously after the light was turned on, followed by an exponential decay to a steady-state cathodic value. These cathodic photocurrent transients can be attributed to accumulation of the photogenerated electrons in the Cu_2O space charge layer and recombination of bulk holes with these electrons.[111,154,170] At longer timescales, a steady-state photocurrent was reached, the magnitude of which was dictated by the relative rates of recombination and charge transfer to redox species.[170]

As for the GR containing samples, the pattern was more complex. First, the initial spike got gradually smaller and finally disappeared as the GR thickness increased. Meanwhile, an opposite (i.e., increasing) pattern developed, dictated by charge carrier transport through the relatively thick Cu_2O/GR electrode architecture (note that no such behavior was observed for thin nanocarbon supports or bare Cu_2O, see also **Fig. 39** and **Fig. 38**). The relative contribution of these processes is clearly correlated with the GR content (note that the Cu_2O amount was identical in all cases). The ratio of the steady-state and the peak photocurrent increased with the GR thickness, because of the increasing magnitude of Cu_2O/GR junction area (see also **Fig. 35**). This suppressed recombination, however, did not result in constantly growing steady-state currents, mostly because of changing optoelectronic properties in the series of samples (i.e., light absorption of GR and increased resistance (see **Fig. 36**)).

To facilitate a semi-quantitative comparison, the transient photocurrent curves were fitted, and time constants were determined for all systems with different composition and morphology. The transient photocurrent curves could be well-fit to a sum of two exponential functions, one related to surface recombination (characterized by τ_1) and another one dictated by hole-transport through the electrode assembly (characterized by τ_2)[157] (see the fitted equation and an example of the fitting in **Fig. 37b**). While A_2 gives the absolute value of the maximum achievable photocurrent (i.e., in the absence of recombination), A_1 shows the maximal contribution of the recombination process to the decrease in the photocurrent. As seen in **Fig. 37c**, both time constants increased with the growing GR thickness, although at vastly different extents (note the logarithmic scale for τ_1). The time constant related to recombination increased rapidly with the higher GR thicknesses. Also note that the Cu_2O amount was fixed, therefore this trend is related to the gradually thinner Cu_2O coverage on the GR platelets.

Upon light irradiation the photogenerated electrons (minority carriers) are driven towards the electrode/electrolyte interface by band bending, while the holes are rapidly syphoned off by the GR phase (note that this process occurs on the nanosecond timescale).[171] As a net result, the time constant related to recombination increased three orders of magnitude for the composite sample with the highest GR content, compared to the bare Cu_2O film. On the other hand, τ_2 changed almost proportionally with the GR loading (thickness), which is not too surprising considering that this time constant is related to the transport of holes to the current collector (ITO). We also note here that there are several other processes which contribute to the charge carrier dynamics of the presented photoelectrodes. However, exciton generation, charge carrier separation in Cu_2O, and charge transfer from Cu_2O to GR occur on a much shorter (fs-ns) timescale, so that their effect cannot be important here.[120,172] From these results taken as a whole, we may conclude that both the enhanced specific surface area and improved charge carrier transport result in suppressed recombination, so that a higher fraction of the photogenerated electrons can react with CO_2.

The photocurrent transients of bare Cu_2O films were also studied. As seen in **Fig. 38a**, gradually larger τ_1 values were obtained with higher oxide thicknesses. The effect of CO_2 was also demonstrated, when higher steady-state photocurrents and τ_1 values were detected in the presence of CO_2 (compared to measurements in N_2 saturated solutions, **Fig. 38b**).

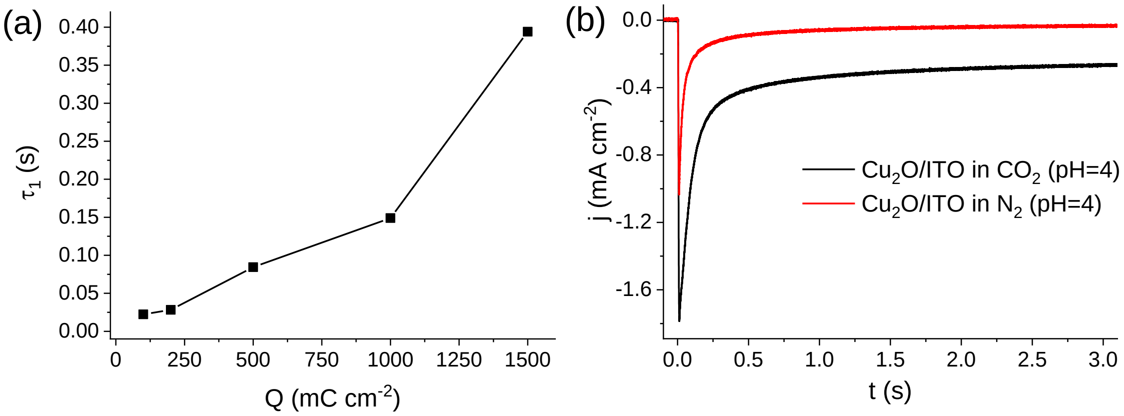

Fig. 38: (a) τ_1 values determined for Cu_2O/ITO films with different oxide thickness. (b) transient photocurrent measurements for a Cu_2O/ITO film (0.5 C cm^{-2}) in CO_2 or N_2 saturated 0.1 mol dm^{-3} Na_2SO_4, and N_2 saturated buffer solution, having the same pH as CO_2 saturated aqueous solutions (pH = 4.0, buffered with H_2SO_4).

5.1.5 Comparison of GR, 3D-GR, and CNT as photoelectrode support

Finally, to further elucidate the role of the nanocarbon scaffold and possible morphological aspects, the PEC behavior of different nanocarbon containing hybrid samples were compared. To deconvolute the effect of the different surface areas, samples with similar charge capacitance are compared in **Fig. 39**, and the slight differences in the surface area were considered by normalizing the photocurrent values (see also **Fig. 17** and **Table 6**). The Cu_2O content was identical in all cases (0.5 C cm^{-2}, with respect to the geometrical surface area). What is immediately striking is that steady-state currents on the three curves (Cu_2O, Cu_2O/CNT1, and Cu_2O/GR1) almost overlap after normalization, although they have significantly different time constants (slower recombination for CNT and especially the GR-containing composite, compared to the bare Cu_2O). These trends suggest that in these instances the improved PEC activity shown above (e.g., **Fig. 32** and **Fig. 35**) is predominantly rooted in the increased surface area (and the resultant high Cu_2O/carbon junction area), provided by the highly conductive nanocarbon scaffold. After factoring out this effect, very similar behavior is seen, at least in terms of the steady-state photocurrents.

On the other hand, much higher normalized steady-state photocurrent flow could be seen for the 3D-GR support, most likely because of the superior charge transport properties rooted in the lack of particle-particle interfaces (also consider that the size of GR platelets is much higher in this case, compared to the spray-coated samples, see **Fig. 28** and **Fig. 26**). Note that while this support had relatively small surface area, at the same time, it has a higher thickness. This manifested in the large time constant for the photocurrent development (τ_2).

Finally, we recognize that the light penetration depth was limited in this macroscopic architecture. Consequently, design of other 3D architectures, where benefits of the presented 3D-GR structure could be maintained while simultaneously ensuring sufficient light harvesting, would be highly desirable in the future.

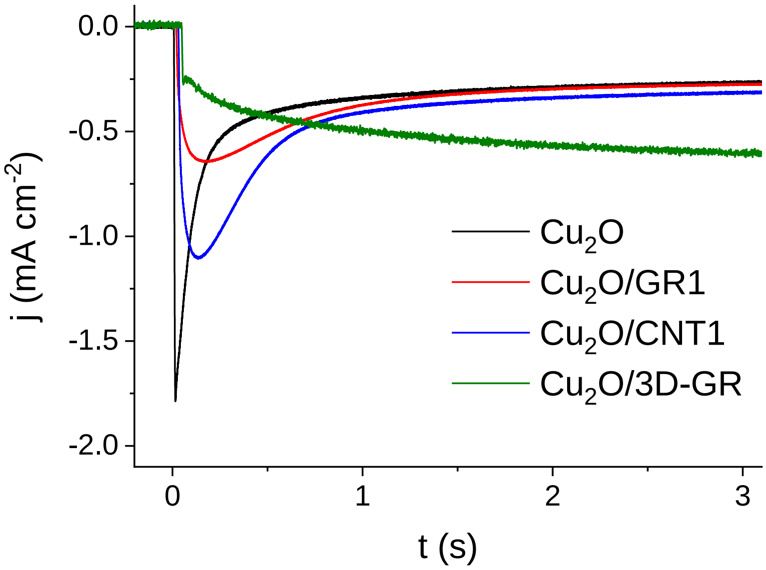

Fig. 39: Photocurrent transient analysis of a pristine Cu_2O film and three different Cu_2O/nanocarbon composites deposited with 0.5 C cm^{-2} charge density. The measurements were performed in CO_2 saturated 0.1 M Na_2SO_4 solution at E = +0.05 V potential. A solar simulator was used employing a UV cut-off filter (<400 nm). Photocurrent normalization was performed using the relative surface area data in **Table 6**.

5.2 Electrodeposition of nanocrystalline TiO_2 films on graphene scaffolds

5.2.1 The effect of electrodeposition conditions on the properties of TiO_2 films

All TiO_2 layers were synthesized by oxidative electrodeposition from aqueous $TiCl_3$ solution using different electrochemical protocols. A linear sweep voltammogram was recorded to identify the potential region where Ti^{3+} species can be oxidized (**Fig. 40a**). The onset potential of the oxidation process is at −0.7 V, which is below the redox potential of the reduction of dissolved dioxygen at this pH. [173] This process could proceed in parallel to the electrodeposition, leading to both lowered current efficiency and the formation of different dioxygen reduction products, which can interfere with TiO_2 formation. Consequently, removal of oxygen species from the solution is a prerequisite for maintaining solution stability and to achieve high-quality electrodeposits in a reproducible way (i.e., Ar purging).

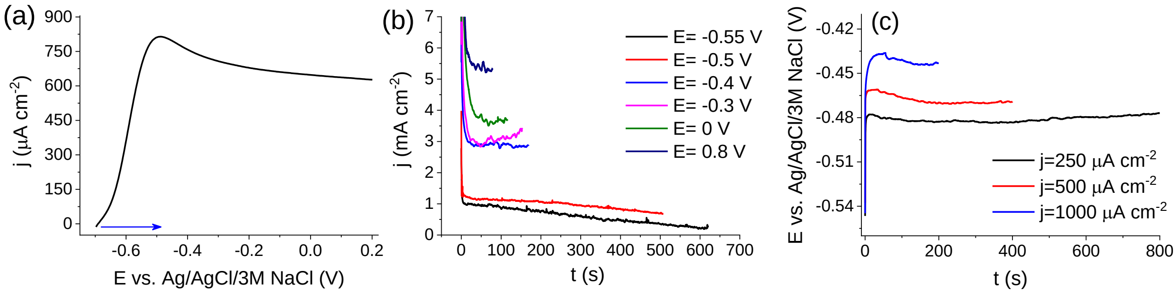

Fig. 40: Linear sweep voltammogram, recorded at 50 mV s^{-1} scan rate, in 50 mM $TiCl_3$ solution at pH = 2.0 and room temperature, using a GC working electrode (a). Potentiostatic deposition curves, recorded in the same solution at 80 °C, using a GC working electrode, Q = 200 mC cm^{-2} (b). Galvanostatic deposition curves, recorded under the same conditions as in (b), using different current densities, Q = 200 mC cm^{-2} (c).

The electrodeposition was performed both potentiostatically (**Fig. 40b**) and galvanostatically (**Fig. 40c**). In the first case, the selected deposition potentials spanned through the whole polarization curve, starting from the kinetically controlled region (from −0.7 V to −0.5 V), up to the mass-transport limited regime (above −0.5 V). In the case of galvanostatic measurements, the current densities were chosen according to the current values measured in the previous case. The role of the electrochemical procedure will be discussed later; first we present the effect of the solution pH and temperature on potentiostaticaly formed layers. The pH of the deposition solution was varied in the range of pH = 1–3. When the pH was further increased, a dark-colored precipitate formed in the solution, while at lower pH values the deposition always resulted in an amorphous and inhomogeneous product on the GC surface, regardless of the other parameters, therefore these pH regions were not studied further.

Solution temperature can also affect the outcome of the reaction, therefore we identified the products first with Raman spectroscopy. Analyzing the deposit formed at room temperature (**Fig. 41a** and **b)** in pH = 2 and in pH = 3 solutions, only those bands appeared that belong to the GC electrode (D and G bands at 1346 and 1600 cm^{-1}, respectively).[174] At 60 °C, weak Raman signals were spotted at 165 and 632 cm^{-1}, which became more pronounced when the temperature was elevated to 80 °C. These peaks, together with the lower intensity peaks at 245 and 443 cm^{-1}, were contributions from the rutile and anatase phases, proving the deposition of crystalline TiO_2.[175] Notably, the presence of brookite minority phase cannot be ruled out or confirmed by these measurements. Further increasing the temperature (95 °C), the quality of the deposited film did not improve (mostly because the deposition solution become unstable). For further measurements, we synthesized the samples at the optimum temperature (80 °C). An interesting and important aspect of the two set of spectra was that the ratio of the bands related to the rutile and anatase phases differed notably in the two cases (**Fig. 41c**), suggesting that the pH of the solution influenced the phase composition of the forming TiO_2.

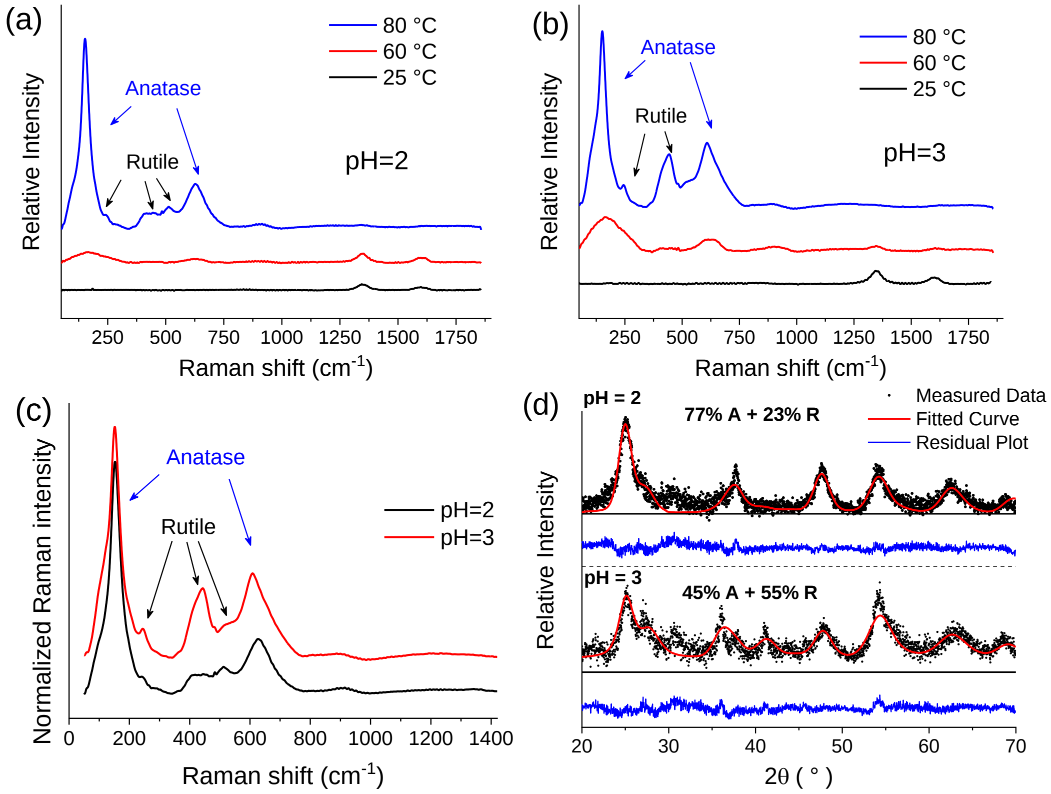

Fig. 41: Raman spectra of the TiO_2 layers deposited on GC working electrodes at E = 0 V, from the aqueous solution of 50 mM $TiCl_3$ at pH = 2.0 (a) and pH = 3.0 (b), at different solution temperatures, Q = 200 mC cm^{-2}. Comparison of the Raman spectra (c) and Rietveld-refined XRD pattern (d) of the samples deposited under otherwise identical conditions in 80 °C deposition temperature, but at different pH.

The phase composition of the samples was further characterized by XRD (**Fig. 41d**). The increased solution pH led to an increase rutile/anatase ratio. As derived from Rietveld refinement of the XRD patterns, the rutile/anatase ratio was about 1:1 at pH = 3. Interestingly, an anatase/rutile ratio of 3:1 was obtained at pH = 2, which is very similar to that of Aeroxide P25, the most commonly applied benchmark TiO_2. For note, the diffraction at 2Θ ≈ 31 ° indicated the presence of a brookite minority phase in the samples, which could however not be quantified by the Rietveld-refinement due to the small amount. The crystallite size was estimated to be 6–7 nm at both pH values, which were calculated with the help of the Scherrer equation.

The structure and morphology were studied by SEM and TEM. The deposits always had a porous, sponge-like structure on the GC electrodes (**Fig. 42a**). This interconnected structure was made of small particles (~10 nm), agreeing well with the crystallite size estimated from XRD measurements. These observations were further supported by TEM images (**Fig. 42b**), where fused, <10 nm-sized nanoparticles were identified. Crystal lattice fringes can be observed for almost all primary nanoparticles, verifying the high crystallinity of the deposits – in good accordance with the XRD and Raman data.

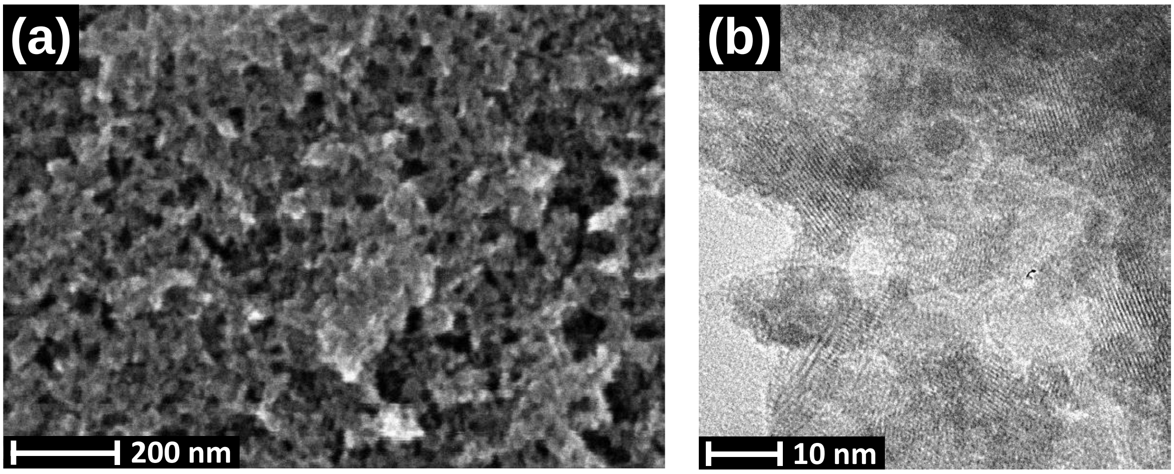

Fig. 42: SEM (a) and TEM images (b) taken for a TiO_2 layer, deposited on a GC electrode ($c(TiCl_3)$ = 50 mM; T = 80°C, pH = 2.0, Q = 200 mC cm^{-2}, and j = 100 µA cm^{-2}).

5.2.2 PEC behavior of deposited TiO_2 photoelectrodes

The electrodes formed at room temperature showed negligible photocurrents indicating the formation of a non-crystalline product (**Fig. 43a**), (in accordance with Raman and XRD data). The photocurrent increased with the temperature of the deposition bath. The photovoltammograms recorded for the samples prepared at T = 80 °C showed a typical shape for crystalline TiO_2 films.[176,177] The onset potential of the photocurrent was −1.05 V, in a good agreement with values reported in the literature.[176,178] The maximum photocurrent value was strongly dependent on the pH of the deposition solution, having a maximum at a pH = 2 (**Fig. 43b**). Careful inspection of these curves revealed further differences: (i) the onset potential of the process and therefore the flatband potential of the deposited TiO_2 was different (ii) the current plateau was reached at different potential values – both in line with our previous conclusions, namely that the phase composition of the electrodeposited TiO_2 can be tuned by adjusting the pH of the deposition solution.

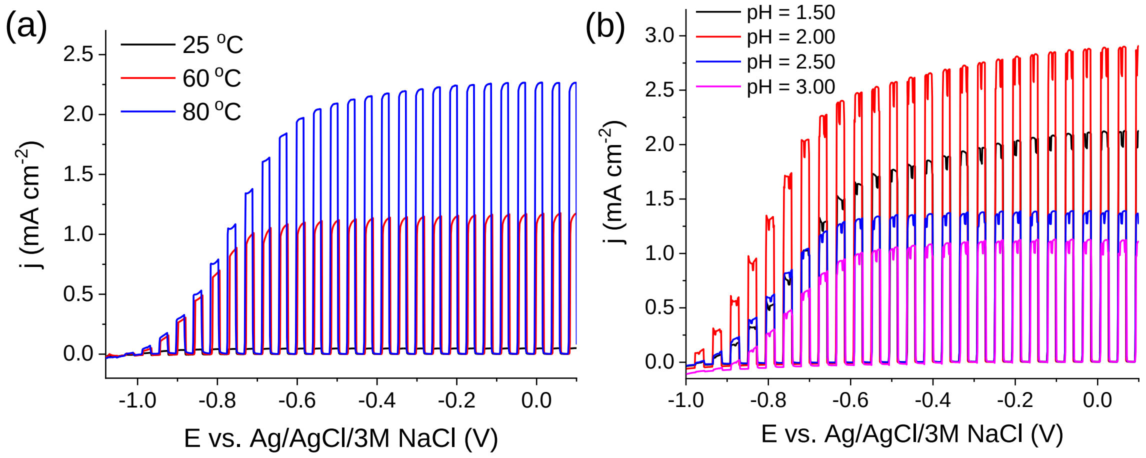

Fig. 43: Typical photovoltammogram of a TiO_2 layer electrodeposited at different bath temperatures (a) 50 mM $TiCl_3$ at pH = 2.0, j = 100 µA cm^{-2}, Q = 200 mC cm^{-2}. Linear sweep photovoltammetric curves, recorded for TiO_2 layers deposited from a 50 mM $TiCl_3$ solution at different pH values (b) j = 100 µA cm^{-2} and Q = 200 mC cm^{-2}, T = 80 °C. All measurements were performed in 0.1 M Na_2SO_3 solution, with a sweep rate of 2 mV s^{-1} and light interruption frequency of 0.1 Hz.

The effect of the deposition current density on the maximum photocurrent was studied at a fixed deposition charge density to ensure identical film thickness (**Fig. 44a**). The highest photocurrents were recorded for the samples obtained with moderate deposition current densities (j = 100 µA cm^{-2}). This trend can be attributed to the followings: (i) at very low current densities the deposition time was longer and hence solution instability had a negative effect (ii) at low current densities the contribution of unwanted electrochemical processes (i.e., dioxygen reduction) can be significant, thus decreasing the current efficiency (iii) at very high current densities (at more positive potentials) other electrochemical processes (e.g., oxidation of the substrate) may decrease the current efficiency. Similar optimization was performed for the potentiostatic deposition as well (**Fig. 45a** and **b**), and the best PEC performance was found for the layers formed at a moderately negative potential (i.e., E = −400 mV).

The PEC activity of the layers also showed a maximum-type dependency on the deposition charge density (i.e., film thickness, **Fig. 44b**) when a fixed current density was applied. At low charge densities, incomplete substrate coverage and the thin layer were limiting factors, while at large charge densities optical/electrical shielding of the layer, mechanical instability, and solution instability (because of long deposition times) were the key aspects.

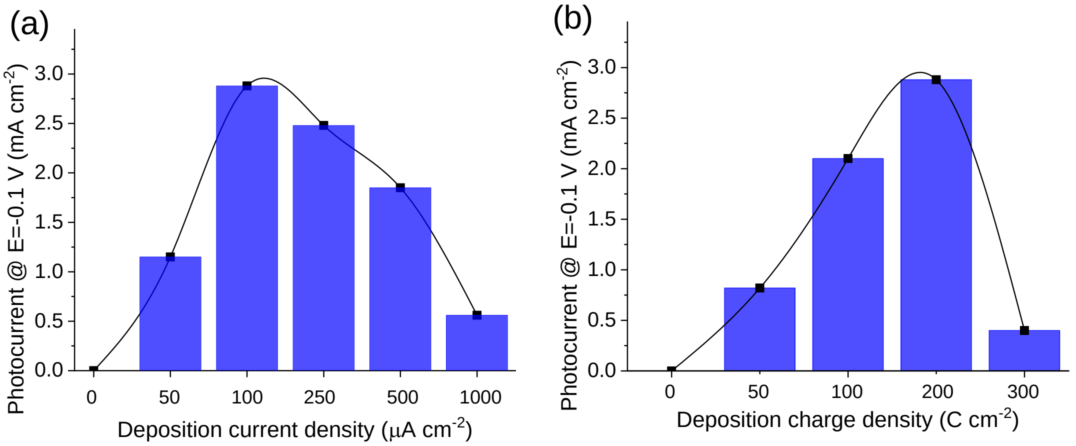

Fig. 44: Maximum photocurrents measured for TiO_2 layers deposited from a 50 mM $TiCl_3$ solution at 80 °C and pH = 2.0 at different current densities and Q = 200 mC cm^{-2} (a). Different charge densities in the same deposition condition and at j = 100 μA cm^{-2} (b). The lines connecting the data points only serve to guide the eye.

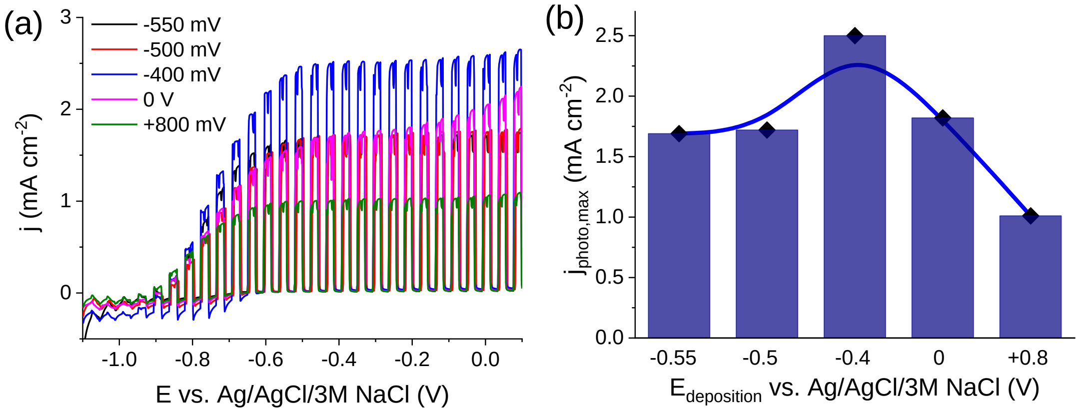

Fig. 45: Linear sweep photovoltammograms of TiO_2 layers, deposited on a GC electrode at T = 80 °C, from a 50 mM $TiCl_3$ solution at pH = 2, by applying different deposition potentials, with Q = 200 mC cm^{-2} (a). The measurements were performed in 0.1 M Na_2SO_3 solution (2 mV s^{-1} sweep rate, 0.1 Hz light chopping frequency). Comparison of the maximum photocurrents in function of the deposition potential (b), as derived from (a). The line between the data points serves only to guide the eye.

5.2.3 Comparison of the PEC activity of electrodeposited TiO_2 films with commercial Aeroxide P25

To have a direct measure on the performance of the electrodeposited samples, commercially available Aeroxide P25 samples were studied under otherwise identical conditions. The P25

TiO_2 NPs were spray-coated on GC electrodes from an ethanol based solution (5 g dm^{-3}), and subsequently sintered at 200 °C for 30 min. The number of spray-coating cycles was varied to find the optimal thickness of the layer (**Fig. 46**). The layer with the optimized thickness then was compared to the electrodeposited sample (**Fig. 47a**).

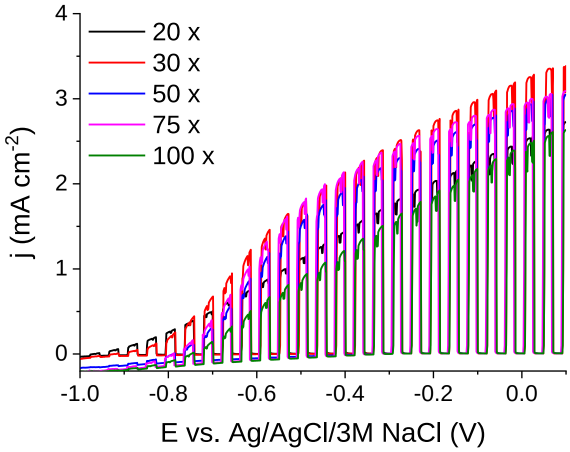

Fig. 46: Linear sweep photovoltammetric curves recorded for P25 TiO_2 layers of different thickness, formed by spray coating on GC electrodes. The measurements were performed in 0.1 M Na_2SO_3 solution, with a sweep rate of 2 mV s^{-1} and light interruption frequency of 0.1 Hz.

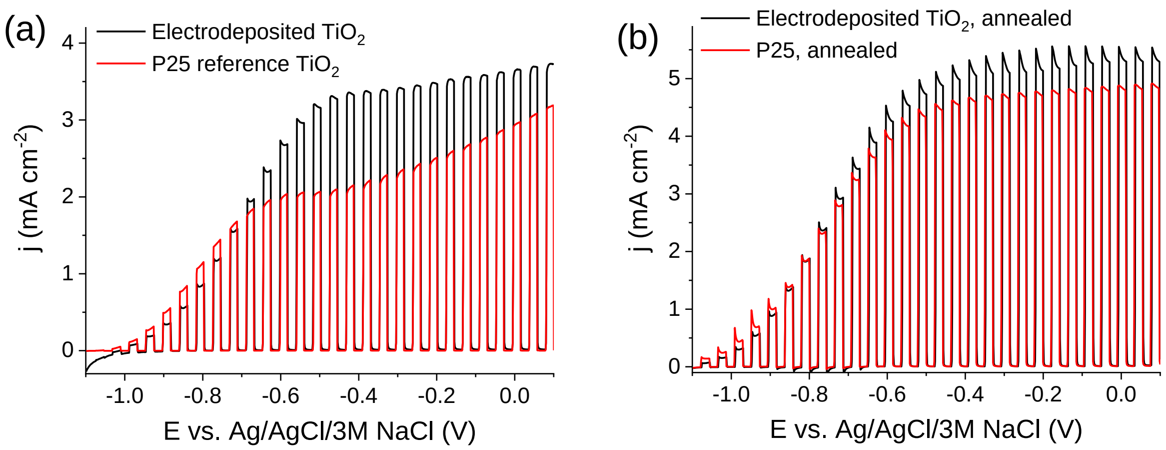

Fig. 47: Linear sweep photovoltammetric curves of a P25 TiO_2 layer and an electrodeposited TiO_2 layer before (a) and after (b) subsequent heat treatment (t = 2 h, T = 350 °C), recorded in 0.1 M Na_2SO_3 solution recorded with a sweep rate of 2 mV s^{-1} and light interruption frequency of 0.1 Hz. The electrodeposited layer was formed from a 50 mM $TiCl_3$ solution (pH = 2, j = 100 µA cm^{-2}, Q = 200 mC cm^{-2}).

Comparing the maximum photocurrent values, we note that the electrodeposited TiO_2 layer outperformed the P25 reference material by ~10%. Furthermore, the saturation photocurrent was reached at more negative potential in the case of the electrodeposited sample, indicating a better charge carrier extraction. This can be explained by the intimate connection between the substrate and the nanoparticles and among the individual crystallites forming the sponge-like structure. When the layers were subjected to an additional heat treatment (*t* = 2 h, *T* = 350 °C), there was a notable increase in the photocurrents both with the P25 sample and the electrodeposited TiO_2 layers (**Fig. 47a** and **b**). This photocurrent enhancement is predominantly rooted in the improved crystallinity and evolving interconnections between particles. After this anneal step, the layers deposited at 60 °C showed very similar results (**Fig. 48a** and **b**), but this increase in the photocurrent no longer occurred in the samples deposited at lower temperatures.

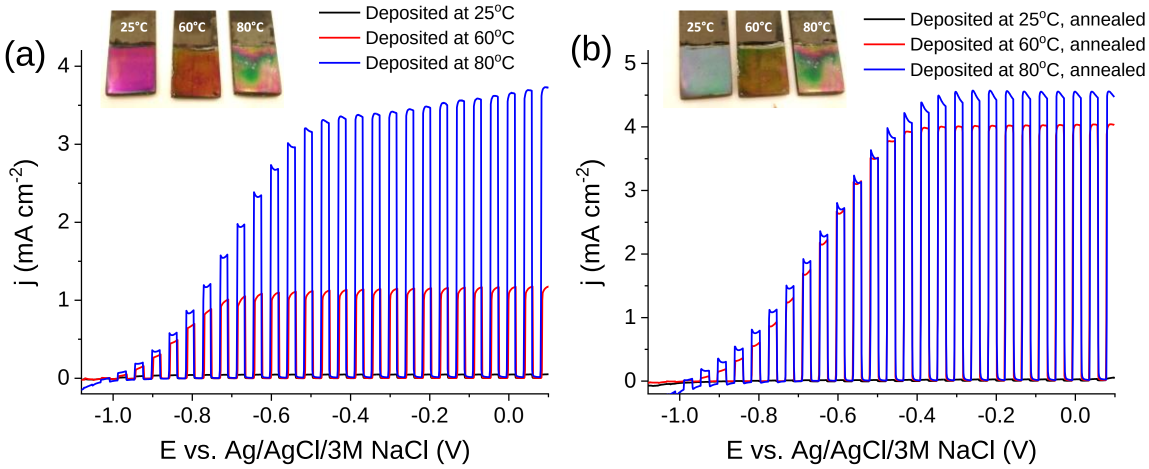

Fig. 48: Linear sweep photovoltammetric curves, recorded for TiO_2 layers electrodeposited at different solution temperatures (50 mM $TiCl_3$ solution, pH = 2, j = 100 μA cm^{-2} and Q = 200 mC cm^{-2}) before (a) and after (b) 2h annealing at T = 350 °C in air. All these measurements were performed in 0.1 M Na_2SO_3 solution, with a sweep rate of 2 mV s^{-1} and light interruption frequency of 0.1 Hz. The inset images show the appearance of the layers before and after annealing process.

5.2.4 Electrodeposition of TiO_2 on spray-coated graphene nanoplatelets

One of the greatest advantage of direct electrodeposition compared to ex situ physical composite fabrication techniques (e.g., drop-casting or spray-coating) is its capability for immobilizing the given material homogeneously on complex, uneven surfaces. To demonstrate this feature, the formerly optimized and presented galvanostatic electrodeposition protocol was applied to spray-coated GR electrodes. SEM images confirmed the formation of a coherent, porous coverage (**Fig. 49**). Very similarly to the case of GC electrodes, the TiO_2 film was assembled from ~10 nm sized grains. The thickness of the oxide film was homogenous on the GR platelets and most importantly, no uncoated places were discovered. Furthermore, the TiO_2 shell thickness increased gradually with the deposition charge density (see the series of images in **Fig. 49**). As a reminder, the amount of GR spray-coated on GC in the presented samples is the same as the amount (and marking) used in the Cu_2O/GR chapter: GR3 - 250 μg cm^{-2}. TEM images also confirmed the same structure, i.e., the TiO_2 nanoparticles evenly coated the GR flakes. Images taken at higher magnifications confirmed that the layer was assembled from less than 10 nm sized crystalline nanoparticles (**Fig. 50**).

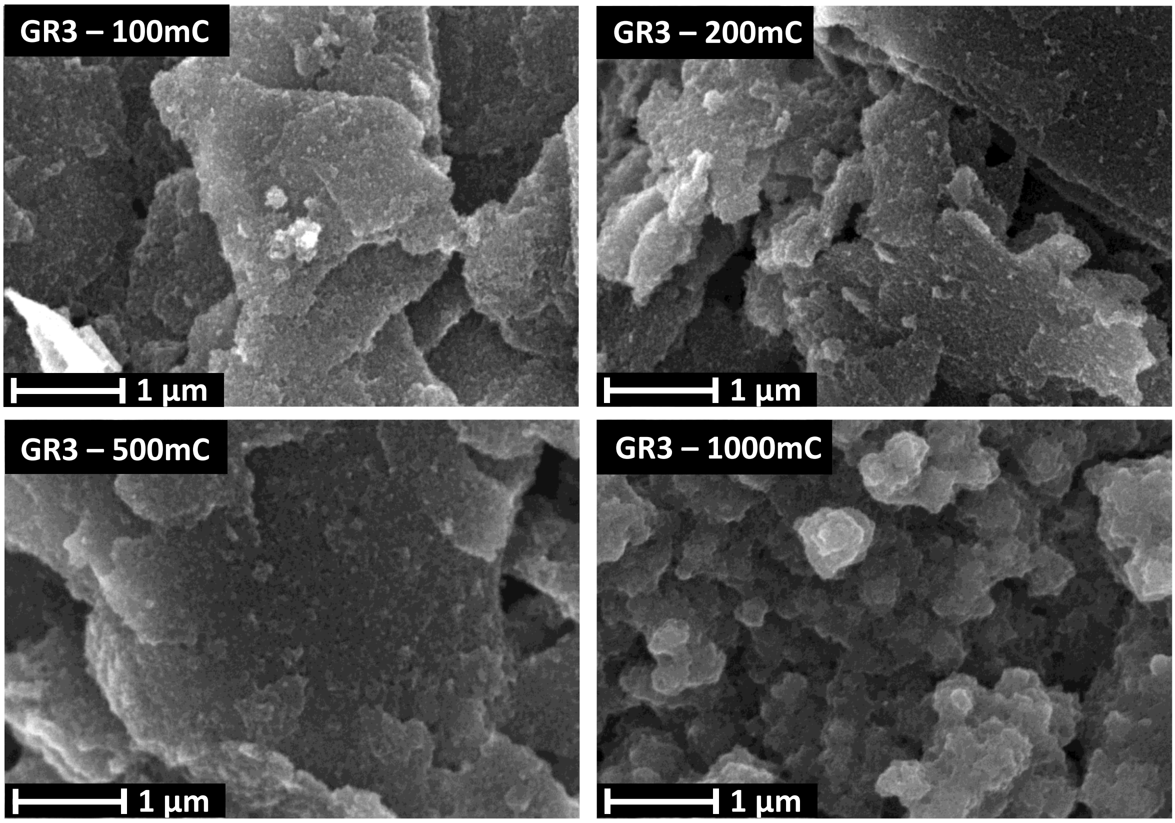

Fig. 49: SEM images of TiO_2/GR3 composites with different TiO_2 loading, deposited at 80 °C, from a 50 mM $TiCl_3$ solution, pH = 2, Q = 100–1000 mC cm^{-2}.

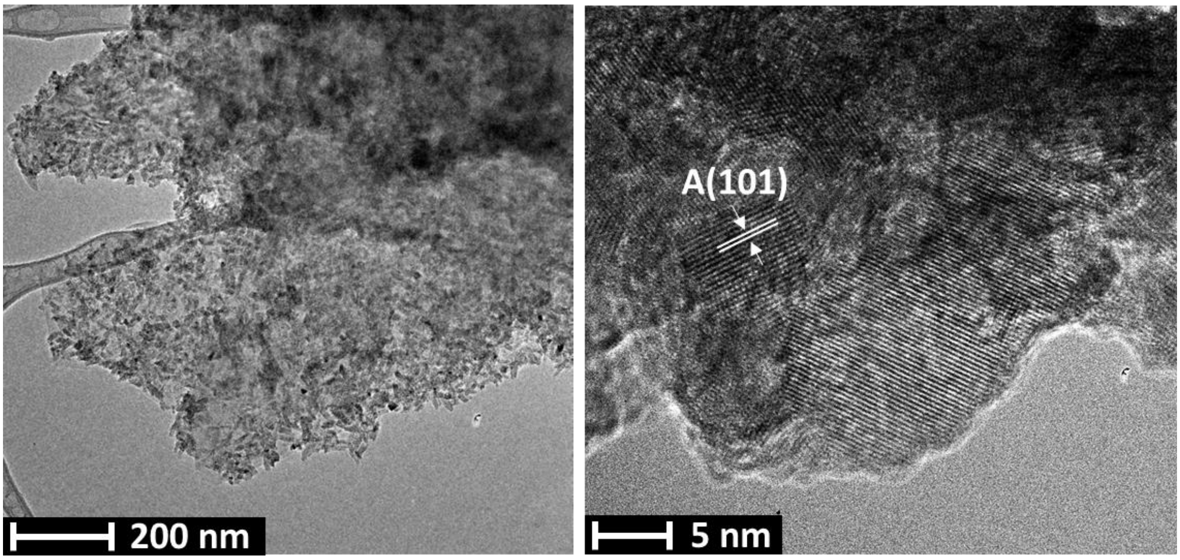

Fig. 50: TEM and HR-TEM images of a TiO_2/GR3 composite deposited from a 50 mM $TiCl_3$ solution (T = 80 °C, pH = 2.0, Q = 200 mC cm^{-2} and j = 100 µA cm^{-2}).

5.2.5 PEC behavior of TiO_2/graphene nanocomposite electrodes

The PEC behavior of TiO_2/GR nanocomposite photoelectrodes, was studied by linear sweep photovoltammetry. However, no photocurrent increase was observed for the GR containing electrodes, in fact, photocurrents were slightly lower than those observed for the pristine TiO_2 films (electrodeposited using the same conditions). The PEC behavior improves with an additional heat treatment (t = 2 h, T = 350 °C), but still does not reach the values measured for non-GR-containing samples (**Fig. 51** compared to **Fig. 48a** and **b**). This may be because TiO_2 alone is an excellent photoelectrode material with good charge separation and charge transport behavior that the additional GR scaffold can no longer further enhance (not as in the already presented the Cu_2O/GR photoelectrodes). Besides that, the parasitic light absorption of GR in the composite samples may contribute to the observed decrease in photocurrent also.

Due to these results, we wanted to study an n-type SC, where the PEC properties can be substantially improved by forming its nanocarbon containing composite electrode. Therefore, our interest turned to hematite (α-Fe_2O_3).

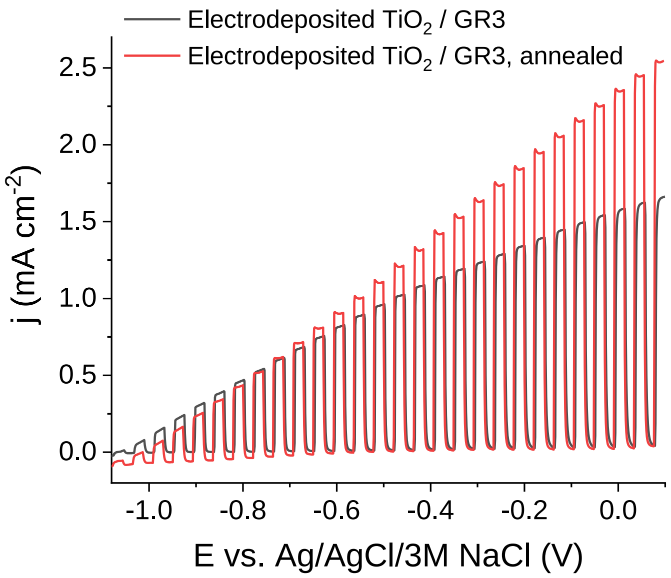

Fig. 51: Linear sweep photovoltammetric curves, recorded for TiO_2 / GR3 layers (50 mM $TiCl_3$ solution at 80 °C, pH = 2, j = 100 µA cm^{-2} and Q = 200 mC cm^{-2}) before and after 2h annealing at T = 350 °C in air. All these measurements were performed in 0.1 M Na_2SO_3 solution, with a sweep rate of 2 mV s^{-1} and light interruption frequency of 0.1 Hz.

5.3 Photoelectrochemical properties of hybrid n-type α-Fe_2O_3/graphene photoelectrodes

5.3.1 Electrodeposition of Fe_2O_3 on FTO and graphene platelets

In the first step, GR nanoflakes were spray-coated on an FTO-coated glass, from their ethanol-based suspension (very similar way to what we did in the preparation of the Cu_2O/GR photoelectrodes, only we used an FTO instead of an ITO that can withstand high temperature heat treatment during the hematite synthesis.). The amount of the spray-coated GR was *held constant* throughout this study, namely: the electrochemically accessible surface area of GR was approximately three-times higher compared to a bare FTO electrode. Prior to the electrodeposition of β-FeOOH, a conditioning step was carried out in the electrodeposition solution, to ensure the proper wetting of the GR nanoflakes and to remove any entrapped gas from the. This step was followed by the electrodeposition of β-FeOOH on the GR surface, using a cathodic electrodeposition procedure adapted from the literature, where the deposition electrolyte solution contained the aqueous solution of $TiCl_4$ for Ti-doping (quick reminder: doping of Fe_2O_3 with Ti can significantly increase the charge carrier mobility and concentration [110]). The final step was a two-step heat treatment of the electrodes, first under air (at 520 °C for 30 min) and secondly under Ar (at 700 °C for 30 min) to transform β-FeOOH to α-Fe_2O_3. The thickness of the deposited Fe_2O_3 (or in other words, the composition of the hybrid electrodes due to fix GR loading) was precisely tuned by varying the electrodeposition charge density. Pristine Fe_2O_3 layers were also synthesized on bare FTO as a comparison. Since the thickness of Fe_2O_3 can greatly influence PEC properties (e.g., insufficient light absorption for thin layers, higher degree of recombination for thicker layers) synthesis conditions were chosen in a way to make results obtained for bare Fe_2O_3 and its GR-containing counterparts fully comparable. Therefore, the electrodeposition charge densities were *normalized by the real surface area*, thus the Fe_2O_3 layer thicknesses were identical both in the case of the pristine and the GR-containing photoelectrodes. For example, the layer deposited with 450 mC cm^{-2} charge density on FTO was compared with a layer deposited with a charge density of 1350 mC cm^{-2} on the GR film, because of the three-fold surface area, so that the thickness of the hematite is similar in the two cases.

Elemental composition of Fe_2O_3 surface was determined with XPS. According to the survey scans (**Fig. 52**), all Fe_2O_3 samples contains Fe, O, Ti and Sn (besides adventitious carbon). To quantify the amount of each element, high resolution scans were also recorded

(**Fig. 53**). The surface of the Fe_2O_3 sample mostly consist of O atoms (79.8 at%), which is followed by Fe (16.3 at%). The amount of Ti was around 3.0 at%. The positions of the Ti 2p peaks suggest that Ti is present in the sample as Ti^{4+}. Similar conclusions apply for Sn, which is present in as small amount as 0.9 at%. The presence of Sn can be explained by the temperature of the second heat treatment step, which allowed the diffusion of Sn from the underlying FTO to the Fe_2O_3 lattice. [118,179]

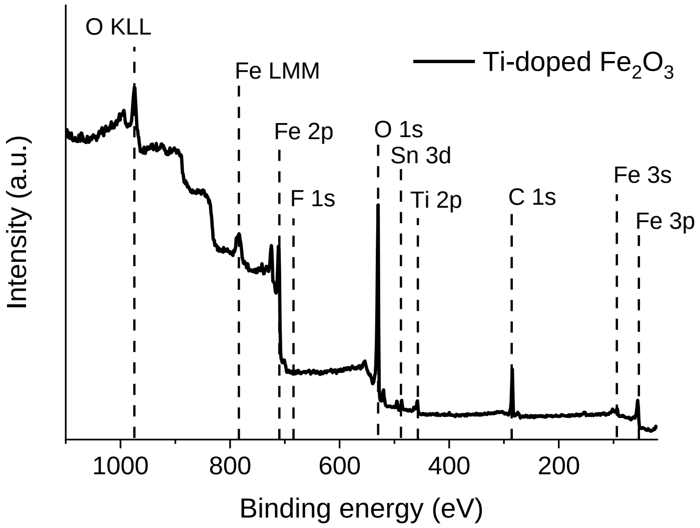

Fig. 52: Survey XPS scans recorded for the deposited Ti-doped Fe_2O_3.

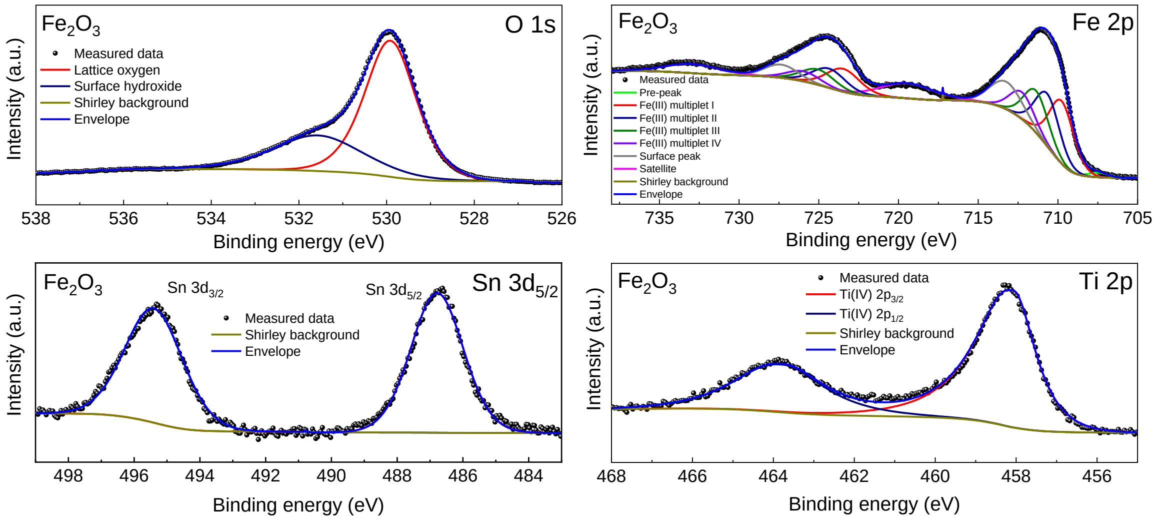

Fig. 53: High resolution XPS data recorded for the deposited Ti-doped Fe_2O_3.

Morphological characteristics of the bare Fe_2O_3, GR and the nanocomposite films were first studied by SEM. Images taken of pristine Fe_2O_3 are presented in **Fig. 54**. The nanostructured Fe_2O_3 layer consists of granular, oval-shaped particles, with an average size of ≈ 100 nm, homogeneously coating the FTO surface, similarly to precedent literature. [110] The GR nanoflakes covered the FTO surface (**Fig. 55a)**, while the average flake size was 1090 ± 50 nm. The morphology of the Fe_2O_3/GR nanocomposites strongly depended on the composition. At high Fe_2O_3 loading (450 mC cm^{-2}), for example, the GR nanoflakes were mostly and homogeneously covered by Fe_2O_3 (**Fig. 55b** and **c**). For layers, containing less Fe_2O_3 (Q_{ED} = 70 mC cm^{-2}), islands were formed, leaving the surface of the nanoflakes partially exposed. If the amount of Fe_2O_3 was more than 450 mC cm^{-2}, all gaps among the nanoflakes were filled with Fe_2O_3, showing a similar morphology as in the case of the pristine Fe_2O_3 photoelectrode (**Fig. 54**). To estimate the average layer thickness (Q_{ED} = 450 mC cm^{-2}) of both systems, cross-section SEM images were recorded (**Fig. 56a** and **b)**, which revealed layer thicknesses of 220 ± 40 nm and 440 ± 90 nm for the Fe_2O_3 and Fe_2O_3/GR films, respectively.

TEM images further confirmed the composite formation, as both the Fe_2O_3 nanocrystals and the underlying GR nanoflakes are visible (**Fig. 55d-f**). HR-TEM revealed lattice fringes in the case of the Fe_2O_3 nanoparticles, suggesting high crystallinity all the way to the edges of the particles. Interplanar spacings of 0.370 nm and 0.260 nm were determined, corresponding to the [012] and [110] lattice planes of α-Fe_2O_3, respectively.[110]

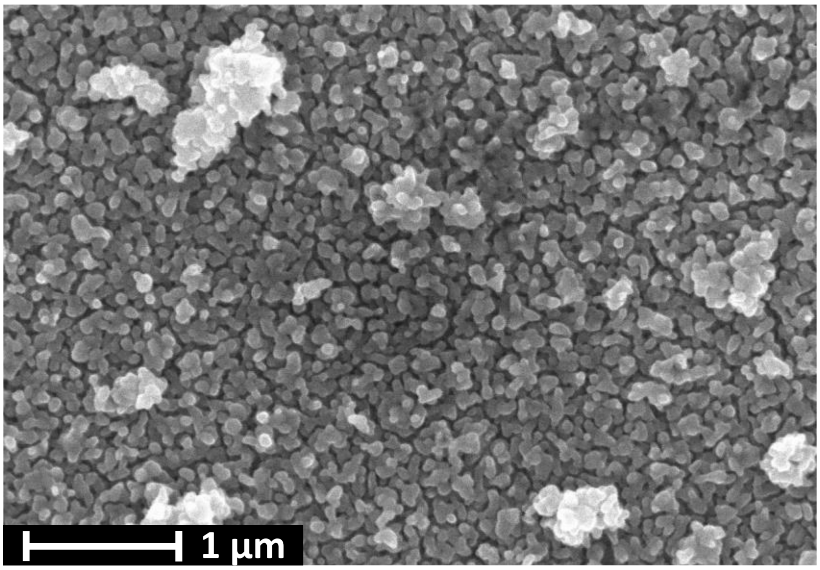

Fig. 54: SEM images captured for a deposited nanostructured Ti-doped Fe_2O_3 electrode on FTO (Q_{ED} = 450 mC cm^{-2})

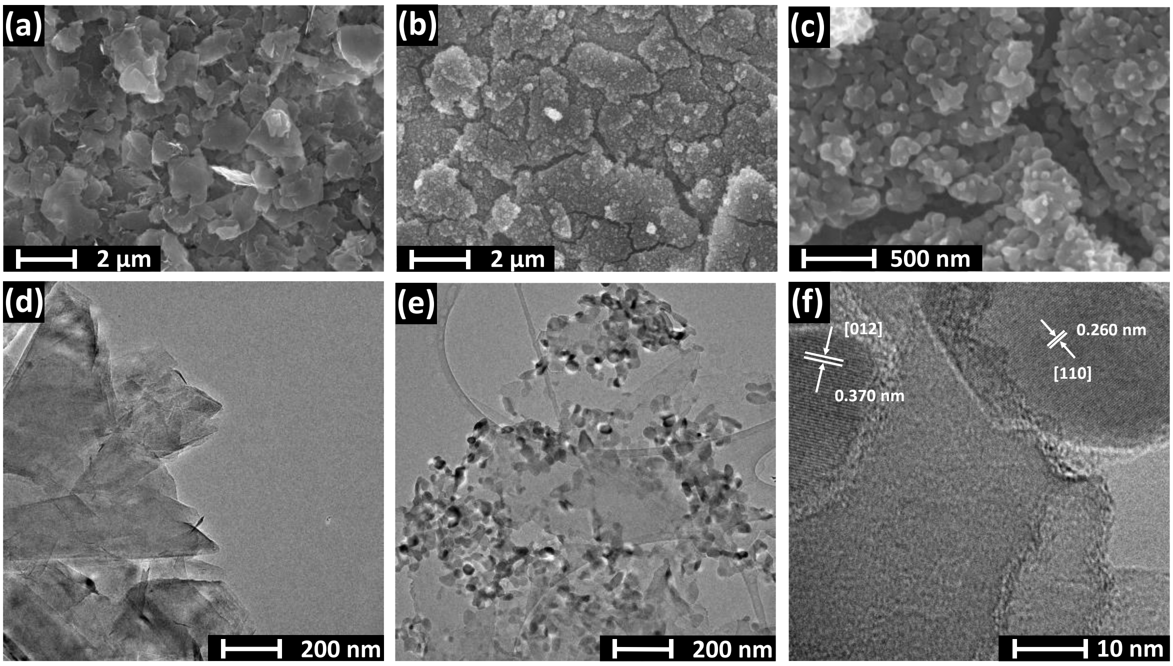

Fig. 55: SEM images captured for GR-coated FTO (a), Fe_2O_3/GR nanocomposite photoelectrode (Q_{ED} = 450 mC cm^{-2}) (b) and for the same sample as (b) at higher magnification (c). TEM images taken for GR nanoflakes (d), Fe_2O_3/GR nanocomposite (Q_{ED} = 450 mC cm^{-2}) (e) and for the same sample as (e) at higher magnification (f).

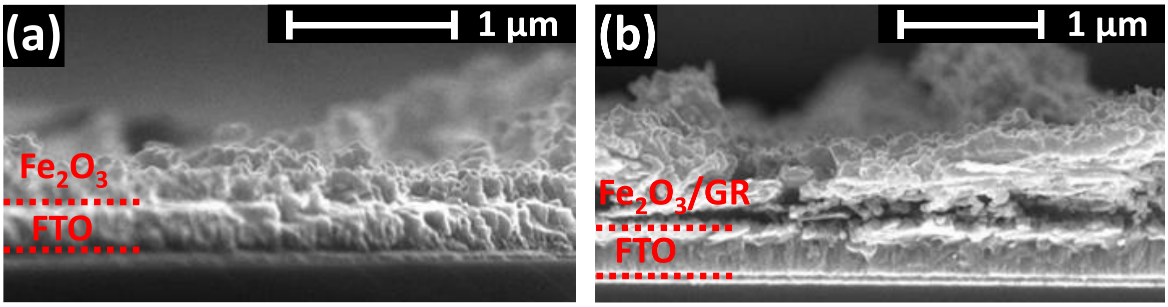

Fig. 56: Cross-section SEM images captured for nanostructured, Ti-doped Fe_2O_3 (Q_{ED} = 450 mC cm^{-2}) (a) and nanostructured, Ti-doped Fe_2O_3/GR photoelectrode (Q_{ED} = 450 mC cm^{-2}) (b).

Fig. 57a compares the Raman spectra recorded for the Fe_2O_3/GR nanocomposite sample and its pristine components. All Raman-active bands are present on the spectrum of GR (**Fig. 57a**, blue curve).[180] The small D/G ratio (0.158) and the position of the 2D band (2688 cm^{-1}) implies that few-layer GR flakes are present in our samples. In the case of the Fe_2O_3 film (**Fig. 57a**, red curve) five out of the seven characteristic bands can be identified, further confirming the chemical nature of the deposited material. Bands centered at 220 cm^{-1} and 504 cm^{-1} are corresponding to the A_{1g} modes, while the ones, which appeared at 288, 401 and 613 cm^{-1} are originated from the E_g modes of α-Fe_2O_3. [181] As for the Fe_2O_3/GR nanocomposite electrode, all bands assigned both to GR and Fe_2O_3 are present on the spectrum (**Fig. 57a**, red curve). Moreover, the presence of the D+D", 2D, D+D’ and 2D’ bands in the nanocomposite is a direct proof that GR did not get oxidized during the synthetic procedure. [182] Finally, Raman bands of Fe_2O_3 are slightly (an average of 5 cm^{-1}) blue-shifted in the nanocomposite, implying an interaction between GR and Fe_2O_3.

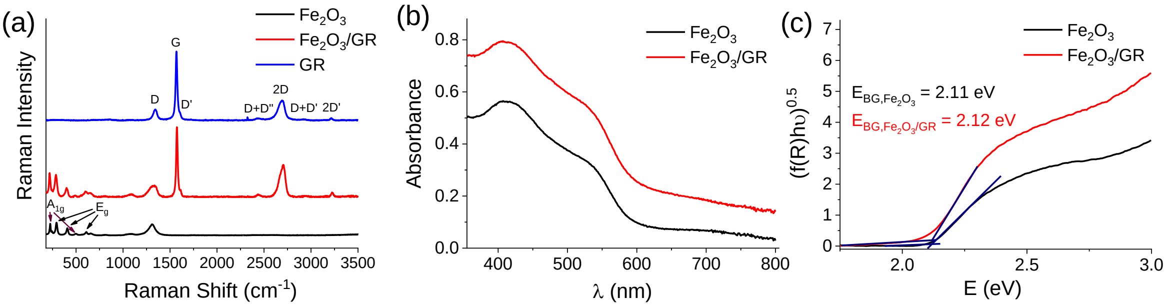

Fig. 57: Raman spectra recorded for Fe_2O_3, GR and Fe_2O_3/GR thin films (a). Q_{ED} was 450 mC cm^{-2} in both cases. UV-vis spectra recorded for Fe_2O_3 and Fe_2O_3/GR thin films (b). Similar compositions were used as for the Raman measurements (a). Tauc plots constructed from diffuse reflectance spectra recorded for Fe_2O_3 and Fe_2O_3/GR thin films (c).

Optical properties of Fe_2O_3 and Fe_2O_3/GR films were studied by UV-vis spectroscopy (**Fig. 57b**). Three absorption features can be observed on the spectrum of bare Fe_2O_3, originating from the ligand d–d and from the direct O2p → Fe4s transitions. [183] As for Fe_2O_3/GR, the only difference is a non-characteristic absorption, shifting the baseline throughout the whole spectral range. [184] Tauc analysis was performed (**Fig. 57c**), [185,186] and indirect bandgaps of 2.11 eV and 2.12 eV were calculated, in good agreement with literature values. [114]

5.3.2 PEC properties of Fe_2O_3/graphene nanocomposite photoelectrodes

To estimate PEC water oxidation performance, linear sweep photovoltammetry traces were recorded in 1 M NaOH solution (**Fig. 58a**). Three major conclusions can be promptly made by looking at these photovoltammograms: 1.) significantly higher photocurrents were harvested in the case of the GR-containing layer, 2.) dark currents start to develop earlier, and 3.) the onset potential slightly shifted (≈ 200 mV) towards more positive potentials in the case of the nanocomposite sample. This last phenomenon can be explained by the difference between the interfaces with the underlying FTO electrode surface. While the Fe_2O_3/FTO is a SC/SC junction, the Fe_2O_3/GR contains a SC/metallic interface. In addition, the temperature of the second heat treatment step (700 °C) is high enough for Sn to diffuse into the Fe_2O_3 structure, thus additionally doping it (see XPS results in **Fig. 53**). According to the literature, this slightly shifts onset potentials as well as increases the photocurrent.[118,179] The presence of GR nanoflakes in the electrode architecture can inhibit this type of diffusion process.

The PEC behavior of nanohybrid electrodes of six different compositions was studied (**Fig. 59**). A maximum of 1.2 mA cm^{-2} photocurrent was measured for Fe_2O_3 layers (**Fig. 58b**), which value is in the range of the best-performing Fe_2O_3 photoelectrodes prepared by electrodeposition. [110,115,187] Most importantly, all Fe_2O_3/GR nanocomposite photoelectrodes greatly outperformed their pristine Fe_2O_3 counterparts. A maximum trend can be observed as a function of Fe_2O_3 loading, both for the pristine and the GR-containing system. Two times higher photocurrents were measured compared to the bare Fe_2O_3 (2.5 mA cm^{-2} vs. 1.2 mA cm^{-2}) for nanocomposite layers with the optimal composition (Q_{ED} = 450 mC cm^{-2}). To the best of our knowledge, until the writing of this dissertation, no *electrodeposited* Fe_2O_3-based photoelectrode showed such PEC behavior so far (see **Table 5** in literature for comparison).

Fig. 58c shows the photoaction spectra recorded for the best performing Fe_2O_3 and Fe_2O_3/GR photoelectrodes. The characteristics of the two curves were similar, with higher IPCE values in the case of the nanocomposite electrode. The IPCE values were comparable to the ones, obtained for Ti-doped hematite layers by others, [188] but a higher bias was applied in this study (+1.5 V vs. RHE). The cutoff region of the two curves were similar ($E_{cutoff} \approx E_{BG} \approx 2$ eV), indicating that the wavelength range of photoactivity has not broadened in the case of the Fe_2O_3/GR photoelectrodes. This means that the origin of the enhanced PEC behavior was rooted in the enhanced charge carrier separation and transport, similar to the previously described Cu_2O/nanocarbon photoelectrodes (i.e., the enhanced non-characteristic absorption in **Fig. 57b** does not results in any photocurrent).

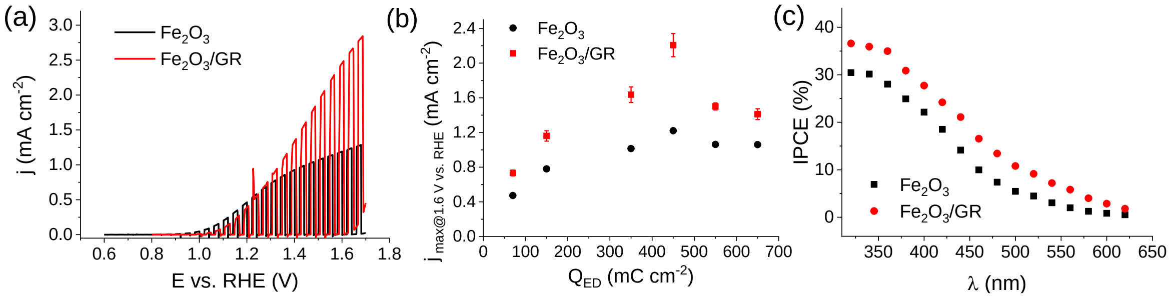

Fig. 58: Linear sweep photovoltammograms, recorded for Fe_2O_3 and Fe_2O_3/GR films in 1 M NaOH under 100 W cm^{-2} simulated AM 1.5 solar light (a) (Q_{ED} = 450 mC cm^{-2}, the sweep rate was kept at 2 mV s^{-1}, and the light-chopping frequency was 0.1 Hz). Maximum photocurrents read from the set of photovoltammograms presented in **Fig. 59** (b). Error bars were calculated from at least three individual measurements on different electrodes. IPCE curves recorded for Fe_2O_3 and Fe_2O_3/GR photoelectrodes in 1 M NaOH solution, applying +1.5 V vs. RHE bias potential (c) (Q_{ED} = 450 mC cm^{-2}).

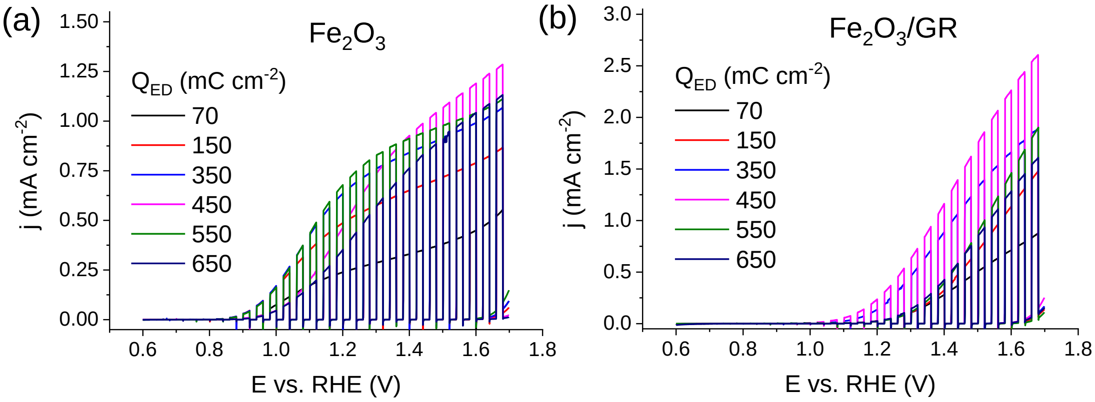

Fig. 59: Linear sweep photovoltammetry traces recorded for nanostructured Fe_2O_3 (a), and Fe_2O_3/GR thin films (b) synthesized with various Fe_2O_3 loadings, measured in 1 M NaOH under 100 W cm^{-2} simulated AM 1.5 solar light, the sweep rate was kept at 2 mV s^{-1}, and the light-chopping frequency was 0.1 Hz.

To glean insights on the electrical properties of the nanohybrid electrodes, EIS measurements were performed. **Fig. 60** shows the Nyquist plots constructed from data collected at open circuit conditions for both Fe_2O_3 and Fe_2O_3/GR. In the case of Fe_2O_3, a distinct semicircle can be identified in the high-frequency range, assigned to an electron-transfer limited process, whereas the linear part, observed in the lower-frequency range corresponds to the diffusion-limited electron-transfer process.[189] The semicircle portion has visibly shrunk in the case of the nanocomposite layers. By fitting the semicircle portion, information can be gained on the series resistance (R_s) and on the charge transfer resistance (R_{ct}). R_s is similar for the two systems. As for R_{ct}, one order of magnitude smaller value was calculated for the nanohybrid sample. This phenomenon has been already discussed and elucidated in this dissertation and in the literature for other metal-oxide/nanocarbon systems [87]: by electrodepositing a metal-oxide on a conductive nanocarbon network, the electric conductivity of the nanocomposite layers becomes better, compared to the pristine metal-oxides. This results in improved charge carrier transport and thereby also in suppressed charge carrier recombination are explaining the higher photocurrents in the case of the Fe_2O_3/GR layers.

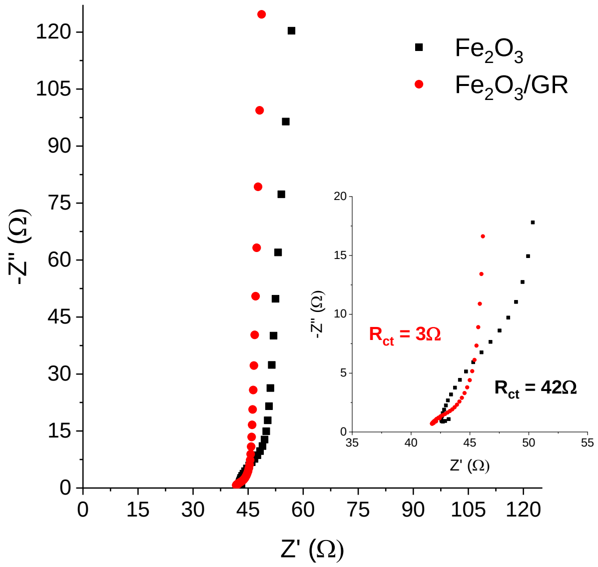

Fig. 60: Nyquist plots recorded for Fe_2O_3 (black curve) and Fe_2O_3/GR (red curve) at OCP in 1 M NaOH (Q_{ED} = 450 mC cm^{-2}). The inset shows the magnified high-frequency region of the plot.

5.3.3 Photostability of Fe_2O_3/graphene nanocomposite photoelectrodes

To probe the photostability of the photoelectrodes, chronoamperometry measurements were carried out for two hours under continuous simulated solar illumination (**Fig. 62a)**. While Fe_2O_3 remained stable in the timeframe of the experiment, the photocurrents recorded for Fe_2O_3/GR decreased substantially within 40 min, approaching the values recorded for Fe_2O_3. It is clear from this comparison that this decrease must be tied to the degradation of the underlying GR scaffold upon applying positive bias and illumination. To probe the disappearance of GR from the hybrid electrode, Raman spectra were recorded periodically during the long-term photoelectrolysis experiment (**Fig. 61a** and **Fig. 62b**). The spectra were recorded every 10 minutes in the first hour and every 20 minutes in the second hour. The presence of GR was followed by monitoring the intensity of the G band on the spectra. To better see the changes in the amount of GR, Raman spectra were recorded from the back side of the electrode. Clearly, this band vanished within the first hour (**Fig. 61a**). To quantify this observation, G band area was integrated for all spectra and it was normalized with the value calculated for t = 0 min (**Fig. 62b**). The normalized area of the G band decreased monotonously, and completely vanished after 80 minutes, confirming the disappearance of the underlying GR layer.

Our observation invokes a rather uncomfortable question about the applicability of nanocarbon-containing electrodes in oxidative processes, since the widely accepted consensus is that such corrosion should not occur. There are few among the many reports on SC/nanocarbon nanocomposites, however, which described a similar effect. [190,191] Upon illumination, either the formed reactive species ($OH^{\cdot}$ radicals) oxidize GR, or after charge separation, a fraction of the photogenerated holes are not transported toward the electrode/electrolyte interface, but rather to GR, which subsequently gets directly oxidized.

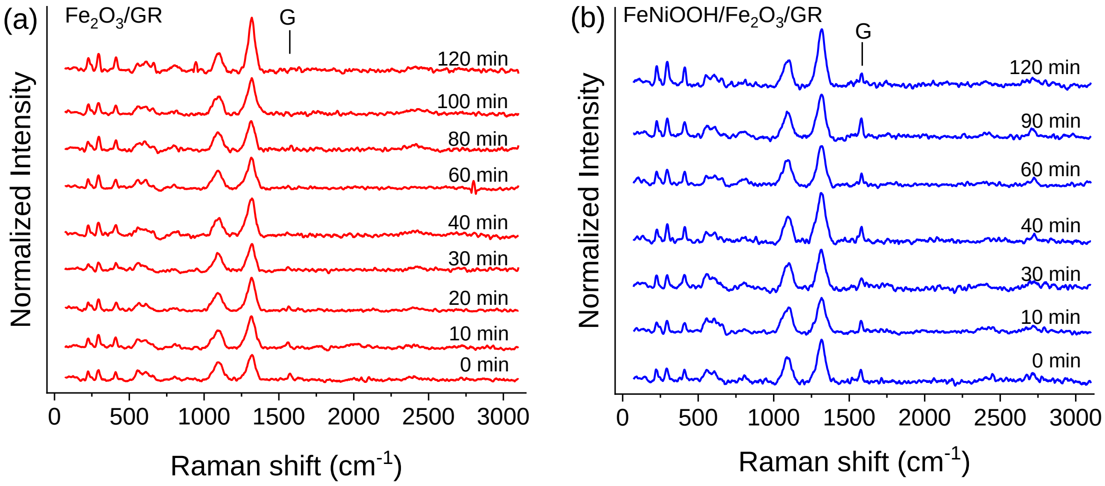

Fig. 61: Raman spectra recorded for a Fe_2O_3/GR (a) and FeNiOOH/Fe_2O_3/GR photoelectrode (b) during a long-term photoelectrolysis measurement performed applying E = +1.45 V vs. RHE (Q_{ED} = 450 mC cm^{-2}).

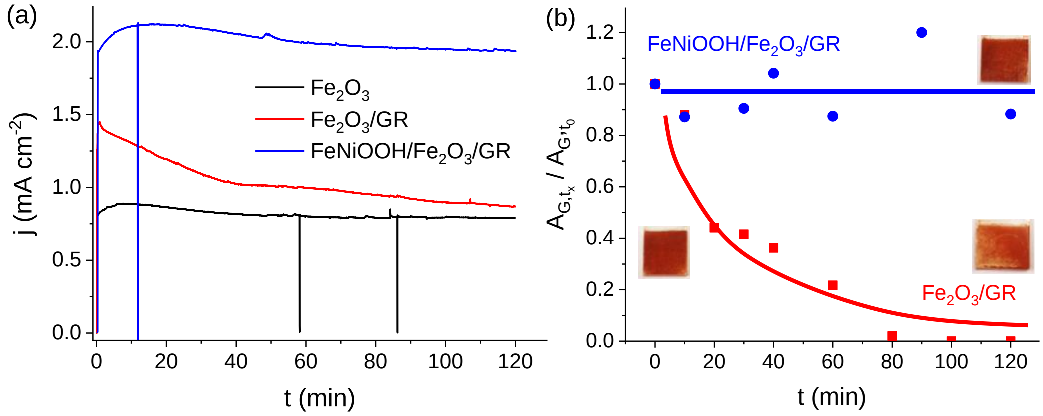

Fig. 62: Long-term chronoamperometry measurements performed in 1 M NaOH solution saturated with Ar, applying E = +1.45 V vs. RHE potential and under 100 mW cm^{-2} AM 1.5 simulated sunlight (a). The vertical lines in show the current drop upon interrupting the illumination. Change in the normalized area of the G band of GR in time (b). Values were determined by integrating the G band intensity in the Raman spectra presented in **Fig. 61** and normalizing these values with area of the G band at t = 0 min. Two lines were added to guide the eye of the reader.

5.3.4 Synthesis and PEC behavior of FeNiOOH/Fe_2O_3/graphene photoelectrodes

One viable option to tackle photostability issues is to deposit a co-catalyst layer on top of Fe_2O_3. By doing so, in theory, the vast majority of the photogenerated holes are rapidly transferred to the co-catalyst, which might successfully prevent the corrosion of GR. We chose amorphous mixed FeOOH and NiOOH as co-catalyst (abbreviated as FeNiOOH in the following), which was electrodeposited on Fe_2O_3/GR after the second heat treatment step (see the Experimental Section for further details). Both FeOOH and NiOOH are well-known water oxidation catalysts and have been widely applied as co-catalyst overlayers to boost the PEC performance of various metal oxide photoelectrodes.[124,125,192,193] In most of these studies, however, either only one of them was used [125] or they were deposited on top of each other as separate layers.[193] In our case, mixed FeOOH and NiOOH were synthesized in a *single step* by electrodeposition (instead of the more popular photodeposition). The main advantage of this method is that FeOOH and NiOOH are simultaneously deposited on the electrode surface and their ratio can be easily tuned by the variation of the concentration of the Fe, and Ni salts in the electrodeposition solution.[124,148] To determine the exact composition of the FeNiOOH layer, XPS measurements were performed. Survey scans proved the presence of O, Fe and Ni in the sample (**Fig. 63a**). After collecting and evaluating the high resolution scans (**Fig. 63b,c,d**), the following elemental composition was determined: 83 at%, 16 at% and 1 at% O, Fe and Ni, respectively.

The most important conclusion from these numbers is that the Fe:Ni ratio differs from the one expected from the experimental conditions (Fe:Ni 5:3), and thus the formed coating is not stoichiometric. Additionally, the position and intensity of the O 1s peaks suggest that O atoms in the sample are mostly in the form of hydroxide (71.0 %), which is a bit more than two-times higher than in the case of the pristine Fe_2O_3 sample. Based on this data it can be safely concluded that the electrodeposited FeNiOOH overlayer consists of mixed FeOOH and NiOOH.

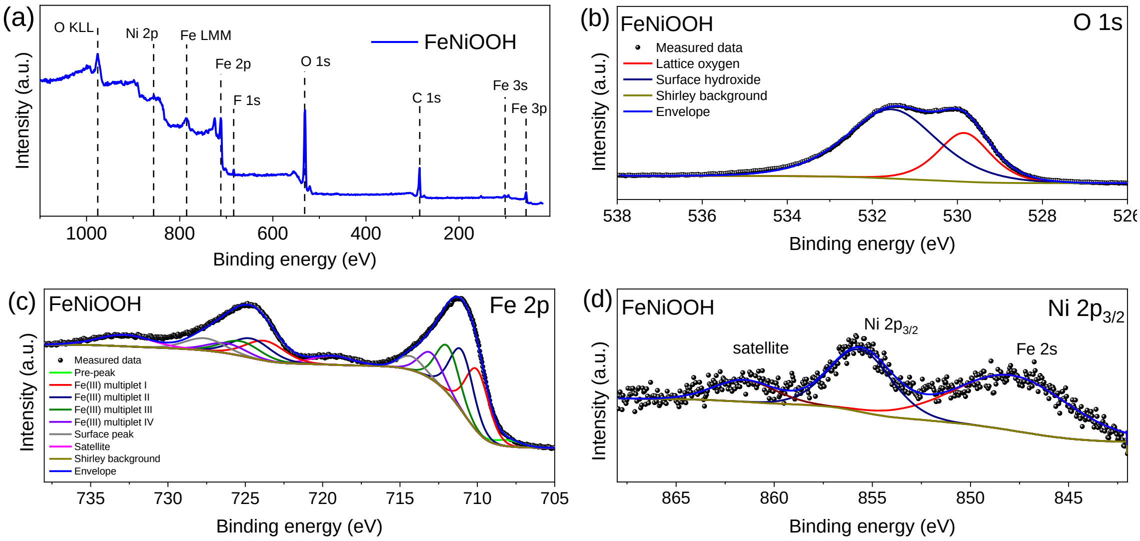

Fig. 63: Survey XPS scan (a) and high resolution XPS data (b,c,d) recorded for the deposited FeNiOOH overlayer.

Fig. 64a shows linear sweep photovoltammetry traces, recorded for Fe_2O_3/GR and its FeNiOOH-decorated counterpart. The onset potential has notably shifted to the cathodic direction (approximately 160 mV) in parallel with the 40% increase of the maximum photocurrent, reaching photocurrents as high as 3.1 mA cm^{-2}. The effect of the co-catalyst on the photostability of the Fe_2O_3/GR electrode was even more striking (blue curve in **Fig. 62a**). The photocurrents remained stable during the two-hour photoelectrolysis in contrast to the previously experienced rapid decrease.

Raman spectra were also taken during this measurement (**Fig. 61b**). The G band corresponding to the presence of GR is clearly visible even at the end of the two-hour electrolysis. Data were quantified similarly as in the case of the Fe_2O_3/GR electrode (**Fig. 62b**) revealing that the normalized area of the G band (thus the amount of GR in the sample) did not change significantly during the measurement. According to the PEC and Raman data, we conclude that by depositing FeNiOOH co-catalyst layer on the surface of Fe_2O_3/GR photoelectrode, the effect of the GR framework on the PEC properties was preserved (even slightly improved), in parallel with the protection of the underlying GR from corrosion.

To further verify that the measured photocurrents are a result of PEC water oxidation, the concentration of the evolved oxygen was measured with a Clark-type O_2 sensor (**Fig. 64b**). A FE of O_2 evolution (right axis) was close to 100% and calculated over the course of the three hour measurement employing a FeNiOOH/Fe_2O_3/GR photoelectrode.

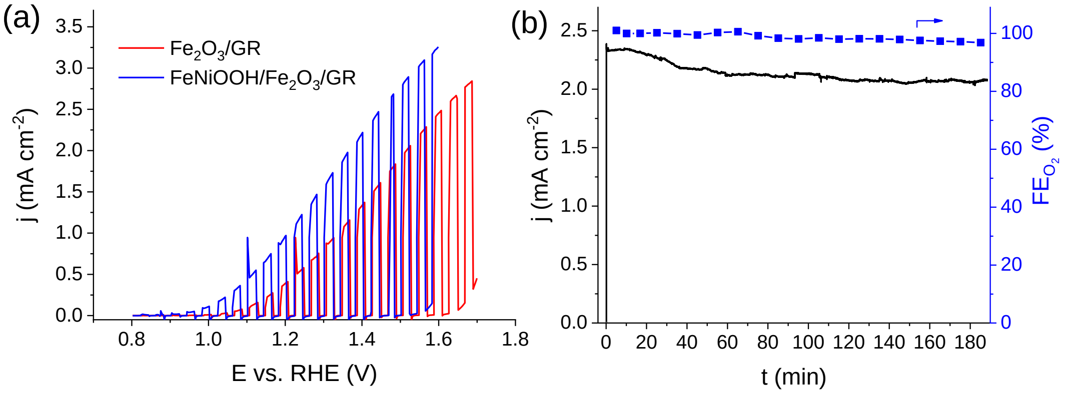

Fig. 64: Linear sweep photovoltammograms, recorded for Fe_2O_3/GR and FeNiOOH/Fe_2O_3/GR thin films in 1 M NaOH under 100 W cm^{-2} simulated AM 1.5 sunlight (a). (Q_{ED} = 450 mC cm^{-2}, the sweep rate was kept at 2 mV s^{-1}, and the light-chopping frequency was 0.1 Hz). Long-term photoelectrolysis measurement performed on a FeNiOOH/Fe_2O_3/GR sample (Q_{ED} = 450 mC cm^{-2}) in 1 M NaOH, saturated with Ar prior to the measurement (b). The applied potential was +1.45 V vs. RHE, while the light intensity was maintained 100 mW cm^{-2}.

5.3.5 Mechanistic insights of the PEC properties of FeNiOOH/Fe_2O_3/graphene photoelectrodes

Our hypothesis on the processes occurring in the investigated systems are presented in **Fig. 65**. For the pristine Fe_2O_3, photogenerated holes can oxidize water either directly from the VB, or from the surface states, where they can also recombine with electrons from the conduction band (CB) (**Fig. 65a**). When GR nanoflakes are present (**Fig. 65b**), two additional processes occur: better transport of photogenerated electrons towards the back contact, due to the highly conductive nature of GR and some of the photogenerated holes can also be transported to GR and oxidize it (note the metallic nature of GR). Finally, if the surface of Fe_2O_3 is decorated with a material, which passivates the surface states, holes can be rapidly transported to the co-catalyst and to the substrate (**Fig. 65c**). Most importantly, because of the rapid hole-transfer to FeNiOOH and rapid electron-transfer to GR, the pathway leading to the corrosion of GR is successfully eliminated while increased photocurrent activity was also achieved.

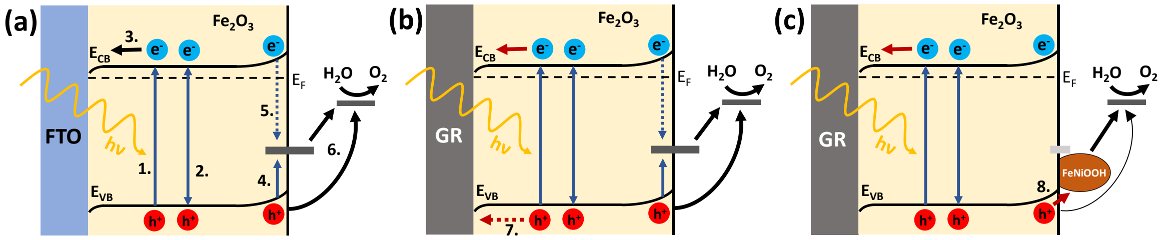

Fig. 65: Simplified models of the elementary processes occurring in the case of a Fe_2O_3 (a), Fe_2O_3/GR (b), and FeNiOOH/ Fe_2O_3/GR photoelectrode (c). Elementary processes are: 1.) absorption of a photon and generation of an electron-hole pair, 2.) nonradiative recombination of an electron-hole pair, 3.) electron transport towards the back contact, 4.) trapping of holes in surface states, 5.) electron-hole recombination in surface states, 6.) hole-transfer from the VB and from the surface states to the electrolyte, 7.) hole-transport towards the GR framework (which can produce reactive species ($OH^{\cdot}$ radicals) to oxidize GR) and 8.) hole-transport to the FeNiOOH co-catalyst overlayer.

5.4 Photoelectroreduction of nitrate ions on CuI-PbI_2 nanocomposite electrodes

5.4.1 Morphological and optical study of CuI-PbI_2 nanocomposite electrodes

The last chapter of this dissertation deals with mixed metal-iodide based composite electrodes. We first studied the phase diagram of the CuI-PbI_2 system.[140] **Fig. 66** shows the phase diagram, together with the optical images of samples of different compositions (the melted mixture is also shown). There is no discernible intermediate compound in the system, only a mixture of solid γ-CuI and PbI_2. Furthermore, at 50 n/n% PbI_2 content the system has an eutectic point where the melting starts already around 300 °C (as opposed to 606 °C to 404 °C of pure materials).

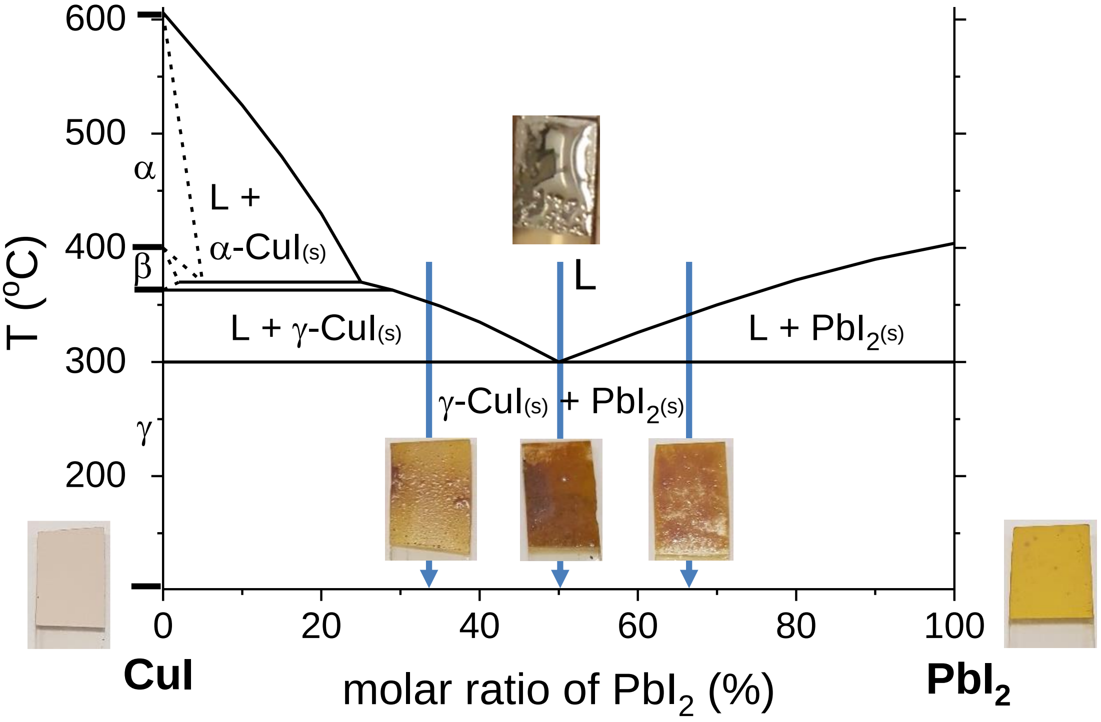

Fig. 66: Phase diagram of the CuI – PbI_2 system adopted from [140] with presentation of three different pathway from the melted thin film to the solid, highly crystalline film (a). The dark gray molten metal-like liquid illustrates the melted nanocomposite. L stands for liquid.

Based on the phase diagram, we performed preliminary experiments to determine an optimal temperature, melting time (**Fig. 67a**), and the spray-coated loading mass (**Fig. 67b**) for the thin film melting method, what we used for the preparation of CuI-PbI_2 photoelectrodes. The monitored parameter was the maximum photocurrent density of the photocathode, recorded in Ar saturated 0.1 M $NaNO_3$ solution under 5 sun irradiation (the CuI-PbI_2 ratio was kept fixed at 50-50%). Better performing photoelectrode was observed when the thin film melting method was carried out at 400 °C for only 5 minutes under Ar gas (at this temperature sublimation of PbI_2 becomes significant over time). The optimum loading (with the previously determined heat treatment parameters) was obtained to be 7 mg cm^{-2}, which corresponds to around 6 µm thickness of nanocomposite film (based on the cross section SEM images in **Fig. 70b**). This loading amount per sample was kept constant throughout this work.

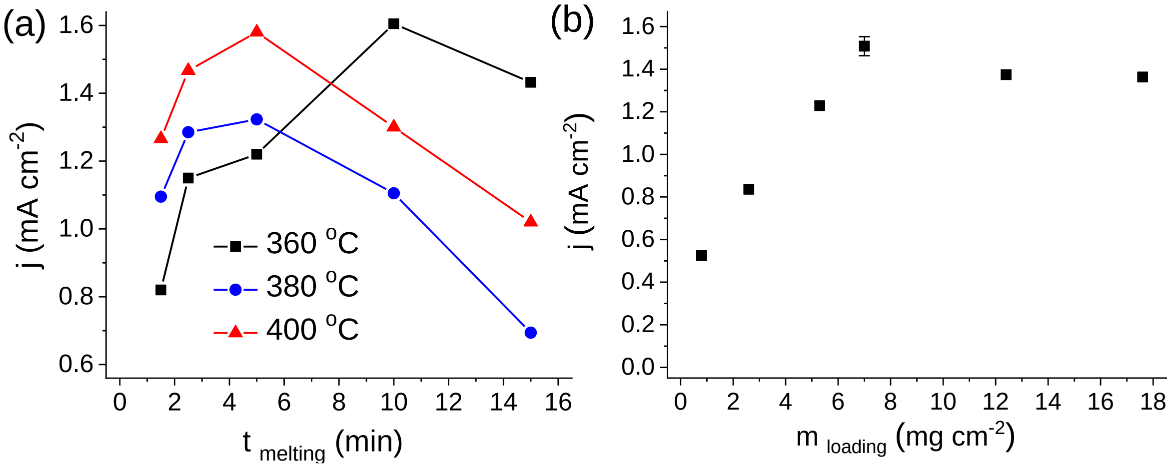

Fig. 67: Preliminary experiments to have optimal heat treatment parameters (melting time and temperature) (a) and dependence of mass loading (b) on the photocurrent recorded for CuI-PbI$_2$ (50-50 %) photoelectrodes, in Ar saturated 0.1 M NaNO$_3$ solution under 5 sun radiation.

XRD data furnished evidence on the formation of a highly crystalline mixture. **Fig. 68a** shows diffraction patterns of CuI, PbI$_2$ and CuI-PbI$_2$ (50-50 %) after melting. Diffraction patterns of CuI and PbI$_2$ are well-aligned with their corresponding JCPDS data. The unassigned peaks were related to the aluminum sample holder (37.4°, 43.6°, and 64°) and to the FTO substrate (peak at 52.5°). The XRD pattern of mixture of CuI-PbI$_2$ (50-50 %) sample before melting (**Fig. 68b**) showed all the major peaks of these two parent compounds, but after melting, the diffractions related to plane (111) of CuI and planes (001), (003) and (004) of PbI$_2$ become dominant (**Fig. 68a**).[194,195] These peaks appeared in the XRD pattern of all nanocomposite samples (containing different molar ratio of CuI and PbI$_2$, **Fig. 68c**). This trend suggests that large, uniform crystal domains are present in the samples. Notably, no new diffraction peak developed, which would correspond to a new phase, as suggested by precedent literature.[137,138]

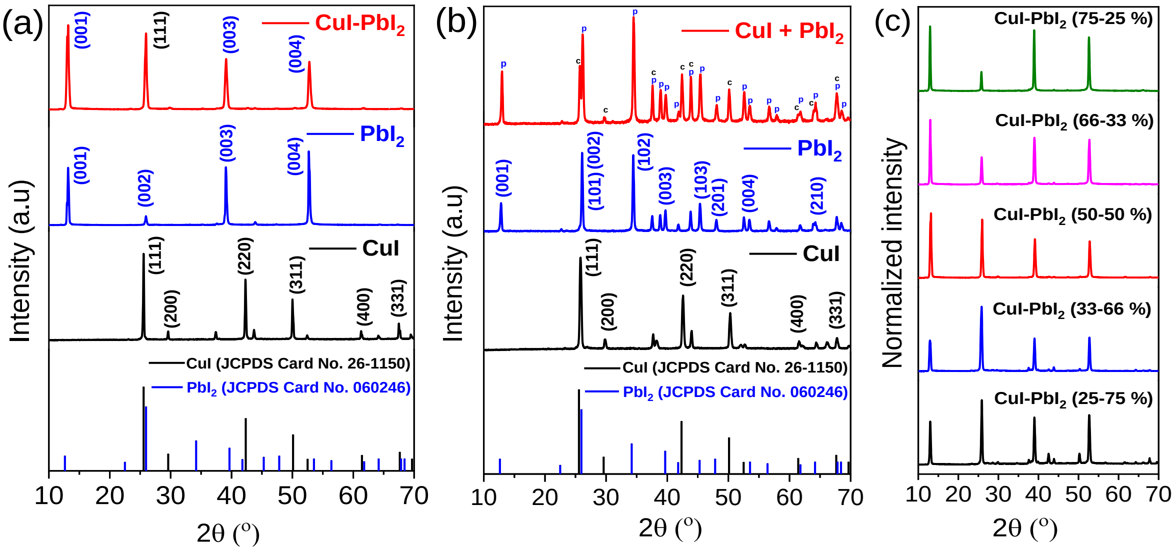

Fig. 68: XRD pattern of CuI, PbI_2, CuI-PbI_2 (50-50 %) after heat treatment (a), before heat treatment (b), and samples containing different molar ratio of CuI and PbI_2 after melting (c).

Electron microscopy images were taken for the CuI, PbI_2 and CuI-PbI_2 (50-50 %) samples before and after heat treatment, to probe their morphological attributes. Both CuI and PbI_2 appeared as few micron size particles before heat treatment on the SEM images (**Fig. 69a** and **b)**. No obvious change was seen in the morphology of CuI upon the heat treatment (**Fig. 69b)** since the melting of pure γ-CuI occurs around 606 °C. In the case of pristine PbI_2 however, after the heat treatment the particles melted, and a sheet like appearance was observed (**Fig. 69c** and **d)**.

In the CuI-PbI_2 (50:50 %) mixture, micron-sized particles are visible initially (**Fig. 70a**). Upon heat treatment, however, major changes were spotted. Cross sectional images demonstrated that a few micrometers thick, semi-continuous film was formed upon the melting process (**Fig. 70b**). In the composite, the melting point of the components was reduced (see also the phase diagram in **Fig. 66**), thus both components are melted at 400 °C. In the sheet like structure, CuI nanoparticles are well dispersed on the largely ordered PbI_2 matrix, as exemplified in **Fig. 70b**. This ordered morphology is retained in the long range and provides fertile ground for facile charge carrier extraction as detailed later.

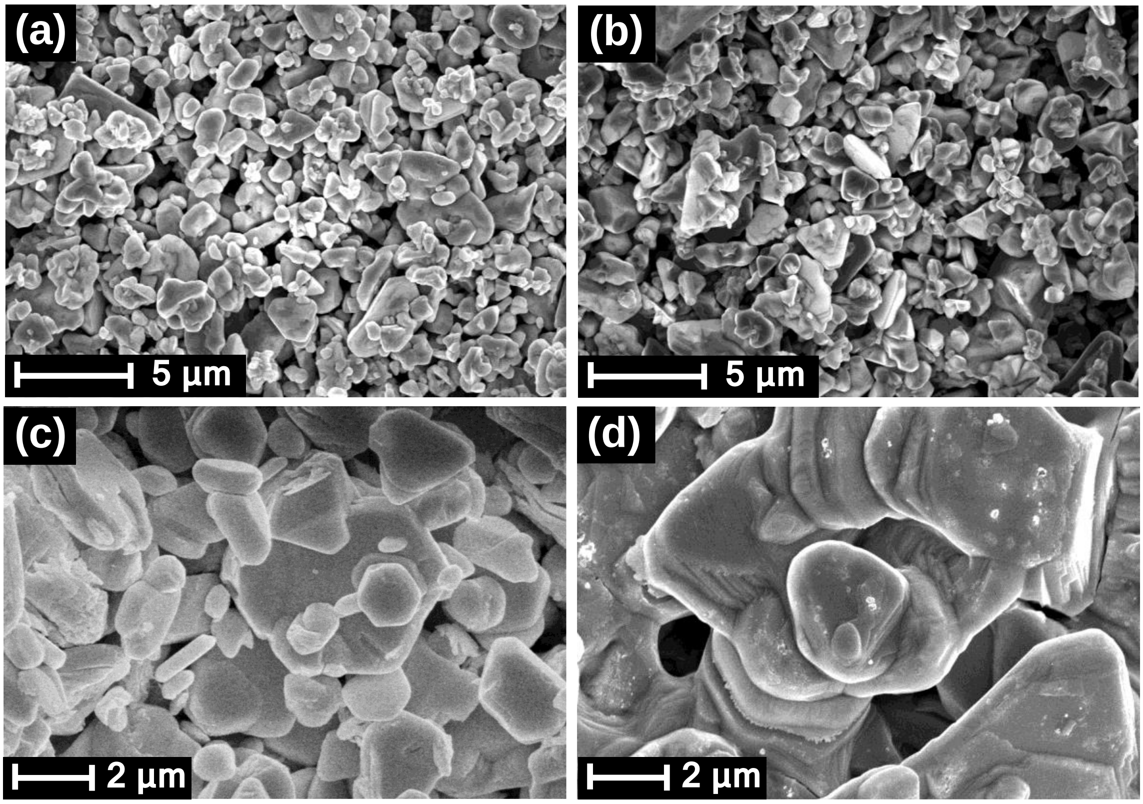

Fig. 69: Topographical SEM images of CuI (a,b), and PbI_2 (c,d) before (a,c) and after (b,d) the heat treatment. (Note that 400 °C is little below to the melting point of PbI_2 (404 °C, see in phase diagram), so exceptionally we used higher temperature (420 °C) during heat treatment in this case).

In order to better understand this structure, cross-sectional TEM lamellae were prepared from the melted CuI-PbI_2 (50-50%) photoelectrode with an SEM-FIB instrument (see details in experimental section). A TEM lamella is shown in **Fig. 70c**, where a Pt pad is seen on the top surface of the photoelectrode (for moving and fixing the lamellae) and the FTO layer, which is connected physically to the melted CuI-PbI_2 (50-50 %) layer. **Fig. 70d** shows a higher magnification image of the ion beam thinned part of the lamella, where it was transparent for electrons. From this area two apparently different points were selected for further imaging (**Fig. 70e and f**). High resolution TEM images confirmed that both components (CuI and PbI_2) exist in highly crystalline form (as expected from XRD analysis). Careful fast Fourier transform (FFT) analysis of HR-TEM images showed that PbI_2 forms the matrix upon heat treatment and CuI particles are distributed either on the surface of PbI_2 or they can be trapped among the PbI_2 sheets. Due to the size of the CuI particles (11 ± 6 nm), the resulting composite can be considered as a nanocomposite. It was be observed in **Fig. 70d-f** that within the homogeneous CuI-PbI_2 nanocomposite domains, there are CuI-free, highly crystalline pure PbI_2 parts. The formation of these inhomogeneities may be due to the thin film melting technique used during production: local inhomogeneity during cooling shifts the composition at a given point, causing the formation of non-nanocomposite crystals.

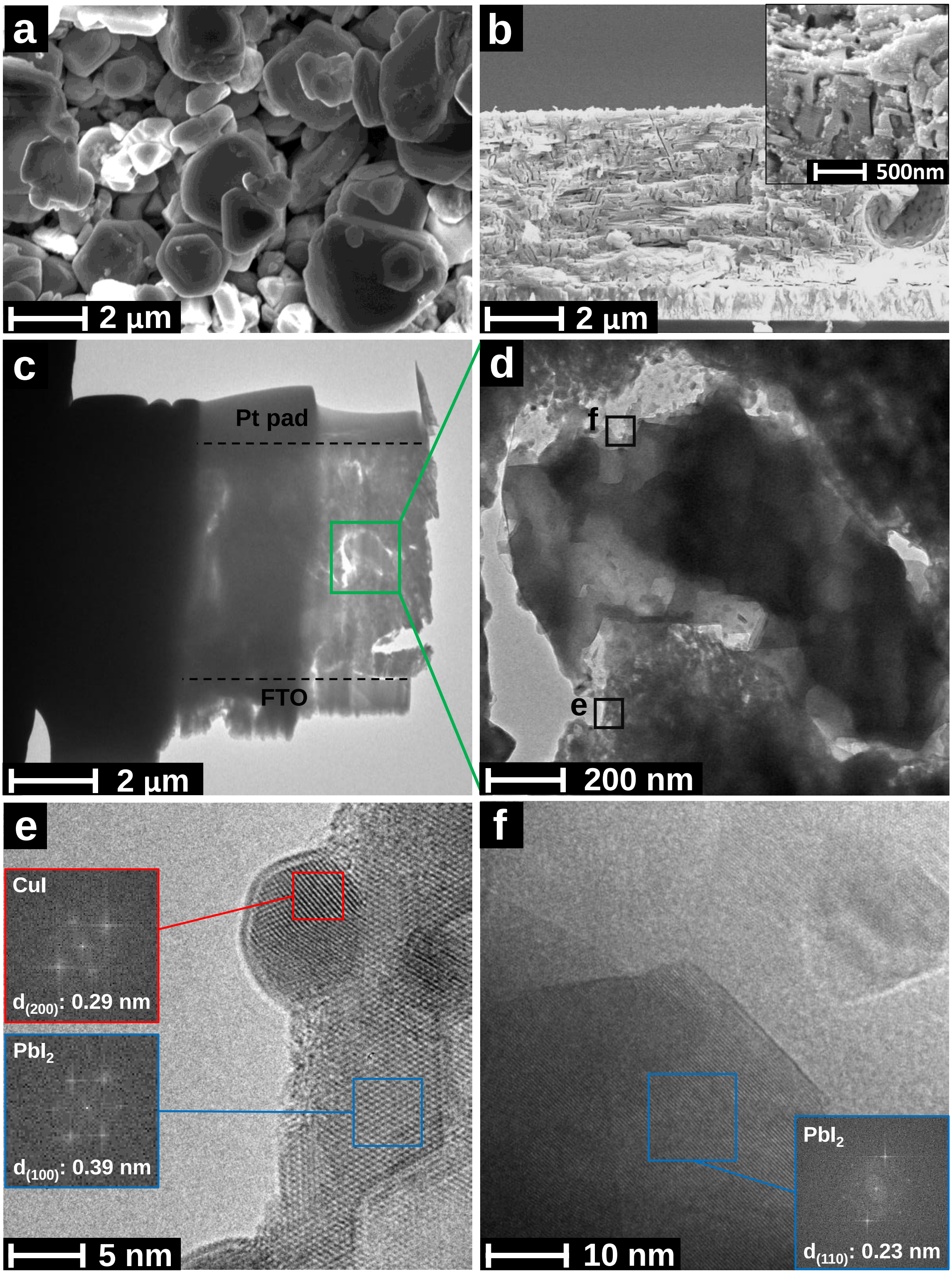

Fig. 70: SEM topographical images of CuI + PbI_2 mixture before heat treatment (a), and cross-sectional view of CuI-PbI_2 (50-50 %) after the thin film melting process (b). Prepared cross-sectional TEM lameallea from melted CuI-PbI_2 (50-50 %) at lower (c) and higher (d) magnification. High resolution TEM image from the selected areas in (d), with fast Fourier transformed (FFT) images from different area as insets (e, f).

Relying on these observations (described with the help of **Fig. 71**), the cooling "path" on the phase diagram during the electrode preparation influences the homogeneity of the resulting mixture in the following way:

- When the spray-coated mixture is heated, and the temperature reaches the liquid phase line, CuI and PbI_2 particles start to melt at the interfaces, which soon extends to the whole material, begins to form a molten salt. This system appears as a dark grey molten metal-like liquid.
- The sample with the composition of the eutectic point (50% PbI_2). When we start cooling the melted liquid from 400 °C: first during the cooling, when the eutectic point at 300 °C is reached, the melted salt "freezes", γ-CuI and PbI_2 crystallize at the same time from the liquid. Based on the TEM and SEM images (**Fig. 70**), we observed that the γ-CuI nanocrystals are located on the large hexagonal PbI_2 crystals, forming a nanocomposite. At the bottom of **Fig. 71**, this is represented by white circles (γ-CuI) on yellow hexagons (PbI_2).
- When starting from a composition other than the eutectic mixture, the liquidus is crossed elsewhere during cooling. For example, when the melt containing 33% PbI_2 is cooled, the liquidus is reached at about 350 °C. Then the excess γ-CuI begins to crystallize from the melted salt, while the concentration of PbI_2 in the liquid phase increases (since those crystals does not form) and the composition of the mixture shifts toward the eutectic composition. Because of this, under 300 °C, after solidification, the obtained large γ-CuI crystals are encased by the solidified eutectic γ-CuI – PbI_2 nanocomposite in the system. The average composition of the resulting material is the same as that of the initial composition, but a mixed, multiphase system is produced during the thin film melting process. The situation is analogous when the mixture is richer in PbI_2.

Based on the analysis of the phase diagram and the previous observations, the most homogeneous distribution of CuI-PbI_2 nanocomposite is expected at the eutectic point.

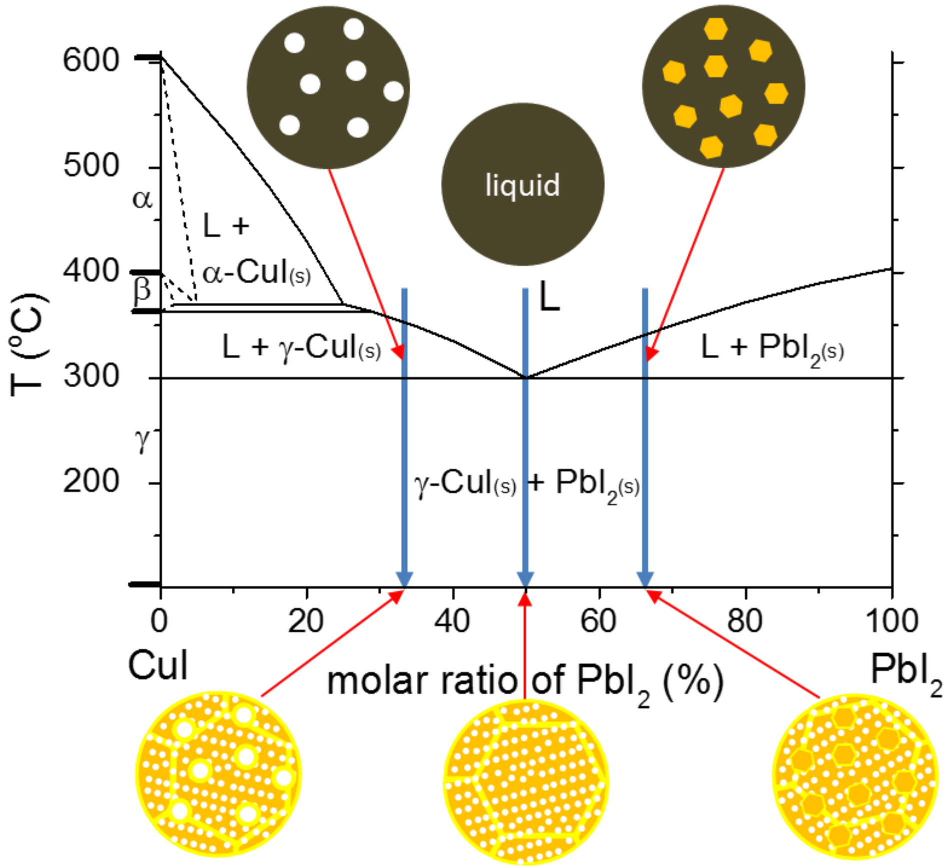

Fig. 71: Phase diagram of CuI – PbI_2 system with presentation of three different pathway from the melted thin film to the solid, highly crystalline film. The white circles and the yellow hexagons are representing γ-CuI nanocrystals and PbI_2 crystals.

At this juncture, we refer to related figures in the experimental section (**Fig. 11a** and **b**) and the mini-insert pictures of **Fig. 66**, where we show the color of the electrodes, which also changes upon melting (shifts to orange-reddish color). This predicts that the optical properties of the nanocomposites are different from those of their constituents. **Fig. 72a** shows the optical absorption features of CuI, PbI_2 and CuI-PbI_2 (50-50 %). While the spectrum of PbI_2 showed an absorption onset at 544 nm (translating to a 2.28 eV bandgap obtained by Tauc-analysis (see also **Fig. 73,** and the insert table of **Fig. 74**), CuI had a bandgap of 2.93 eV. These absorption bands appeared in the nanocomposite samples as well (**Fig. 74**). More interestingly, a new optical feature was observed between 550 and 680 nm for all nanocomposite samples (although at different extents), which translates to a new transition at 1.93-1.99 eV energy values (**Fig. 73b** and **Fig. 74**). This feature is indeed interesting, considering that no new compound was formed (based on our XRD and electron-diffraction studies).

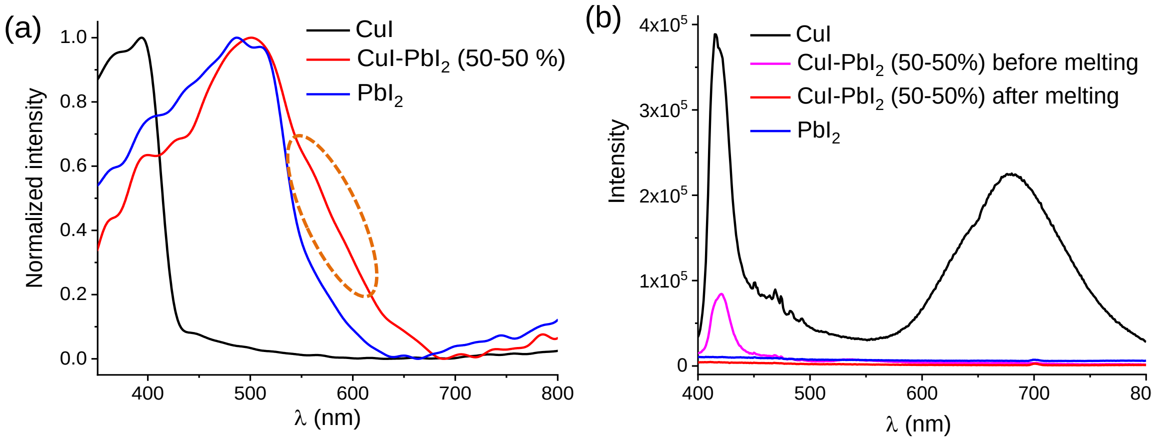

Fig. 72: UV-vis absorption profiles of CuI, PbI_2 and CuI-PbI_2 (50-50 %) thin films (a), photoluminescence of CuI, PbI_2 and CuI-PbI_2 (50-50 %) before and after the heat treatment (b).

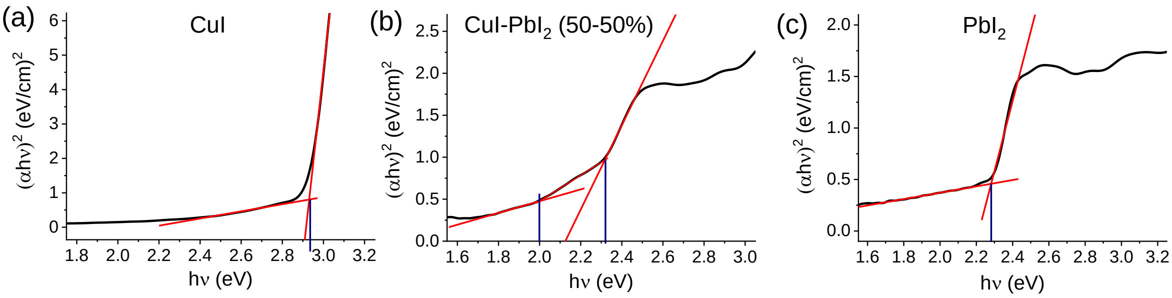

Fig. 73: Tauc plot of (a) CuI, (b) CuI-PbI_2 (50-50 %) and (c) PbI_2 from the UV-vis absorption profile.

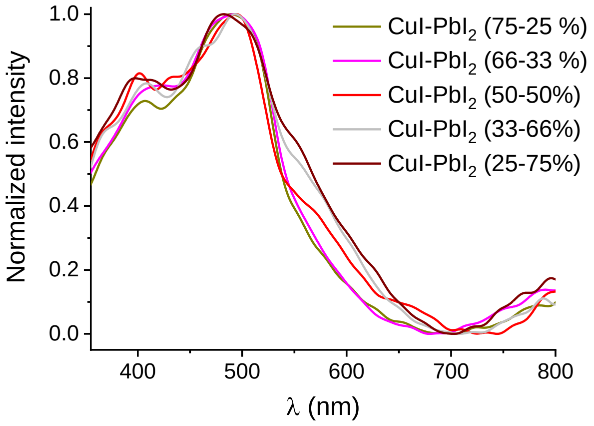

Sample (composition)	Direct bandgap (eV)	New transition (eV)
CuI	2.93	
CuI-PbI_2 (75-25 %)	2.28	1.94
CuI-PbI_2 (66-33 %)	2.29	1.98
CuI-PbI_2 (50-50 %)	2.32	1.99
CuI-PbI_2 (33-66 %)	2.30	1.95
CuI-PbI_2 (25-75 %)	2.32	1.93
PbI_2	2.28	

Fig. 74: Absorption profiles of investigated CuI-PbI_2 nanocomposites with different ratio. The insert table showing the optical bandgap obtained from Tauc plot for all the investigated samples.

To better understand the optical features of the nanocomposites, their light emission properties were studied by exciting the samples at 350 nm (an energy which is sufficient to excite both CuI and PbI_2). CuI showed two prominent luminescence peaks, a blue emission at 412 nm (ascribed to the radiative recombination of excitons) and red emission closer to 700 nm related to the presence of iodine vacancies (**Fig. 72b**).[196] The intensity of photoluminescence (PL) peaks of CuI is substantially reduced in the mixture even before heat treatment. After the heat treatment, however, the PL is *completely* suppressed. This suggests that the contact area between the two constituents increased upon the nanocomposite formation, and consequently enhancing the possibility of charge transfer between them. Among all nanocomposite samples, the film containing 1:1 molar ratio of CuI and PbI_2 shows the lowest PL intensity (**Fig. 75)**.

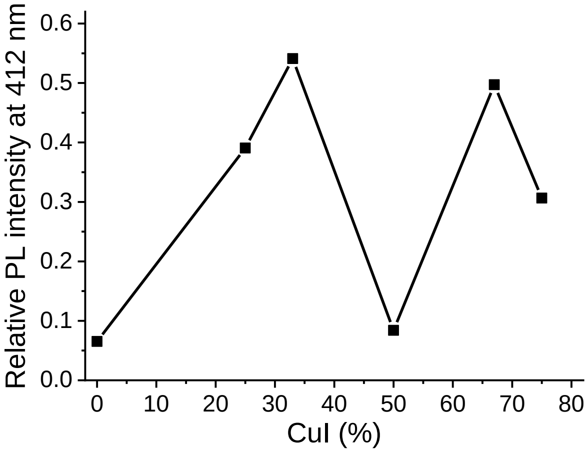

Fig. 75: Relative PL intensity of CuI-PbI_2 nanocomposite electrodes with different molar ratio at 412nm, compared to pure CuI. The lines connecting the data points only serve to guide the eye

5.4.2 PEC behavior of CuI-PbI_2 photoelectrodes

Given the fact that PEC properties highly depend on the morphology and the composition of the photoelectrodes, the CuI-PbI_2 ratio is expected to have a significant effect. PEC studies were carried in aqueous 0.1 M $NaNO_3$ solutions. Linear sweep photovoltammetry curves, recorded for CuI, PbI_2 and CuI-PbI_2 (50-50 %), are shown in **Fig. 76a**. The photocurrents are cathodic in polarity for all samples, indicating a p-type SC behavior. The maximum photocurrent was recorded around +0.61 V vs RHE. The maximum photocurrent is plotted as a function of composition in **Fig. 76b**, where the current peaks at the 1:1 molar ratio of CuI and PbI_2 (1.2-1.5 mA cm^{-2}). This trend is in line with IPCE measurements (see **Fig. 77c**), where the maximum efficiency was recorded also for the equimolar sample (CuI-PbI_2 (50-50 %)). To investigate the thickness dependence of this particular nanocomposite, the loading was varied systematically. The photocurrent increased gradually up to a point (7 mg cm^{-2}) with the increasing loading, and after reaching the maximum, it slowly decreased (refer back in preliminary experiments about loading mass in **Fig. 67b**).

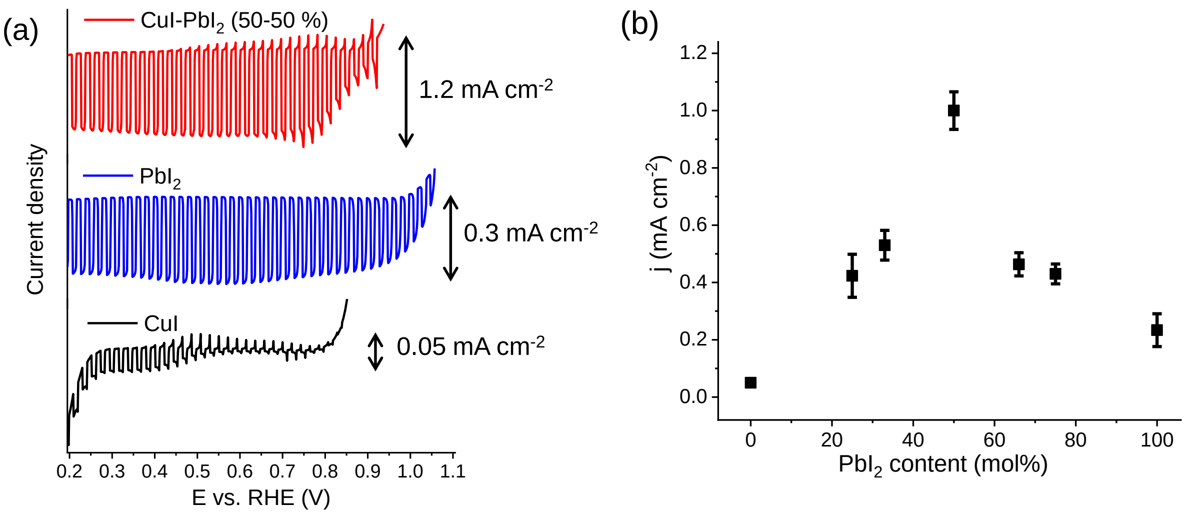

Fig. 76: Linear sweep photovoltammograms recorded for CuI, PbI_2, and CuI-PbI_2 (50-50 %) in Ar saturated 0.1 M $NaNO_3$ solution. The sweep rate was kept at 2 mV s^{-1}, while the light-chopping frequency was 0.2 Hz (a). Maximum current density vs. composition of the nanocomposite samples with error bars from three independent measurements from every composition (b).

The wavelength-dependent PEC behavior of the photoelectrodes was studied by recording photoaction spectra. The lowest IPCE values were obtained for the CuI sample, while the nanocomposite samples showed the highest activity (**Fig. 77a**). The onset of the photocurrent matched with the bandgap for both PbI_2 and CuI. The trend in the IPCE values (recorded at 400 nm) as a function of composition (**Fig. 77c**), mirrored that shown for the photocurrent values in **Fig. 76b**. The IPCE value was zero above 550 nm for CuI and PbI_2, but interestingly, the nanocomposite samples showed a small, yet significant, current response between 575 and 675 nm (**Fig. 77b**). Importantly, the wavelength range for this new PEC activity matches that of the new absorbance feature, showed in **Fig. 72a**.

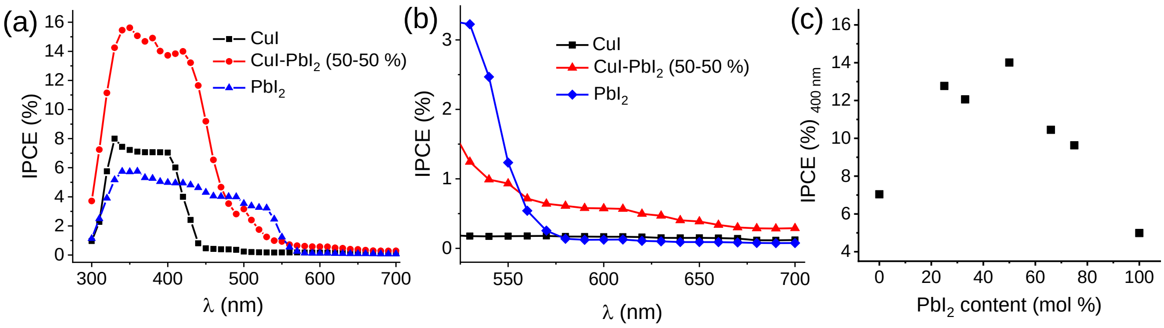

Fig. 77: IPCE curves recorded in 0.1 M $NaNO_3$ for heat treated CuI and PbI_2 and CuI-PbI_2 (50-50 %) photoelectrodes at +0.61 V vs RHE (a), photoresponse of CuI-PbI_2 (50-50 %) at wavelength of light between 500-700 nm (b), IPCE values recorded at 400 nm of all the samples (c).

To summarize and put the PEC results into context, it is worth taking another look at the phase diagram shown in **Fig. 66**. The CuI-PbI_2 (50-50 %) sample gave the largest photocurrent density, where the entire film is made of the stoichiometric γ-CuI – PbI_2 nanocomposite phase (without interruption) in the eutectic point. In the cases of different molar ratios, large γ-CuI and PbI_2 crystals are also present in the films and thus break the continuity of the nanocomposite (**Fig. 71**), explaining the observed volcano curve in **Fig. 76b**.

5.4.3 Long-term photoelectrolysis and product analysis

To explore the stability of the synthesized photoelectrodes, long-term chronoamperometry measurements were performed at three different potentials (+0.46 V, +0.61 V and +0.76 V vs RHE) under periodically interrupted light irradiation (**Fig. 78** and **Fig. 79**). A decrease in photocurrent was observed for both CuI-PbI_2 (50-50 %) and PbI_2, although at different extents. PbI_2 corroded and dissolved rapidly, while in the nanocomposite this process was much slower and reasonable photocurrents were retained in the course of hours. CuI was found to be rather stable, as expected from our precedent results.[134] XRD patterns of photocathodes after photoelectrolysis were recorded to understand the chemical changes, and the *partial* conversion to the respective hydroxides was seen (**Fig. 80**).

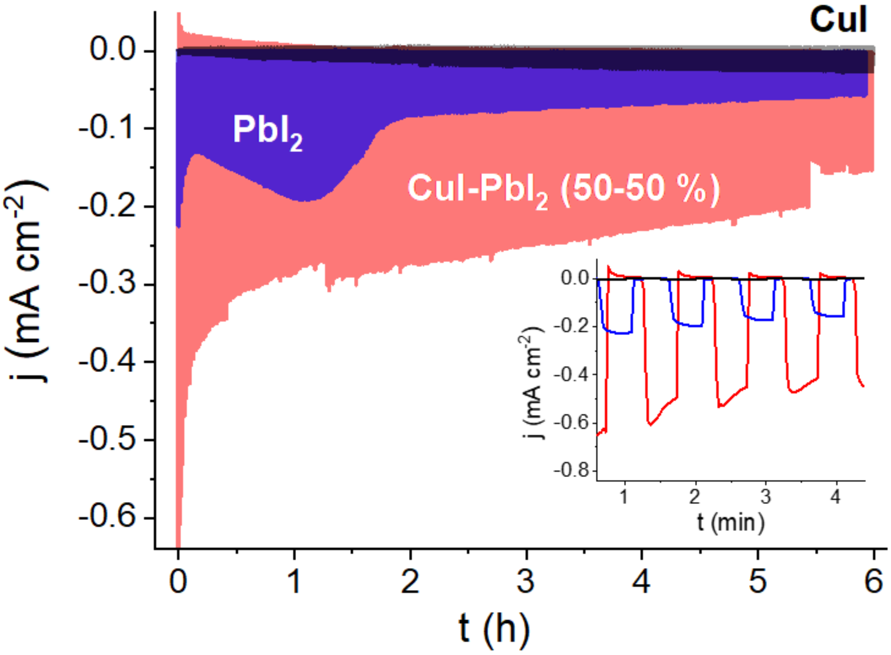

Fig. 78: Long term chronoamperometry analysis of heat-treated CuI, PbI_2 and CuI-PbI_2 (50-50 %) photoelectrodes at +0.61 V vs RHE for 6 hours in 0.1M $NaNO_3$ solution. The inset figure shows chronoamperometric trend of CuI and PbI_2 and CuI-PbI_2 (50-50 %) under chopped light irradiation (0.033 Hz) in the first 4 minute.

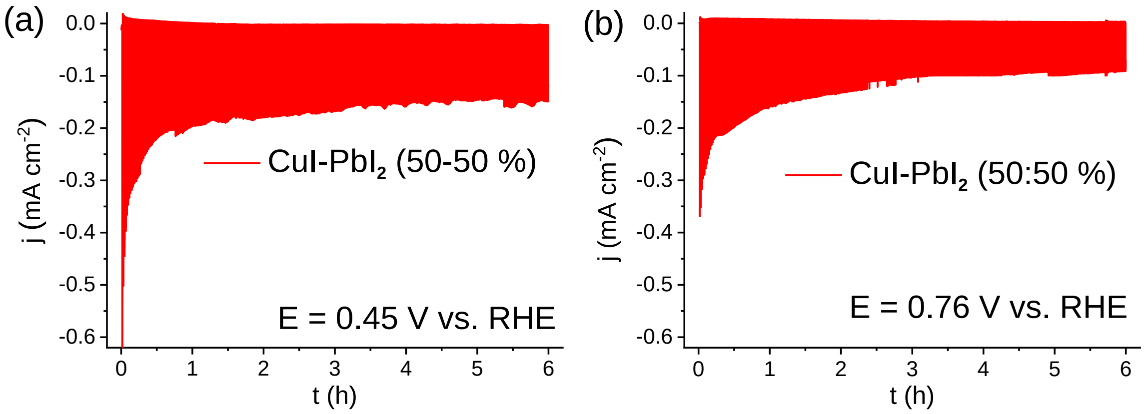

Fig. 79: Long term photoelectrolysis using CuI-PbI$_2$ (50-50 %) at +0.46 V (a) and +0.76 V (b) vs RHE for 6 hours in 0.1M NaNO$_3$ solution.

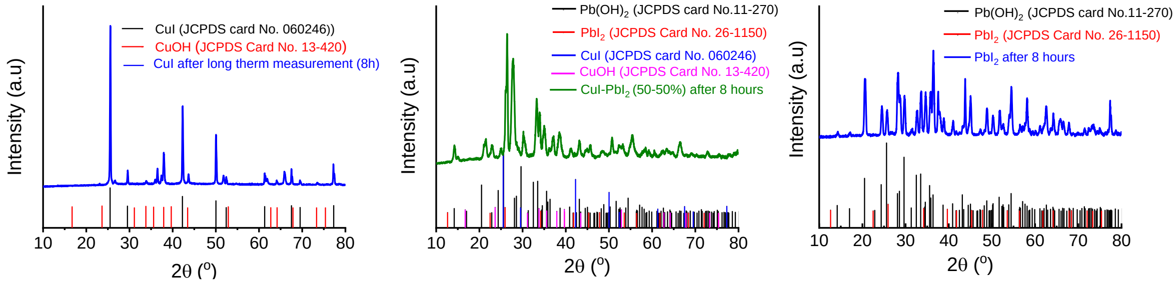

Fig. 80: XRD pattern of CuI, CuI-PbI$_2$ (50-50 %), PbI$_2$ after 6 hours of stability test, with the diffraction lines of possible compounds, based on JCPDS data.

The expected reduction products of nitrate ion are NO_2^-, N_2 and NH_3, together with H_2 from the parasite reaction of water splitting. We quantitatively analyzed the amount of nitrite ions using ion chromatography, whereas colorimetric analysis combined with ^{1}H-NMR was employed for detecting NH_3. GC-MS studies qualitatively confirmed the formation of N_2 gas, while online GC-BID analysis excluded the formation of H_2. Aliquots were taken from the electrolyte before- and 2, 4 and 6 h electrolysis. To accurately quantify the products formed during photoelectrolysis, two control experiments were also carried out: (i) illumination of only the solution in the absence of the electrodes and (ii) an experiment under dark with the electrodes in the solution. No product formation was detected in these cases.

The maximum amount of NO_2^- was produced at +0.61 V vs RHE, with about 50% FE after 4 hours (**Fig. 81a**). The maximum NO_2^- production rate was 0.77 μmol h^{-1} cm^{-2} (2.14×10^{-10} mol s^{-1} cm^{-2}), also observed at this potential, and this rate gradually decreased with time (**Fig. 81b**), coinciding with the observed decrease in the photocurrents (**Fig. 78** and **Fig. 79**). The error bars on the figure confirm the consistency and reproducibility of NO_2^- formation. Notably, all the applied potentials (i.e., +0.46 V, +0.61 V and +0.76 V vs RHE), are below the thermodynamic reduction potential for NO_3^- (–0.02 V vs RHE, see **Fig. 83a** later).

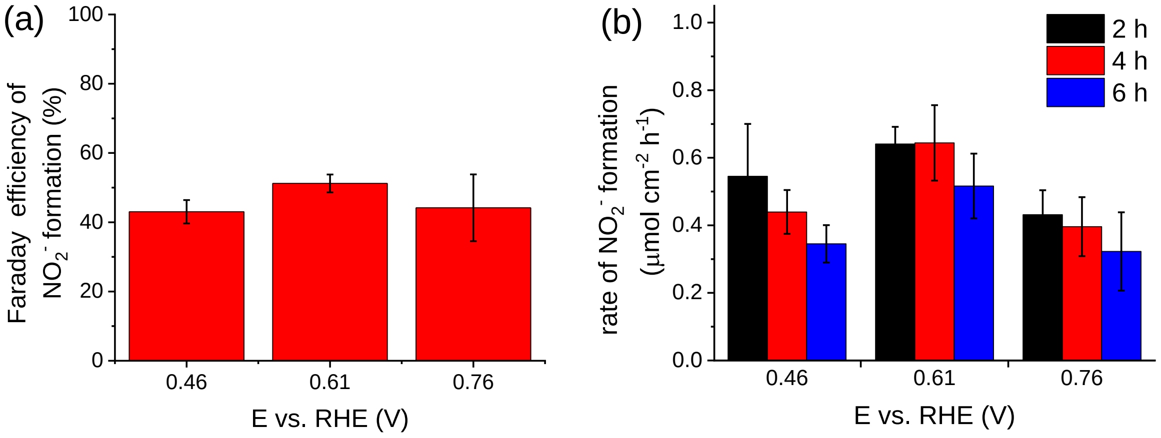

Fig. 81: FE of NO_2^- ion formation after 4 hours during the photoelectrolysis (a) and formation rates with the irradiation time (b) at constant applied potentials (+0.46 V, +0.61 V, +0.76 V vs RHE) on CuI-PbI_2 (50-50 %) photoelectrode in 0.1 M $NaNO_3$ solution.

Colorimetric measurements showed the presence of ammonia in the taken samples, however, in the case when the nitrate ion source was 0.1 M ^{15}N labeled (98%) $Na^{15}NO_3$ solution, ^1H-NMR measurements proved that this ammonia does not come from the reduction of the nitrate ions, but from an external source of contamination.

As another interesting observation, small bubbles were spotted on the surface of the photoelectrodes during photoelectrolysis. On-line GC-BID analysis of the gas phase was performed (with the same equipment in **Fig. 16**) and no H_2 formation was seen in any of these experiments. Therefore, we assumed that the formed bubbles are N_2. Quantitative detection of nitrogen from the gas space is complicated because nitrogen in the air cannot be completely excluded during sampling. As the natural occurrence of ^{15}N in the air is 0.4%, it might also interfere with determining the *exact amount* of evolving nitrogen gas when we started $Na^{15}NO_3$ (98% ^{15}N) solution (Ar saturated, 0.1 M concentration). However, the formation of nitrogen gas during the photoelectrolysis can be *qualitatively* prove with isotope labeling studies: the gas space was sampled and analyzed by GC-MS at various m/z ratios. Airborne interfering nitrogen and its natural ^{15}N isotope is present of 0.4% in the form of $^{15}N^{14}N$ gas, which gives a signal at 29 m/z during GC-MS measurement. As shown in **Fig. 82a**, there is no significant difference between the amounts of $^{14}N^{15}N$ gas sampled from the experiments with labeled and unlabeled nitrate ions, which means that practically nitrogen contamination from the air was measured. However, $^{15}N_2$ molecules (having both nitrogen atoms labeled) have much lower concentration (0.0016%) in the air, so observing a signal from this molecule at 30 m/z can exclude nitrogen gas from interfering air. As shown in **Fig. 82b**, the bubbles formed during photoelectrolysis were exclusively coming from $^{15}N_2$, which can only originate from the reduction of 98% ^{15}N labeled nitrate ions. We think therefore that the missing charge density (i.e., to achieve 100 % total FE) can be partially accounted to N_2 formation (besides the photocorrosion).

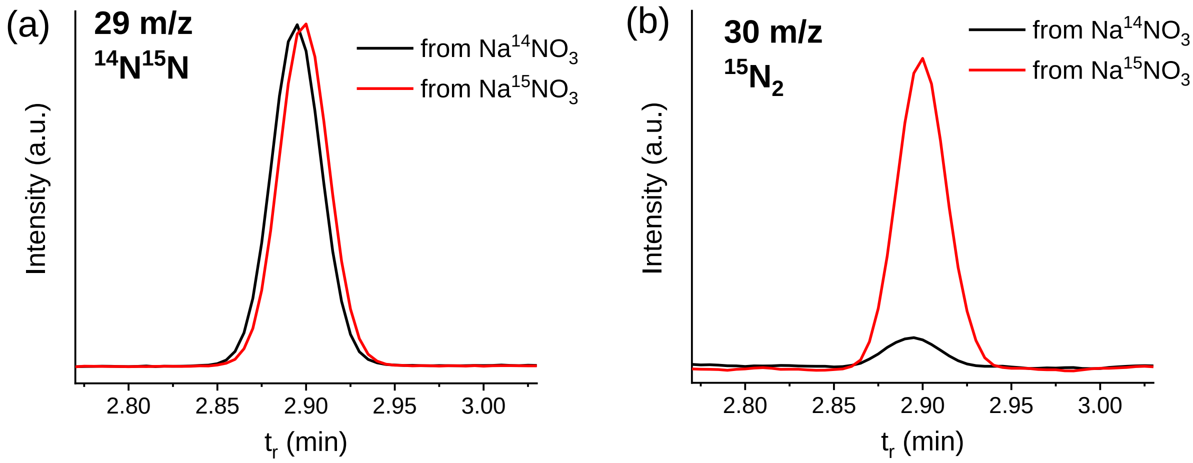

Fig. 82: Isotope labeling experiments to prove qualitative the nitrogen gas formation: signal at 29 m/z during GC-MS measurement (a) from $^{15}N^{14}N$ gas contamination, and signal at 30 m/z (b) which originate from labeled $Na^{15}NO_3$ (98% ^{15}N) reduction into $^{15}N_2$.

5.4.4 Mechanistic insights of the PEC processes on CuI-PbI₂ nanocomposite electrodes

XRD and HR-TEM investigations showed that PbI_2 and CuI do not form any new compound upon heat treatment, instead they retain their individual form in the nanocomposite photoelectrodes. At the same time, a new absorption band at 600 nm was seen for all nanocomposite samples, corresponding to a transition energy of 1.9 eV. Experimental (optoelectronic and IPCE studies) results confirmed that this is related to the transfer of electrons from the VB of CuI to the CB of PbI_2 (**Fig. 83a**). Furthermore, the PL intensity of CuI is completely quenched in the nanocomposite samples, indicating rapid charge carrier separation. This assumption was proven in the PEC studies, where higher photocurrents were recorded for the hybrid photoelectrodes compared to their single component counterparts. The maximum photocurrent was obtained when the composition is 1:1, indicating efficient charge transfer from CuI to PbI_2 in this case.

Various pathways of electron excitation and recombination are illustrated in **Fig. 83b**. Pathways 1 and 2 represent the generation of electron-hole pairs within CuI and PbI_2, respectively. The additional two pathways 3 and 4 are expected to be the reasons behind the improved PEC performance of CuI-PbI_2 hybrids. Excited electrons in the CB of CuI can be transferred to the CB of PbI_2 (3). Along with this event, the electrons in the VB of CuI can be excited to the CB of PbI_2 (4), which are then available for chemical reactions or these excited electrons may recombine with the holes in CuI or PbI_2 (5). This recombination can decrease the performance of CuI-PbI_2 hybrid photoelectrode. Considering the significant improvement in the experienced photocurrent, it can be assumed that pathway 4 is dominant over 5. This additional electron excitation pathway, together with the vertical charge carrier separation in the nanocomposite, play a vital role in improving the performance of hybrid samples.

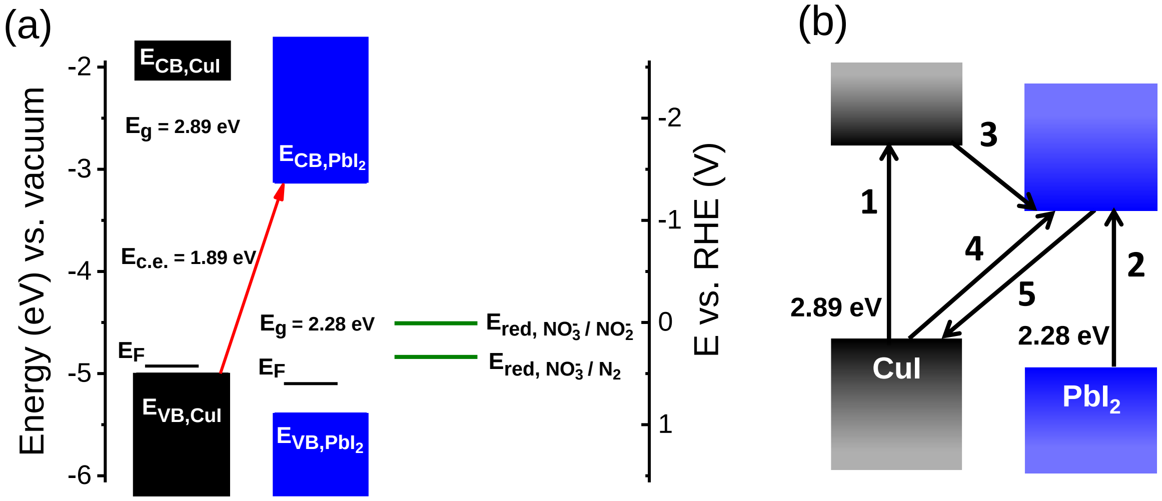

E_g (CuI in literature) = 3.01 eV
E_g (PbI_2 in literature) = 2.20 eV

Fig. 83: Band diagram of CuI and PbI_2 with vacuum energies are set to zero and the reduction potential for NO_2^- and N_2 is set versus RHE (a). Various pathways of electron excitation and recombination within and between CuI and PbI_2 (b).

6. SUMMARY

The first step of my doctoral work was to develop electrochemical methods for preparing SC/nanocarbon photoelectrodes and study their PEC behavior. We investigated different options to homogeneously deposit p-type Cu_2O, n-type TiO_2 and Fe_2O_3 nanocrystals on different nanocarbon electrodes, such as spray-coated CNT and GR film, and 3D-GR. In the second phase of my work, we employed such nanocomposite electrodes in different PEC reactions (i.e., CO_2 reduction and water oxidation). We studied the reasons behind the improved PEC performance of the nanocarbon based photoelectrodes, compared to their bare SC counterparts. We then investigated the synthesis of mixed iodide-based photoelectrodes (using CuI and PbI_2) and studied these composite photoelectrodes in the PEC reduction of NO_3^- ion. We established a possible explanation for why mixed iodide photoelectrodes behave better than the components alone.

The most important results of my doctoral work can be summarized in the following points:

1. A broad compositional and morphological space was explored to assemble hybrid photoelectrodes based on a highly conductive nanocarbon support and a p-type inorganic SC (Cu_2O). A multiple potential-step electrodeposition protocol was developed and employed to control the amount and size of the Cu_2O nanocrystallites on spray-coated CNT, GR and 3D-GR surface. The PEC activity of the composites was proved in CO_2 reduction (to form alcohol products), as a model multi-electron transfer reaction of practical significance. It was found that the GR containing photoelectrodes outperformed the pure Cu_2O, both in terms of the achieved current densities and stability. Composition-dependent PEC studies revealed that there was an optimal loading for both components. Fast transient photocurrent measurements revealed that the main contribution of the GR substrate in such structures was the facilitation of effective charge separation and transport, leading to better harvesting of the generated photoelectrons. An added bonus from this was the enhanced stability and durability of the SC components.
2. A phenomenological model was developed to explain the enhanced PEC behavior involving: 1) electron transfer from Cu_2O to CO_2, 2) recombination of the photoelectrons with holes in the space charge layer (GR), 3) hole transfer from Cu_2O to GR, and 4) hole transport through the electrode architecture to the current

collector. By fitting the transient photocurrent curve, semi-quantitative assessment could be made, for the first time, for the GR contribution to the enhanced PEC activity of the hybrid photoelectrodes. The presented approach also afforded study of the effect of the nanocarbon morphology: after deconvoluting the effect of the increased surface area, we demonstrated that an interconnected 3D-GR structure (as a new promising member of the self-standing, highly conductive carbon derivative family) has further benefits compared to its non-organized counterparts (spray-coated GR and CNT films), because of the lack of carbon-carbon boundaries in the structure.

3. A new method was developed and optimized for the direct synthesis of crystalline TiO_2 on different carbon substrates (GC and GR). This synthetic route consists of one single electrochemical step, resulting in a high quality, porous, nanocrystalline TiO_2 film, in a significantly shorter timeframe than the most frequently applied synthesis procedures (e.g., sol–gel method or flame pyrolysis). The approach is based on the electrochemical oxidation of $TiCl_3$ precursor in an aqueous solution. The crystallinity of the product is ensured by the elevated solution temperature during electrodeposition (proved by TEM, Raman spectroscopy and XRD). The phase composition of the deposit was dependent on the initial pH value of the deposition solution. Therefore, the composition of the TiO_2 films, namely the rutile/anatase ratio, can be controlled and adjusted to a specific targeted application. The electrodeposited layers showed higher photocurrents compared to the Aeroxide P25 reference material. This is rooted in the interconnected structure of the electrodeposited layer, and in the intimate connection between the substrate and the deposited TiO_2 film. TiO_2 was also electrodeposited on GR supports with this developed method but was not observed increase in PEC activity on this composite electrodes. This may be because TiO_2 alone is an excellent photoelectrode material with good charge separation and charge transport behavior that the additional GR scaffold can no longer further enhance.
4. We have shown that electrodeposition allows the synthesis of complex photoelectrode architectures also in the case of Ti-doped α-Fe_2O_3/GR/FTO with precisely controlled structure and composition. Fe_2O_3 was responsible for light absorption, the GR framework ensured proper charge transport, while the FeNiOOH overlayer retained recombination at the surface states through passivation. Photocurrent densities in water oxidation were 2.6 and 1.3 times higher compared to the respective single- and two-component counterparts, and most importantly

exceeded all precedent literature data for electrodeposited hematite based photoelectrodes. Introducing a carbon component to a photoanode, however, raised an additional concern, namely that the photogenerated holes can oxidize the underlying nanocarbon framework (as confirmed by Raman spectroscopy). By adding a third component to the system (i.e., a FeNiOOH overlayer), we were able to suppress the corrosion of the nanocarbon matrix, while all the benefits gained by the presence of GR were still present.

5. We have successfully demonstrated that the mixed CuI-PbI_2 system does not form a new compound, thereby clarifying a contradiction existing in the literature. Also, the possibility of PEC reduction of nitrate to nitrite ion and nitrogen gas was realized on CuI-PbI_2 nanocomposite photoelectrodes, which electrodes were synthesized with a developed thin film melting process. IPCE values up to 15% were realized in a broad wavelength range, while the maximum FE for NO_2^- formation was over 52%. Residual FE is likely linked to N_2 evolution, which was demonstrated by a semi-quantitative isotope labeling method. While the hybrid photocathodes always outperformed than pure CuI and PbI_2 counterparts, the equimolar composition was found to give maximum photocurrent. Detailed optical and PEC studies gave evidence on the possibility of electron transfer from the VB of CuI to the CB of PbI_2 upon illumination, extending the visible light photoactivity of the photoelectrodes. This additional electron excitation, together with the vertical charge carrier separation in the nanocomposite, play a vital role in improving the performance of hybrid samples.

7. ÖSSZEFOGLALÁS

Doktori munkám során első lépésben olyan elektrokémiai leválasztási módszereket dolgoztunk ki, amelyek alkalmasak különböző félvezető/nanoszén kompozit fotoelektródok létrehozására. Különböző elektrokémiai módszereket vizsgáltunk p-típusú Cu_2O, n-típusú TiO_2, valamint egy másik n-típusú félvezető, a Fe_2O_3 nanokristályok létrehozására. A leválasztásokat különböző nanoszén elektród felületeken, spray-coating technikával készült szén-nanocső és grafén filmeken, valamint önhordó 3D grafén rétegen végeztük. Ebben a szakaszban a fő cél az volt, hogy minél egyenletesebb eloszlással és jól szabályozható módon legyünk képesek a kívánt félvezetőt a nanoszén felületére építeni, létrehozva ezzel különböző nanokompozit elektródokat. Munkám második fázisában az így előállított nanokompozit elektródok felhasználását vizsgáltuk különböző fotoelektrokémiai reakciókban, mint például a CO_2 fotoelektrokémiai redukciójában vagy a víz fotoelektrokémiai oxidációjában. A kísérletek során tanulmányoztuk azokat a folyamatokat, amelyek magyarázatot adnak a nanokompozit fotoelektródoknál tapasztalt, a nanoszén nélküli félvezetőhöz képest megnövekedett fotoelektrokémiai aktivitásra. Ezek után tértünk rá a keverék fém-jodid alapú fotoelektródok szintézisére, ahol a két kiválasztott fém-jodid a CuI és az PbI_2 volt. A hőkezeléssel előállított fotoelektródok tulajdonságait nitrát-ion fotoelektrokémiai redukciójában vizsgáltuk. Ezen felül feltérképeztük azokat a folyamatokat, amelyek előidézhetik az előállított CuI/PbI_2 kompozit elektródokban tapasztalt, tiszta komponensekhez képest megnövekedett fotoelektrokémiai aktivitást (különösen az 50-50%-os eutektikus keverék esetében).

Doktori munkám legfontosabb eredményei a következő pontokban foglalhatók össze:

1. Széles összetételi és morfológiai tartományon vizsgáltuk a nagy elektromos vezetőképességű nanoszén alapú kompozit fotoelektródok létrehozásának lehetőségeit, egy p-típusú szervetlen félvezető, a Cu_2O felhasználásával. Egy többlépcsős, potenciál változtatáson alapuló elektrokémiai leválasztási módszert dolgoztunk ki. Ennek segítségével szabályozni tudtuk a spray-coating technikával készült szén-nanocső és grafén filmeken, valamint a 3D grafén elektródok felületén létrehozott Cu_2O nanorészecskék méretét, valamint a borítottság mértékét, egyenletességét. Az így létrehozott Cu_2O/nanoszén kompozit elektródok fotoelektrokémiai aktivitását vizsgáltuk CO_2 redukciójában, ahol a fejlődő termékek (főleg alkoholok) bizonyították a többelektronos átmenettel járó fotoelektrokémiai

reakció lejátszódását. Ezek a mérések azt is megmutatták, hogy a grafén tartalmú kompozit fotoelektródok jobb fotoelektrokémiai teljesítményt nyújtanak, mint a grafén nélküli Cu_2O fotoelektródok. A kompozitok nemcsak az elérhető fotoáramok tekintetében, hanem a stabilitásukban is jobbnak bizonyultak. Vizsgáltuk továbbá a nanokompozitot felépítő komponensek arányának fotoelektrokémiai aktivitásra gyakorolt hatását. Kísérleteink során megállapítottuk, hogy létezik egy optimális fotoelektród összetétel mind a Cu_2O, mint a hordozó grafén mennyiségét tekintve. A gyors fototranziens mérések megmutatták, hogy a kompozitban lévő grafén segíti a töltéshordozók szeparációját és transzportját, amely hatékonyabbá teszi a fotoelektródokon fény hatására keletkező fotoelektronok felhasználását a CO_2 fotoelektrokémiai redukciója során. Továbbá ehhez a jelenséghez köthető a tapasztalt megnövekedett stabilitás is a hosszabb távú fotoelektrolízis során.

2. Egy fenomenológikus modellt fejlesztettünk, amelyben megjelenik: 1) elektron transzfer a Cu_2O-ról a CO_2 molekulára, 2) fotoelektronok rekombinációja a nanoszén felületén, 3) a fotogenerált lyukak mozgása a Cu_2O-ról a nanoszén hordozóra és 4) a lyukak transzportja a nanoszén hordozó elektród struktúrán keresztül a használt áramgyűjtő felületre. Ebből a modellből kiindulva a fototranziens mérési görbékre illesztett, két exponenciális tagot tartalmazó egyenlet segítségével kvázi-kvantitatív módon bemutattuk a megnövekedett fotoelektrokémiai aktivitás okát a grafén tartalmú nanokompozit fotoelektródok esetében. Ennek a módszernek az alkalmazásával hasonlítottuk össze a különböző nanoszén hordozók a kialakított kompozitoktulajdonságaira gyakorolt hatását, a mért fotoáramok nagyságát a hordozó nanoszén elektrokémiailag aktív felületére vonatkoztatva. Az adatok részletes értékelése felfedte, hogy a 3D grafén szerkezetnek (ami egy ígéretes képviselője az öntartó, nagy vezetőképességű szénszármazékoknak) további előnyei vannak a nem rendezett struktúrákkal szemben, mint a spray-coating technikával készült grafén és szén-nanocső filmek. Ennek oka, hogy előbbiben nincsenek fizikai szén-szén kapcsolatok, mint ami tapasztalható két grafénlap vagy két nanocső találkozásánál.
3. Új szintézismódszert fejlesztettünk ki kristályos TiO_2 film létrehozására különböző szén hordozókon (elsődlegesen üvegszénen és spray-coating technikával készült grafén filmeken). Ez az előállítási módszer egy egylépéses elektrokémiai leválasztásból áll ($TiCl_3$ savas oldatának elektrokémiai oxidációja), amely során rövid idő alatt porózus és nanokristályos TiO_2 film hozható létre az adott elektród

felületén. A keletkező TiO_2 film kristályosságát befolyásolja a leválasztási oldat hőmérséklete (ezt transzmissziós elektronmikroszkópiával, Raman spektroszkópiával és Röntgen diffraktometriával is bizonyítottuk). A méréseink ezen túlmenően bizonyították, hogy a leválasztott TiO_2 film fázisösszetételére (rutil/anatáz arány) jelentős hatással van a leválasztásnál használt oldat pH-ja. Az előállított TiO_2 elektródokat tulajdonságait víz fotoelektrokémiai oxidációjában hasonlítottuk össze a referenciaként gyakran használt Aeroxide P25-ből készített elektródokkal és az általunk előállított fotoelektródok esetében nagyobb fotoáramokat mértünk. Ez javarészt ahhoz köthető, hogy az elektrokémiai leválasztás során a keletkező TiO_2 nanokristályok egymással, és a hordozóval is szoros fizikai kapcsolatba kerülnek. Ugyanezzel a módszerrel spray-coating technikával készült grafén film hordozóra választottunk le ugyanazzal a módszerrel TiO_2 nanokristályokat, azonban az így kapott kompozit elektródok fotoelektrokémiai aktivitása nem növekedett a tiszta anyaghoz képest. Ennek magyarázata, hogy a TiO_2 önmagában is egy kiváló fotoelektród alapanyag, amelyben a töltéshordozók szeparálásának és továbbításának mértékét a hozzáadott grafén hordozó réteg már nem tudja tovább növelni.

4. Megmutattuk, hogy elektrokémiai leválasztással jól kontrollálható módon Ti-adalékolt hematit (Fe_2O_3) választható le komplex geometriájú felületre, mint amilyen a spray-coating technikával készült grafén film. Ebben a rendszerben a Fe_2O_3 a fényelnyelő réteg, az alapot képző grafén hordozó film segíti a töltésszeparációt, míg, ha további ko-katalizátor, például FeNiOOH kerül a fotoelektród felületére, az segíti visszaszorítani a rekombinációt a foteolektrokémiai reakció során. Az előállított Fe_2O_3/grafén fotoelektródoknál 2,6-szoros és 1,3-szoros fotoáram növekedést mértünk fotoelektrokémiai vízoxidációs reakcióban (ko-katalizátorral és anélkül), mint a grafén nélküli fotoelektródok esetében. Ezek a fotoáramsűrűségek meghaladják a szakirodalomban ezidáig elektrokémiai leválasztással készült hematit alapú fotoelektródokra közölt értékeket. Azonban a szén hordozó használata egy fotoanódban némi aggodalomra ad okot, ugyanis a fotogenerált lyukak képesek oxidálni a félvezető alatt található nanoszén rétegeket. Ezt a jelenséget Raman spektroszkópiával kombinált hosszú távú fotoelektrolízis mérések során bizonyítottuk. A probléma egy lehetséges megoldásának bemutatása érdekében megfelelő ko-katalizátor réteg felületre történő létrehozásával (elektrokémiai leválasztást használva) képesek voltunk ezt a korróziós effektust visszaszorítani,

miközben a kialakított összetett elektródon továbbra is ki tudtuk használni a grafén hordozó réteg előnyeit annak töltésszeparációban és töltés transzportjában való részvételével. Ezen felül a hozzáadott FeNiOOH réteggel a felületi rekombinációt is jelentősen sikerült csökkenteni, tovább növelve a fotoelektrokémiai aktivitást a vizsgált vízoxidációs reakcióban.

5. Bizonyítottuk, hogy a keverék CuI-PbI_2 rendszer nem képez önálló vegyületet, tisztázva ezzel az irodalomban található egymásnak ellentmondó információkat. Bemutattuk, hogy miként lehet felhasználni az általunk használt vékonyfilm olvasztással készült CuI-PbI_2 kompozit fotoelektródokat nitrát-ion fotoelektrokémiai redukciójában, nitrit-ion és nitrogén gáz keletkezése mellett, hidrogénfejlődés nélkül. A fotoelektrolízis során a mért fotonhasznosítási tényező (IPCE) érték 15% fölötti volt, és 52%-os Faraday hatásfokkal nitrit-ion keletkezett. A maradék töltés valószínűleg nitrogén gáz fejlődésére fordítódik, amely feltevést egy félkvantitatív, izotóp jelzéses módszerrel bizonyítottunk. A kompozit fotoelektródok minden összetétel mellett jobb teljesítményt mutatott a tisztán CuI és PbI_2-ből készült fotoelektródoknál. A legnagyobb fotoáramot az 50-50 n/n%-os összetételű mintáknál mértük, ami egyben a keverék eutektikus pontja is. Részletes optikai és fotoelektrokémiai vizsgálatokkal bizonyítékot találtunk arra vonatkozóan, hogy megvilágítás hatására lehetséges a CuI vegyértéksávjáról a PbI_2 vezetési sávjába történő elektron gerjesztés, amely így szélesíti a létrehozott kompozit fotoelektródok optikai elnyelési tartományt (csökkenti a tiltottsáv-szélességet). Ez a keresztgerjesztés, és a vertikális töltéshordozó szeparációval együtt biztosítja a megnövekedett fotoáramokat ebben a vegyes rendszerben. Míg általánosan a szakirodalomban a fém-halogenid vegyületeket túl instabilnak találják fotoelektródok készítéséhez, a vizsgált CuI-PbI_2 rendszerben ez nem volt jellemző rövid távon, mint ahogy azt a viszonylag stabil 6 órás fotoelektrolízis mérések is bizonyították.

8. REFERENCES

[1] G.W. Crabtree, N.S. Lewis, Solar energy conversion, *Phys. Today.* 60 (2007) 37–42.

[2] British Petroleum (BP), Statistical Review of World Energy report (2020), 69th edition

[3] N. Lewis, D. Nocera, Powering the planet: Chemical challenges in solar energy utilization, *Proc. Natl. Acad. Sci.* 104 (2006) 15729–15735.

[4] A.M. Appel, J.E. Bercaw, A.B. Bocarsly, H. Dobbek, D.L. Dubois, M. Dupuis, J.G. Ferry, E. Fujita, R. Hille, P.J. a Kenis, C. a Kerfeld, R.H. Morris, C.H.F. Peden, A.R. Portis, S.W. Ragsdale, T.B. Rauchfuss, J.N.H. Reek, L.C. Seefeldt, R.K. Thauer, G.L. Waldrop, Frontiers, Opportunities, and Challenges in Biochemical and Chemical Catalysis of CO_2 Fixation., *Chem. Rev.* 113 (2013) 6621–6658.

[5] Y. Tachibana, L. Vayssieres, J.R. Durrant, Artificial photosynthesis for solar water-splitting, *Nat. Photonics.* 6 (2012) 511–518.

[6] J.-W. Jang, S. Cho, G. Magesh, Y.J. Jang, J.Y. Kim, W.Y. Kim, J.K. Seo, S. Kim, K.-H. Lee, J.S. Lee, Aqueous-Solution Route to Zinc Telluride Films for Application to CO_2 Reduction, *Angew. Chemie Int. Ed.* 53 (2014) 5852–5857.

[7] J. Li, N. Wu, Semiconductor-based photocatalysts and photoelectrochemical cells for solar fuel generation: a review, *Catal. Sci. Technol.* 5 (2015) 1360–1384.

[8] M. Kan, D. Yue, J. Jia, Y. Zhao, Photoelectrochemical reduction of nitrates with visible light by nanoporous Si photoelectrode, *Electrochim. Acta.* 177 (2015) 366–369.

[9] H. Wang, J.A. Turner, Photoelectrochemical reduction of nitrates at the illuminated p-$GaInP_2$ photoelectrode, *Energy Environ. Sci.* 6 (2013) 1802–1805.

[10] John A. Dean, ed., Properties of atoms, chemicals and bonds, *Lange's Handb. Chem.*, 15th ed., McGRAW-HILL, INC., (1985) 4.41-4.53.

[11] J.L. White, M.F. Baruch, J.E. Pander, Y. Hu, I.C. Fortmeyer, J.E. Park, T. Zhang, K. Liao, J. Gu, Y. Yan, T.W. Shaw, E. Abelev, A.B. Bocarsly, Light-Driven Heterogeneous Reduction of Carbon Dioxide: Photocatalysts and Photoelectrodes, *Chem. Rev.* 115 (2015) 12888–12935.

[12] B. Kumar, M. Llorente, J. Froehlich, T. Dang, A. Sathrum, C.P. Kubiak, Photochemical and Photoelectrochemical Reduction of CO_2, *Annu. Rev. Phys. Chem.* 63 (2012) 541–569.

[13] J.B. Greenblatt, D.J. Miller, J.W. Ager, F.A. Houle, I.D. Sharp, The technical and energetic challenges of separating (photo)electrochemical carbon dioxide reduction products, *Joule.* 2 (2018) 381–420.

[14] C.M. Sánchez-Sánchez, V. Montiel, D. a. Tryk, A. Aldaz, A. Fujishima, Electrochemical approaches to alleviation of the problem of carbon dioxide accumulation, *Pure Appl. Chem.* 73 (2001) 1917–1927.

[15] H.A. Schwarz, R.W. Dodson, Reduction potentials of CO_2^- and the alcohol radicals, *J. Phys. Chem.* 93 (1989) 409–414.

[16] S. Jin, What Else Can Photoelectrochemical Solar Energy Conversion Do Besides Water Splitting and CO_2 Reduction?, *ACS Energy Lett.* 3 (2018) 2610–2612.

[17] R. Saito, H. Ueno, J. Nemoto, Y. Fujii, A. Izuoka, M. Kaneko, Photoelectrochemical conversion of NO_3^- to N_2 by using a photoelectrochemical cell composed of a nanoporous TiO_2 film photoanode and an O_2 reducing cathode, *Chem. Commun.* (2009) 3231–3233.

[18] J. Choi, J. Choi, H.L. Du, H.L. Du, C.K. Nguyen, C.K. Nguyen, B.H.R. Suryanto, A.N. Simonov, A.N. Simonov, D.R. MacFarlane, D.R. MacFarlane, Electroreduction of Nitrates, Nitrites, and Gaseous Nitrogen Oxides: A Potential Source of Ammonia in Dinitrogen Reduction Studies, *ACS Energy Lett.* 5 (2020) 2095–2097.

[19] Y. Wang, A. Xu, Z. Wang, L. Huang, J. Li, F. Li, J. Wicks, M. Luo, D.H. Nam, C.S. Tan, Y. Ding, J. Wu, Y. Lum, C.T. Dinh, D. Sinton, G. Zheng, E.H. Sargent, Enhanced Nitrate-to-Ammonia Activity on Copper-Nickel Alloys via Tuning of Intermediate Adsorption, *J. Am. Chem. Soc.* 142 (2020) 5702–5708.

[20] Y. Kim, E.B. Creel, E.R. Corson, B.D. McCloskey, J.J. Urban, R. Kostecki, Surface-Plasmon-Assisted Photoelectrochemical Reduction of CO_2 and NO_3^- on Nanostructured Silver Electrodes, *Adv. Energy Mater.* 8 (2018).

[21] C. Roy, J. Deschamps, M.H. Martin, E. Bertin, D. Reyter, S. Garbarino, L. Roué, D. Guay, Identification of Cu surface active sites for a complete nitrate-to-nitrite conversion with nanostructured catalysts, *Appl. Catal. B Environ.* 187 (2016) 399–407.

[22] K. Rajeshwar, A. Thomas, C. Janáky, Photocatalytic Activity of Inorganic Semiconductor Surfaces: Myths, Hype, and Reality, *J. Phys. Chem. Lett.* 6 (2015) 139–147.

[23] P. V. Kamat, Semiconductor surface chemistry as holy grail in photocatalysis and photovoltaics, *Acc. Chem. Res.* 50 (2017) 527–531.

[24] K. Rajeshwar, Electrosynthesized thin films of group II–VI compound semiconductors, alloys and superstructures, *Adv. Mater.* 4 (1992) 23–29.

[25] D. Lincot, Electrodeposition of semiconductors, *Thin Solid Films.* 487 (2005) 40–48.

[26] K. Rajeshwar, N.R. de Tacconi, C.R. Chenthamarakshan, Spatially directed electrosynthesis of semiconductors for photoelectrochemical applications, *Curr. Opin. Solid State Mater. Sci.* 8 (2004) 173–182.

[27] P. Roy, S. Berger, P. Schmuki, TiO_2 nanotubes: synthesis and applications., *Angew. Chemie Int. Ed.* 50 (2011) 2904–2939.

[28] N.R. de Tacconi, C. Chenthamarakshan, G. Yogeeswaran, A. Watcharenwong, R. de Zoysa, N. Basit, K. Rajeshwar, Nanoporous TiO_2 and WO_3 films by anodization of titanium and tungsten substrates: influence of process variables on morphology and photoelectrochemical response., *J. Phys. Chem. B.* 110 (2006) 25347–25355.

[29] C. Janáky, K. Rajeshwar, The role of (photo)electrochemistry in the rational design of hybrid conducting polymer/semiconductor assemblies: From fundamental concepts to practical applications, *Prog. Polym. Sci.* 43 (2015) 96–135.

[30] G. Ghadimkhani, N.R. de Tacconi, W. Chanmanee, C. Janaky, K. Rajeshwar, Efficient solar photoelectrosynthesis of methanol from carbon dioxide using hybrid CuO-Cu_2O semiconductor nanorod arrays, *Chem. Commun.* 49 (2013) 1297–1299.

[31] E.P. Krivan, D. Ungor, C. Janáky, Z. Németh, C. Visy, Optimization of the photoactivity of conducting polymer covered ZnO nanorod composite electrodes, *J. Solid State Electrochem.* 19 (2015) 37–44.

[32] J. Yan, H. Zhou, P. Yu, L. Su, L. Mao, A general electrochemical approach to deposition of metal hydroxide/oxide nanostructures onto carbon nanotubes, *Electrochem. Comm.* 10 (2008) 761–765.

[33] B. Brown, I. a. Cordova, C.B. Parker, B.R. Stoner, J.T. Glass, Optimization of Active Manganese Oxide Electrodeposits Using Graphenated Carbon Nanotube Electrodes for Supercapacitors, *Chem. Mater.* 27 (2015) 2430–2438.

[34] L. Wang, S. Xu, H. Li, Q. Yue, X. Gu, S. Zhang, J. Liu, Carbon Fiber and Electrochemiluminescence of ZnO nanostructures, *Cryst. Eng. Comm.* 15 (2013) 8444–8449.

[35] S. Wu, Z. Yin, Q. He, X. Huang, X. Zhou, H. Zhang, Electrochemical deposition of semiconductor oxides on reduced graphene oxide-based flexible, transparent, and conductive electrodes, *J. Phys. Chem. C.* 114 (2010) 11816–11821.

[36] Y. Zhou, J.A. Switzer, Electrochemical Deposition and Microstructure of Copper (I) Oxide Films,

Scr. Mater. 38 (1998) 1731–1738.

[37] S. Wu, Z. Yin, Q. He, G. Lu, X. Zhou, H. Zhang, Electrochemical deposition of Cl-doped n-type Cu_2O on reduced graphene oxide electrodes, *J. Mater. Chem.* 21 (2011) 3467.

[38] I. Dumitrescu, P.R. Unwin, J. V Macpherson, Electrochemistry at carbon nanotubes: perspective and issues., *Chem. Commun.* 7345 (2009) 6886–6901.

[39] A. Ambrosi, C.K. Chua, A. Bonanni, M. Pumera, Electrochemistry of graphene and related materials., *Chem. Rev.* 114 (2014) 7150–7188.

[40] W.S. Hummers, R.E. Offeman, Preparation of Graphitic Oxide, *J. Am. Chem. Soc.* 80 (1958) 1339.

[41] S. Stankovich, D. a. Dikin, R.D. Piner, K. a. Kohlhaas, A. Kleinhammes, Y. Jia, Y. Wu, S.T. Nguyen, R.S. Ruoff, Synthesis of graphene-based nanosheets via chemical reduction of exfoliated graphite oxide, *Carbon N. Y.* 45 (2007) 1558–1565.

[42] V. Singh, D. Joung, L. Zhai, S. Das, S.I. Khondaker, S. Seal, Graphene based materials: Past, present and future, *Prog. Mater. Sci.* 56 (2011) 1178–1271.

[43] M. Velický, D.F. Bradley, A.J. Cooper, E.W. Hill, I.A. Kinloch, A. Mishchenko, K.S. Novoselov, H. V. Patten, P.S. Toth, A.T. Valota, S.D. Worrall, R.A.W. Dryfe, Electron Transfer Kinetics on Mono- and Multilayer Graphene, *ACS Nano.* 10 (2014) 10089–10100.

[44] B. Marinho, M. Ghislandi, E. Tkalya, C.E. Koning, G. de With, Electrical conductivity of compacts of graphene, multi-wall carbon nanotubes, carbon black, and graphite powder, *Powder Technol.* 221 (2012) 351–358.

[45] C. Janáky, K. Rajeshwar, The Role of (Photo)electrochemistry in the Rational Design of Hybrid Conducting Polymer / Semiconductor Assemblies: From Fundamental Concepts to Practical *Applications, Prog. Polym. Sci.* 43 (2015) 96–135.

[46] J.F. Lin, O. Pitkänen, J. Mäklin, R. Puskas, A. Kukovecz, A. Dombovari, G. Toth, K. Kordas, Synthesis of tungsten carbide and tungsten disulfide on vertically aligned multi-walled carbon nanotube forests and their application as non-Pt electrocatalysts for the hydrogen evolution reaction, *J. Mater. Chem. A.* 3 (2015) 14609–14616.

[47] A. Peigney, C. Laurent, E. Flahaut, R.R. Bacsa, A. Rousset, Specific surface area of carbon nanotubes and bundles of carbon nanotubes, *Carbon N. Y.* 39 (2001) 507–514.

[48] H. Dai, E.W. Wong, C.M. Lieber, Probing Electrical Transport in Nanomaterials: Conductivity of Individual Carbon Nanotubes, *Science* 272 (1996) 523–526.

[49] J. Sánchez-González, a. Macías-García, M.F. Alexandre-Franco, V. Gómez-Serrano, Electrical conductivity of carbon blacks under compression, *Carbon N. Y.* 43 (2005) 741–747.

[50] B. Endrődi, G.F. Samu, D. Fejes, Z. Németh, E. Horváth, A. Pisoni, P.K. Matus, K. Hernádi, C. Visy, C. Forró, C. Janáky, Challenges and rewards of the electrosynthesis of macroscopic aligned carbon nanotube array/conducting polymer hybrid assemblies, *J. Polym. Sci. Part B Polym. Phys.* 53 (2015) 1507–1518.

[51] M. Schlesinger, K. Rajeshwar, N.R. de Tacconi, *Modern Electroplating*, 5th Editio, Wiley-VCH, Hoboken, New Jersey, 2010.

[52] K. Rajeshwar, C. Janaky, W.-Y. Lin, D.A. Roberts, W. Wampler, Photocatalytically prepared metal nanocluster-oxide semiconductor-carbon nanocomposite electrodes for driving multielectron transfer, *J. Phys. Chem. Lett.* 4 (2013) 3468–3478.

[53] Y. Zhao, Y. Hu, Y. Li, H. Zhang, S. Zhang, L. Qu, G. Shi, L. Dai, Super-long aligned TiO_2/carbon nanotube arrays., *Nanotechnology.* 21 (2010) 505702.

[54] J. Yang, L.-C. Jiang, W.-D. Zhang, S. Gunasekaran, A highly sensitive non-enzymatic glucose sensor based on a simple two-step electrodeposition of cupric oxide (CuO) nanoparticles onto multi-walled carbon nanotube arrays., *Talanta.* 82 (2010) 25–33.

[55] S.L. Chou, J.Z. Wang, S.Y. Chew, H.K. Liu, S.X. Dou, Electrodeposition of MnO_2 nanowires on carbon nanotube paper as free-standing, flexible electrode for supercapacitors, *Electrochem. Commun.* 10 (2008) 1724–1727.

[56] B. Xu, M.-L. Ye, Y.-X. Yu, W.-D. Zhang, A highly sensitive hydrogen peroxide amperometric sensor based on MnO_2-modified vertically aligned multiwalled carbon nanotubes., *Anal. Chim. Acta.* 674 (2010) 20–6.

[57] J. Yang, W. De Zhang, S. Gunasekaran, A low-potential, H_2O_2-assisted electrodeposition of cobalt oxide/hydroxide nanostructures onto vertically-aligned multi-walled carbon nanotube arrays for glucose sensing, *Electrochim. Acta.* 56 (2011) 5538–5544.

[58] A. Goyal, A.L.M. Reddy, P.M. Ajayan, Flexible carbon nanotube-Cu_2O hybrid electrodes for Li-ion batteries, *Small.* 7 (2011) 1709–1713.

[59] R. Amade, E. Jover, B. Caglar, T. Mutlu, E. Bertran, Optimization of MnO_2/vertically aligned carbon nanotube composite for supercapacitor application, *J. Power Sources.* 196 (2011) 5779–5783.

[60] J.-S. Ye, Y. Wen, W.-D. Zhang, H.F. Cui, G.Q. Xu, F.-S. Sheu, Electrochemical functionalization of vertically aligned carbon nanotube arrays with molybdenum oxides for the development of a surface-charge-controlled sensor, *Nanotechnology.* 17 (2006) 3994–4001.

[61] L. Li, G. Zhang, L. Chen, H.M. Bi, K.Y. Shi, Ni(NiO)/single-walled carbon nanotubes composite: Synthesis of electro-deposition, gas sensing property for NO gas and density functional theory calculation, *Mater. Res. Bull.* 48 (2013) 504–511.

[62] Y. Liu, D.-P. Wang, Y.-X. Yu, W.-D. Zhang, Preparation and photoelectrochemical properties of functional carbon nanotubes and Ti co-doped Fe_2O_3 thin films, *Int. J. Hydrogen Energy.* 37 (2012) 9566–9575.

[63] H. Kou, L. Jia, C. Wang, Electrochemical deposition of flower-like ZnO nanoparticles on a silver-modified carbon nanotube/polyimide membrane to improve its photoelectric activity and photocatalytic performance, *Carbon N. Y.* 50 (2012) 3522–3529.

[64] C. Zhang, G. Wang, M. Liu, Y. Feng, Z. Zhang, B. Fang, A hydroxylamine electrochemical sensor based on electrodeposition of porous ZnO nanofilms onto carbon nanotubes films modified electrode, *Electrochim. Acta.* 55 (2010) 2835–2840.

[65] C. Liu, Y. Teng, R. Liu, S. Luo, Y. Tang, L. Chen, Q. Cai, Fabrication of graphene films on TiO_2 nanotube arrays for photocatalytic application, *Carbon N. Y.* 49 (2011) 5312–5320.

[66] Y. Zou, I. a. Kinloch, R. a. W. Dryfe, Mesoporous Vertical Co_3O_4 Nanosheet Arrays on Nitrogen-Doped Graphene Foam with Enhanced Charge-Storage Performance, ACS Appl. Mater. Interfaces. 7 (2015), 22831–22838

[67] M.S. Wu, C.J. Lin, C.L. Ho, Multilayered architecture of graphene nanosheets and MnO_2 nanowires as an electrode material for high-performance supercapacitors, *Electrochim. Acta.* 81 (2012) 44–48.

[68] G. Yu, L. Hu, M. Vosgueritchian, H. Wang, X. Xie, J.R. McDonough, X. Cui, Y. Cui, Z. Bao, Solution-processed graphene/MnO_2 nanostructured textiles for high-performance electrochemical capacitors, *Nano Lett.* 11 (2011) 2905–2911.

[69] Z. Yin, S. Wu, X. Zhou, X. Huang, Q. Zhang, F. Boey, H. Zhang, Electrochemical deposition of ZnO nanorods on transparent reduced graphene oxide electrodes for hybrid solar cells, *Small.* 6 (2010) 307–312.

[70] S. Palanisamy, S.-M. Chen, R. Sarawathi, A novel nonenzymatic hydrogen peroxide sensor based on reduced graphene oxide/ZnO composite modified electrode, *Sensors Actuators B Chem.* 166–167 (2012) 372–377.

[71] C. Xu, B.-S. Kim, J.-H. Lee, M. Kim, S.W. Hwang, B.L. Choi, E.K. Lee, J.M. Kim, D. Whang,

Seed-free electrochemical growth of ZnO nanotube arrays on single-layer graphene, *Mater. Lett.* 72 (2012) 25–28.

[72] N.S.A. Aziz, M.R. Mahmood, K. Yasui, A.M. Hashim, Seed/catalyst-free vertical growth of high-density electrodeposited zinc oxide nanostructures on a single-layer graphene., *Nanoscale Res. Lett.* 9 (2014) 95.

[73] L. Jiang, S. Gu, Y. Ding, F. Jiang, Z. Zhang, Facile and novel electrochemical preparation of a graphene-transition metal oxide nanocomposite for ultrasensitive electrochemical sensing of acetaminophen and phenacetin., *Nanoscale.* 6 (2014) 207–14.

[74] I. V Lightcap, P. V Kamat, Graphitic Design: Prospects of Graphene-Based Nanocomposites for Solar Energy Conversion, Storage, and Sensing., *Acc. Chem. Res.* 46 (2013) 2235–2243.

[75] K. Rajeshwar, N.R. De Tacconi, G. Ghadimkhani, W. Chanmanee, C. Janáky, Tailoring copper oxide semiconductor nanorod arrays for photoelectrochemical reduction of carbon dioxide to methanol, *ChemPhysChem.* 14 (2013) 2251–2259.

[76] D.H. Won, C.H. Choi, J. Chung, S.I. Woo, Photoelectrochemical production of formic acid and methanol from carbon dioxide on metal-decorated CuO/Cu_2O-layered thin films under visible light irradiation, *Appl. Catal. B Environ.* 158–159 (2014) 217–223.

[77] X. Ba, L. Yan, S. Huang, J. Yu, X. Xia, Y. Yu, New Way for CO_2 Reduction under Visible Light by a Combination of a Cu Electrode and Semiconductor Thin Film: Cu_2O Conduction Type and Morphology Effect, *J. Phys. Chem. C.* 118 (2014) 24467–24478.

[78] J.F. De Brito, A. Da Silva, A. Cavalheiro, B. Zanoni, Evaluation of the Parameters Affecting the Photoelectrocatalytic Reduction of CO_2 to CH_3OH at Cu/Cu_2O Electrode Evaluation of the Parameters Affecting the Photoelectrocatalytic Reduction of CO_2 to CH_3OH at Cu/Cu_2O Electrode, *Int. J. Electrochem. Sci.* 9 (2014) 5961–5973.

[79] H. Homayon, C. Wilaiwan, N.R. de Tacconi, B.H. Dennis, K. Rajeshwar, Continuous Flow Photoelectrochemical Reactor for Solar Conversion of Carbon Dioxide to Alcohols, *J. Electrochem. Soc.* 162 (2015) E115–E122.

[80] L. Bendavid, E. Carter, CO_2 Adsorption on Cu_2O (111): A DFT+ U and DFT-D Study, *J. Phys. Chem. C.* 117 (2013) 26048–26059.

[81] Z. Zhang, R. Dua, L. Zhang, H. Zhu, H. Zhang, P. Wang, W. Desalination, E. Science, E. Division, P. Sciences, E. Division, S. Arabia, Carbon-Layer-Protected Cuprous Oxide Nanowire Arrays for Efficinet Water Reduction, *ACS Nano.* 7 (2013) 1709–1717.

[82] A. Paracchino, V. Laporte, K. Sivula, M. Grätzel, E. Thimsen, Highly active oxide photocathode for photoelectrochemical water reduction, *Nat. Mater.* 10 (2011) 456–461.

[83] A. Paracchino, N. Mathews, T. Hisatomi, M. Stefik, S.D. Tilley, M. Grätzel, Ultrathin films on copper(I) oxide water splitting photocathodes: a study on performance and stability, *Energy Environ. Sci.* 5 (2012) 8673.

[84] E. Szaniawska, I.A. Rutkowska, E. Seta, I. Tallo, E. Lust, P.J. Kulesza, Photoelectrochemical reduction of CO_2: Stabilization and enhancement of activity of copper(I) oxide semiconductor by over-coating with tungsten carbide and carbide-derived carbons, *Electrochim. Acta.* 341 (2020) 136054.

[85] C.W. Li, M.W. Kanan, CO_2 reduction at low overpotential on Cu electrodes resulting from the reduction of thick Cu_2O films, *J. Am. Chem. Soc.* 134 (2012) 7231–7234.

[86] F.E. Osterloh, Inorganic nanostructures for photoelectrochemical and photocatalytic water splitting., *Chem. Soc. Rev.* (2012).

[87] W.-D. Zhang, B. Xu, L.-C. Jiang, Functional hybrid materials based on carbon nanotubes and metal oxides, *J. Mater. Chem.* 20 (2010) 6383.

[88] J. Young Kim, J.-W. Jang, D. Hyun Youn, J. Yul Kim, E. Sun Kim, J. Sung Lee, Graphene–carbon nanotube composite as an effective conducting scaffold to enhance the photoelectrochemical water oxidation activity of a hematite film, *RSC Adv.* 2 (2012) 9415.

[89] H. Li, X. Zhang, D.R. MacFarlane, Carbon Quantum Dots/Cu2O Heterostructures for Solar-Light-Driven Conversion of CO_2 to Methanol, *Adv. Energy Mater.* 5 (2014) 1401077.

[90] X. An, K. Li, J. Tang, Cu_2O/Reduced Graphene Oxide Composites for the Photocatalytic Conversion of CO_2, *ChemSusChem.* 7 (2014) 1086–1093.

[91] A. Fujishima, K. Honda, Electrochemical photolysis of water at a semiconductor electrode, *Nature.* 238 (1972) 37–38.

[92] M. Grätzel, Dye-sensitized solar cells, *J. Photochem. Photobiol. C Photochem. Rev.* 4 (2003) 145.

[93] A. Kojima, K. Teshima, Y. Shirai, T. Miyasaka, Organometal halide perovskites as visible-light sensitizers for photovoltaic cells, *J. Am. Chem. Soc.* 131 (2009) 6050–6051.

[94] X. Chen, S.S. Mao, Titanium Dioxide Nanomaterials: Synthesis, Properties, Modifications, and Applications, *Chem. Rev.* 107 (2007) 2891–2959.

[95] D.P. Macwan, P.N. Dave, S. Chaturvedi, A review on nano-TiO_2 sol–gel type syntheses and its applications, *J. Mater. Sci.* 46 (2011) 3669–3686.

[96] J.R. McCormick, B. Zhao, S.A. Rykov, H. Wang, J.G. Chen, Thermal Stability of Flame-Synthesized Anatase TiO_2 Nanoparticles, *J. Phys. Chem. B.* 108 (2004) 17398–17402.

[97] A.S. Aricò, P. Bruce, B. Scrosati, J. Tarascon, W. van Schalkwijk, Nanostructured materials for advanced energy conversion and storage devices, *Nat. Mater. 4* (2005) 366–377.

[98] X. Hu, G. Li, J.C. Yu, Design, Fabrication, and Modification of Nanostructured Semiconductor Materials for Environmental and Energy Applications, *Langmuir.* 26 (2010) 3031–3039.

[99] A.B. Couto, F.L. Migliorini, M.R. Baldan, N.G. Ferreira, Titanium Oxide Electrodeposition on Diamond/Ti Electrodes with Different Boron Dopings, *ECS Trans.* 58 (2014) 47–52.

[100] L. Kavan, B. O'Regan, A. Kay, M. Grätzel, Preparation of TiO_2 (anatase) films on electrodes by anodic oxidative hydrolysis of TiCl3, *J. Electroanal. Chem.* 346 (1993) 291–307.

[101] L.-C. Jiang, W.-D. Zhang, Electrodeposition of TiO_2 Nanoparticles on Multiwalled Carbon Nanotube Arrays for Hydrogen Peroxide Sensing, *Electroanalysis.* 21 (2009) 988–993.

[102] S. Patra, C. Andriamiadamanana, M. Tulodziecki, C. Davoisne, P.-L. Taberna, F. Sauvage, Low-temperature electrodeposition approach leading to robust mesoscopic anatase TiO_2 films, *Sci. Rep.* 6 (2016) 21588.

[103] M. Kiyama, T. Akita, Y. Tsutsumi, T. Takada, Formation of titanic oxides of anatase, brookite and rutile by aerial oxidation of titanous solutions, *Chem. Lett.* 1 (1972) 21–24.

[104] K. Wessels, A. Feldhoff, M. Wark, J. Rathousky, T. Oekermann, Low-Temperature Preparation of Crystalline Nanoporous TiO_2 Films by Surfactant-Assisted Anodic Electrodeposition, *Electrochem. Solid-State Lett.* 9 (2006) C93.

[105] N.J. Bell, Y.H. Ng, A. Du, H. Coster, S.C. Smith, R. Amal, Understanding the Enhancement in Photoelectrochemical Properties of Photocatalytically Prepared TiO_2 - Reduced Graphene Oxide Composite, *J. Phys. Chem. C.* 115 (2011) 6004–6009.

[106] A. Kongkanand, R. Martínez Domínguez, P. V. Kamat, Single Wall Carbon Nanotube Scaffolds for Photoelectrochemical Solar Cells. Capture and Transport of Photogenerated Electrons, *Nano Lett.* 7 (2007) 676–680.

[107] W. Li, F. Wang, S. Feng, J. Wang, Z. Sun, B. Li, Y. Li, J. Yang, A.A. Elzatahry, Y. Xia, D. Zhao, Sol–Gel Design Strategy for Ultradispersed TiO_2 Nanoparticles on Graphene for High-Performance Lithium Ion Batteries, J. Am. Chem. Soc. 135 (2013) 18300–18303.

[108] C. Lohaus, A. Klein, W. Jaegermann, Limitation of Fermi level shifts by polaron defect states in hematite photoelectrodes, *Nat. Commun.* 9 (2018) 4309.

[109] S. Amaral Carminati, A. do Nascimento Barbosa, A. Luiz Martins de Freitas, F.L. Freire, F.L. Souza, A.F. Nogueira, Unraveling the role of single layer graphene as overlayer on hematite photoanodes, *J. Catal.* 372 (2019) 109–118.

[110] N. Mirbagheri, D. Wang, C. Peng, J. Wang, Q. Huang, C. Fan, E.E. Ferapontova, Visible Light Driven Photoelectrochemical Water Oxidation by Zn- and Ti-Doped Hematite Nanostructures, *ACS Catal.* 4 (2014) 2006–2015.

[111] B. Klahr, S. Gimenez, F. Fabregat-Santiago, J. Bisquert, T.W. Hamann, Electrochemical and photoelectrochemical investigation of water oxidation with hematite electrodes, *Energy Environ. Sci.* 5 (2012) 7626.

[112] K. Sivula, F. Le Formal, M. Grätzel, Solar Water Splitting: Progress Using Hematite (α-Fe_2O_3) Photoelectrodes, *ChemSusChem.* 4 (2011) 432–449.

[113] C. Li, Z. Luo, T. Wang, J. Gong, Surface, Bulk, and Interface: Rational Design of Hematite Architecture toward Efficient Photo-Electrochemical Water Splitting, *Adv. Mater.* 30 (2018) 1–23.

[114] B. Iandolo, B. Wickman, I. Zorić, A. Hellman, The rise of hematite: origin and strategies to reduce the high onset potential for the oxygen evolution reaction, *J. Mater. Chem. A.* 3 (2015) 16896–16912.

[115] R. Franking, L. Li, M.A. Lukowski, F. Meng, Y. Tan, R.J. Hamers, S. Jin, Facile post-growth doping of nanostructured hematite photoanodes for enhanced photoelectrochemical water oxidation, *Energy Environ. Sci.* 6 (2013) 500–512.

[116] C.A. Mesa, A. Kafizas, L. Francàs, S.R. Pendlebury, E. Pastor, Y. Ma, F. Le Formal, M.T. Mayer, M. Grätzel, J.R. Durrant, Kinetics of Photoelectrochemical Oxidation of Methanol on Hematite Photoanodes, *J. Am. Chem. Soc.* 139 (2017) 11537–11543.

[117] A. Cots, D. Cibrev, P. Bonete, R. Gómez, Hematite Nanorod Electrodes Modified with Molybdenum: Photoelectrochemical Studies, *ChemElectroChem.* 4 (2017) 585–593.

[118] Y. Ling, G. Wang, D.A. Wheeler, J.Z. Zhang, Y. Li, Sn-Doped Hematite Nanostructures for Photoelectrochemical Water Splitting, *Nano Lett.* 11 (2011) 2119–2125.

[119] S.D. Tilley, M. Cornuz, K. Sivula, M. Grätzel, Light-inducedwater splitting with hematite: Improved nanostructure and iridium oxide catalysis, *Angew. Chemie - Int. Ed.* 49 (2010) 6405–6408.

[120] F. Meng, J. Li, S.K. Cushing, J. Bright, M. Zhi, J.D. Rowley, Z. Hong, A. Manivannan, A.D. Bristow, N. Wu, Photocatalytic Water Oxidation by Hematite/Reduced Graphene Oxide Composites, *ACS Catal.* 3 (2013) 746–751.

[121] S. Do Amaral Carminati, F.L. Souza, A.F. Nogueira, Enhancing Hematite Photoanode Activity for Water Oxidation by Incorporation of Reduced Graphene Oxide, *ChemPhysChem.* 17 (2016) 170–177.

[122] S. Rai, A. Ikram, S. Sahai, S. Dass, R. Shrivastav, V.R. Satsangi, Morphological, optical and photoelectrochemical properties of Fe_2O_3-GNP composite thin films, *RSC Adv.* 4 (2014) 17671–17679.

[123] B.Y. Yu, S.Y. Kwak, Carbon quantum dots embedded with mesoporous hematite nanospheres as efficient visible light-active photocatalysts, *J. Mater. Chem.* 22 (2012) 8345–8353.

[124] J. Deng, X. Lv, H. Zhang, B. Zhao, X. Sun, J. Zhong, Loading the FeNiOOH cocatalyst on Pt-modified hematite nanostructures for efficient solar water oxidation, *Phys. Chem. Chem. Phys.* 18 (2016) 10453–10458.

[125] A.G. Tamirat, W.-N. Su, A.A. Dubale, H.-M. Chen, B.-J. Hwang, Photoelectrochemical water splitting at low applied potential using a NiOOH coated codoped (Sn, Zr) α-Fe_2O_3 photoanode, *J. Mater. Chem. A.* 3 (2015) 5949–5961.

[126] J.E. Thorne, J.W. Jang, E.Y. Liu, D. Wang, Understanding the origin of photoelectrode performance enhancement by probing surface kinetics, *Chem. Sci.* 7 (2016) 3347–3354.

[127] T.H. Jeon, G. Moon, H. Park, W. Choi, Ultra-efficient and durable photoelectrochemical water oxidation using elaborately designed hematite nanorod arrays, *Nano Energy.* 39 (2017) 211–218.

[128] X. Guo, L. Wang, Y. Tan, Hematite nanorods Co-doped with Ru cations with different valence states as high performance photoanodes for water splitting, *Nano Energy.* 16 (2015) 320–328.

[129] P. Peerakiatkhajohn, J.-H. Yun, H. Chen, M. Lyu, T. Butburee, L. Wang, Stable Hematite Nanosheet Photoanodes for Enhanced Photoelectrochemical Water Splitting, *Adv. Mater.* 28 (2016) 6405–6410.

[130] D.H. Fabini, J.G. Labram, A.J. Lehner, J.S. Bechtel, H.A. Evans, A. Van Der Ven, F. Wudl, M.L. Chabinyc, R. Seshadri, Main-Group Halide Semiconductors Derived from Perovskite: Distinguishing Chemical, Structural, and Electronic Aspects, *Inorg. Chem.* 56 (2017) 11–25.

[131] G.F. Samu, R.A. Scheidt, P. V. Kamat, C. Janáky, Electrochemistry and Spectroelectrochemistry of Lead Halide Perovskite Films: Materials Science Aspects and Boundary Conditions, *Chem. Mater.* 30 (2018) 561–569.

[132] H.Y. Hsu, L. Ji, M. Du, J. Zhao, E.T. Yu, A.J. Bard, Optimization of PbI_2/$MAPbI_3$ Perovskite Composites by Scanning Electrochemical Microscopy, *J. Phys. Chem. C.* 120 (2016) 19890–19895.

[133] T. Baran, S. Wojtyła, A. Dibenedetto, M. Aresta, W. Macyk, Photocatalytic Carbon Dioxide Reduction at p-Type Copper(I) Iodide, *ChemSusChem.* 9 (2016) 2933–2938.

[134] Á. Balog, G.F. Samu, P. V. Kamat, C. Janáky, Optoelectronic Properties of CuI Photoelectrodes, *J. Phys. Chem. Lett.* 10 (2019) 259–264.

[135] P.A. Beckmann, A review of polytypism in lead iodide, *Cryst. Res. Technol.* 45 (2010) 455–460.

[136] D. Tiwari, D.J. Fermin, Textured PbI_2 photocathodes obtained by gas phase anion replacement, *Electrochim. Acta.* 254 (2017) 223–229.

[137] T. Kuku, Electrical conductivity of $CuSnI_3$, $CuPbI_3$ and $KPbI_3$, *Solid State Ionics.* 25 (1987) 1–7.

[138] T.. Kuku, Ionic transport and galvanic cell discharge characteristics of $CuPbI_3$ thin films, *Thin Solid Films.* 325 (1998) 246–250.

[139] R. Naeem, R. Yahya, M.A. Mansoor, M.A.M. Teridi, M. Sookhakian, A. Mumtaz, M. Mazhar, Photoelectrochemical water splitting over mesoporous $CuPbI_3$ films prepared by electrophoretic technique, *Monatshefte Fur Chemie.* 148 (2017) 981–989.

[140] T. Takahashi, O. Yamamoto, H. Takahashi, Phase diagrams of the coper(I) bromide-lead bromide and copper (I) iodide-lead iodide systems and the ionic conductivity of $CuPb_3Br_7$, *J. Solid State Chem.* 21 (1977) 37–42.

[141] W.N. Wang, J. Soulis, Y. Jeffrey Yang, P. Biswas, Comparison of CO_2 photoreduction systems: A review, *Aerosol Air Qual. Res.* 14 (2014) 533–549.

[142] W. Tu, Y. Zhou, Z. Zou, Photocatalytic Conversion of CO_2 into Renewable Hydrocarbon Fuels: State-of-the-Art Accomplishment, Challenges, and Prospects, *Adv. Mater.* 26 (2014) 4607–4626.

[143] A. Sápi, A. Varga, G.F. Samu, D. Dobó, K.L. Juhász, B. Takács, E. Varga, Á. Kukovecz, Z. Kónya, C. Janáky, Photoelectrochemistry by Design: Tailoring the Nanoscale Structure of Pt/NiO Composites Leads to Enhanced Photoelectrochemical Hydrogen Evolution Performance, *J. Phys. Chem. C.* 121 (2017) 12148–12158.

[144] R. Hinogami, Y. Nakamura, S. Yae, Y. Nakato, An Approach to Ideal Semiconductor Electrodes for Efficient Photoelectrochemical Reduction of Carbon Dioxide by Modification with Small Metal Particles, *J. Phys. Chem. B.* 102 (1998) 974–980.

[145] D. Fejes, Z. Pápa, E. Kecsenovity, B. Réti, Z. Toth, K. Hernadi, Super growth of vertically aligned carbon nanotubes on pulsed laser deposited catalytic thin films, *Appl. Phys. A.* 118 (2015) 855–861.

[146] Y. Zou, I.A. Kinloch, R.A.W. Dryfe, Mesoporous Vertical Co_3O_4 Nanosheet Arrays on Nitrogen-Doped Graphene Foam with Enhanced Charge-Storage Performance, *ACS Appl. Mater. Interfaces.* 7 (2015) 22831–22838.

[147] L.C. Wang, N.R. de Tacconi, C.R. Chenthamarakshan, K. Rajeshwar, M. Tao, Electrodeposited copper oxide films: Effect of bath pH on grain orientation and orientation-dependent interfacial behavior, *Thin Solid Films.* 515 (2007) 3090–3095.

[148] R. Schrebler, K. Bello, F. Vera, P. Cury, E. Muñoz, R. del Río, H. Gómez Meier, R. Córdova, E.A. Dalchiele, An Electrochemical Deposition Route for Obtaining α-Fe_2O_3 Thin Films, *Electrochem. Solid-State Lett.* 9 (2006) C110.

[149] W. Melitz, J. Shen, A.C. Kummel, S. Lee, Kelvin probe force microscopy and its application, *Surf. Sci. Rep.* 66 (2011) 1–27.

[150] I.D. Baikie, A.C. Grain, J. Sutherland, J. Law, Ambient pressure photoemission spectroscopy of metal surfaces, *Appl. Surf. Sci.* 323 (2014) 45–53.

[151] K. Rajeshwar, Electron transfer at semiconductor–electrolyte interfaces, V. Balzani (Ed.), *Electron Transf. Chem.*, Wiley- VCH, Weinheim, 2001.

[152] Z. Chen, T.G. Deutsch, H.N. Dinh, K. Domen, K. Emery, A.J. Forman, N. Gaillard, R. Garland, C. Heske, T.F. Jaramillo, A. Kleiman-Shwarsctein, E. Miller, K. Takanabe, J. Turner, *Photoelectrochemical Water Splitting*, Springer, 2013.

[153] S. Sahoo, G. Karthikeyan, G.C. Nayak, C.K. Das, Electrochemical characterization of in situ polypyrrole coated graphene nanocomposites, *Synth. Met.* 161 (2011) 1713–1719.

[154] Y. Ma, S.R. Pendlebury, A. Reynal, F. Le Formal, J.R. Durrant, Dynamics of photogenerated holes in undoped $BiVO_4$ photoanodes for solar water oxidation, *Chem. Sci.* 5 (2014) 2964.

[155] F. Le Formal, S.R. Pendlebury, M. Cornuz, S.D. Tilley, M. Grätzel, J.R. Durrant, Back Electron–Hole Recombination in Hematite Photoanodes for Water Splitting, *J. Am. Chem. Soc.* 136 (2014) 2564–2574.

[156] M. Kalaji, L. Nyholm, L.M. Peter, A.J. Rudge, Photoelectrochemical properties of polyaniline films, *J. Electroanal. Chem. Interfacial Electrochem.* 310 (1991) 113–126.

[157] V. Noack, H. Weller, A. Eychmuller, Electron Transport in Particulate ZnO Electrodes : A Simple Approach, *J. Phys. Chem. B.* 106 (2002) 8514–8523.

[158] Y. Zhao, R. Shi, X. Bian, C. Zhou, Y. Zhao, S. Zhang, F. Wu, G.I.N. Waterhouse, L.Z. Wu, C.H. Tung, T. Zhang, Ammonia Detection Methods in Photocatalytic and Electrocatalytic Experiments: How to Improve the Reliability of NH_3 Production Rates?, *Adv. Sci.* 6 (2019).

[159] M. Huang, T. Wang, W. Chang, J. Lin, C. Wu, I.-C. Chen, K. Peng, S. Lee, Temperature dependence on p-Cu_2O thin film electrochemically deposited onto copper substrate, *Appl. Surf. Sci.* 301 (2014) 369–377.

[160] H. Zhang, Q. Zhu, Y. Zhang, Y. Wang, L. Zhao, B. Yu, One-Pot Synthesis and Hierarchical Assembly of Hollow Cu_2O Microspheres with Nanocrystals-Composed Porous Multishell and Their Gas-Sensing Properties, *Adv. Funct. Mater.* 17 (2007) 2766–2771.

[161] X. Cao, Z. Yin, H. Zhang, Three-Dimensional Graphene Materials: Preparation, Structures and Application in Supercapacitors, *Energy Environ. Sci.* 7 (2014) 1850–1865.

[162] M.A. Dar, Y.S. Kim, W.B. Kim, J.M. Sohn, H.S. Shin, Structural and magnetic properties of CuO nanoneedles synthesized by hydrothermal method, *Appl. Surf. Sci.* 254 (2008) 7477–7481.

[163] A.C. Ferrari, J.C. Meyer, V. Scardaci, C. Casiraghi, M. Lazzeri, F. Mauri, S. Piscanec, D. Jiang, K.S. Novoselov, S. Roth, A.K. Geim, Raman spectrum of graphene and graphene layers, *Phys. Rev. Lett.* 97 (2006) 187401–187404.

[164] L.M. Malard, M.A. Pimenta, G. Dresselhaus, M.S. Dresselhaus, Raman spectroscopy in graphene, *Phys. Rep.* 473 (2009) 51–87.

[165] Y. Nakano, S. Saeki, T. Morikawa, Optical bandgap widening of p-type Cu_2O films by nitrogen doping, *Appl. Phys. Lett.* 94 (2009) 022111.

[166] E. Gao, W. Wang, M. Shang, J. Xu, Synthesis and enhanced photocatalytic performance of graphene-Bi_2WO_6 composite, *Phys. Chem. Chem. Phys.* 13 (2011) 2887–2893.

[167] A. Paracchino, J.C. Brauer, J.E. Moser, E. Thimsen, M. Graetzel, Synthesis and characterization of high-photoactivity electrodeposited Cu_2O solar absorber by photoelectrochemistry and ultrafast spectroscopy, *J. Phys. Chem. C.* 116 (2012) 7341–7350.

[168] C. Janaky, D. Hursán, B. Endrodi, W. Chanmanee, D. Roy, D. Liu, N.R. De Tacconi, B.H. Dennis, K. Rajeshwar, Electro- and Photoreduction of Carbon Dioxide : The Twain Shall Meet at Copper Oxide/Copper Nanocube Interfaces, *ACS Energy Lett.* 1 (2016) 332–338.

[169] J.F. de Brito, A.R. Araujo, K. Rajeshwar, M.V.B. Zanoni, Photoelectrochemical reduction of CO_2 on Cu/Cu_2O films: Product distribution and pH effects, *Chem. Eng. J.* 264 (2015) 302–309.

[170] L.M. Peter, Dynamic Aspects of Semiconductor Photoelectrochemistry, *Chem. Rev.* 90 (1990) 753.

[171] Y.C. Pu, H.Y. Chou, W.S. Kuo, K.H. Wei, Y.J. Hsu, Interfacial charge carrier dynamics of cuprous oxide-reduced graphene oxide (Cu_2O-rGO) nanoheterostructures and their related visible-light-driven photocatalysis, *Appl. Catal. B Environ.* 204 (2017) 21–32.

[172] O. Hansen, B. Seger, P.C.K. Vesborg, I. Chorkendorff, A quick look at how photoelectrodes work, *Science* (80-.). 350 (2015) 1030–1031.

[173] T. Nagaoka, T. Sakai, K. Ogura, T. Yoshino, Oxygen reduction at electrochemically treated glassy carbon electrodes, *Anal. Chem.* 58 (1986) 1953–1955.

[174] M.S.S. Dresselhaus, G. Dresselhaus, R. Saito, A. Jorio, Raman spectroscopy of carbon nanotubes, *Phys. Rep.* 409 (2005) 47–99.

[175] H. Cheng, J. Ma, Z. Zhao, L. Qi, Hydrothermal Preparation of Uniform Nanosize Rutile and Anatase Particles, *Chem. Mater.* 7 (1995) 663–671.

[176] Á. Veres, J. Ménesi, C. Janáky, G.F. Samu, M.K. Scheyer, Q. Xu, F. Salahioglu, M. V. Garland, I. Dékány, Z. Zhong, New insights into the relationship between structure and photocatalytic properties of TiO_2 catalysts, *RSC Adv.* 5 (2015) 2421–2428.

[177] K. Shankar, J.I. Basham, N.K. Allam, O.K. Varghese, G.K. Mor, X. Feng, M. Paulose, J. a Seabold, K. Choi, C. a Grimes, Recent Advances in the Use of TiO_2 Nanotube and Nanowire Arrays for Oxidative Photoelectrochemistry, *J. Phys. Chem. C.* 113 (2009) 6327–6359.

[178] M. Radecka, M. Rekas, A. Trenczek-Zajac, K. Zakrzewska, Importance of the band gap energy and flat band potential for application of modified TiO_2 photoanodes in water photolysis, *J. Power Sources.* 181 (2008) 46–55.

[179] O. Zandi, A.R. Schon, H. Hajibabaei, T.W. Hamann, Enhanced Charge Separation and Collection in High-Performance Electrodeposited Hematite Films, *Chem. Mater.* 28 (2016) 765–771.

[180] A.C. Ferrari, D.M. Basko, Raman spectroscopy as a versatile tool for studying the properties of graphene., *Nat. Nanotechnol.* 8 (2013) 235–46.

[181] A.M. Jubb, H.C. Allen, Vibrational Spectroscopic Characterization of Hematite, Maghemite, and Magnetite Thin Films Produced by Vapor Deposition, *ACS Appl. Mater. Interfaces.* 2 (2010) 2804–2812.

[182] J.-B. Wu, M.-L. Lin, X. Cong, H.-N. Liu, P.-H. Tan, Raman spectroscopy of graphene-based materials and its applications in related devices, *Chem. Soc. Rev.* 47 (2018) 1822–1873.

[183] Z. Huang, Y. Lin, X. Xiang, W. Rodríguez-Córdoba, K.J. McDonald, K.S. Hagen, K.-S. Choi, B.S. Brunschwig, D.G. Musaev, C.L. Hill, D. Wang, T. Lian, In situ probe of photocarrier dynamics in water-splitting hematite (α-Fe_2O_3) electrodes, *Energy Environ. Sci.* 5 (2012) 8923.

[184] G. Wang, X. Shen, J. Yao, J. Park, Graphene nanosheets for enhanced lithium storage in lithium ion batteries, *Carbon N. Y. 47* (2009) 2049–2053.

[185] P. Makuła, M. Pacia, W. Macyk, How To Correctly Determine the Band Gap Energy of Modified Semiconductor Photocatalysts Based on UV–Vis Spectra, *J. Phys. Chem. Lett.* 9 (2018) 6814–6817.

[186] J. Tauc, Optical properties and electronic structure of amorphous Ge and Si, *Mater. Res. Bull.* 3 (1968) 37–46.

[187] Y.W. Phuan, W.-J. Ong, M.N. Chong, J.D. Ocon, Prospects of electrochemically synthesized hematite photoanodes for photoelectrochemical water splitting: A review, *J. Photochem. Photobiol. C Photochem. Rev.* 33 (2017) 54–82.

[188] Gurudayal, P.S. Bassi, T. Sritharan, L.H. Wong, Recent progress in iron oxide based photoanodes for solar water splitting, *J. Phys. D. Appl. Phys.* 51 (2018) 473002.

[189] S.H. Aboutalebi, A.T. Chidembo, M. Salari, K. Konstantinov, D. Wexler, H.K. Liu, S.X. Dou, Comparison of GO, GO/MWCNTs composite and MWCNTs as potential electrode materials for supercapacitors, *Energy Environ. Sci.* 4 (2011) 1855.

[190] J.G. Radich, A.L. Krenselewski, J. Zhu, P. V Kamat, Is Graphene a Stable Platform for Photocatalysis? Mineralization of Reduced Graphene Oxide With UV-Irradiated TiO_2 Nanoparticles, *Chem. Mater.* 26 (2014) 4662–4668.

[191] J.G. Radich, P. V. Kamat, Making Graphene Holey. Gold-Nanoparticle-Mediated Hydroxyl Radical Attack on Reduced Graphene Oxide, *ACS Nano.* 7 (2013) 5546–5557.

[192] A. Tsyganok, D. Klotz, K.D. Malviya, A. Rothschild, D.A. Grave, Different Roles of $Fe_{1-x}Ni_xOOH$ Cocatalyst on Hematite (α-Fe_2O_3) Photoanodes with Different Dopants, *ACS Catal.* 8 (2018) 2754–2759.

[193] K. George, X. Zhang, A. Bieberle-Hütter, Why does NiOOH cocatalyst increase the oxygen evolution activity of α-Fe_2O_3?, *J. Chem. Phys.* 150 (2019) 041729.

[194] B. Sharma, M.K. Rabinal, Ambient synthesis and optoelectronic properties of copper iodide semiconductor nanoparticles, *J. Alloys Comp.* 556 (2013) 198–202.

[195] X.H. Zhu, B.J. Zhao, S.F. Zhu, Y.R. Jin, Z.Y. He, J.J. Zhang, Y. Huang, Synthesis and characterization of PbI_2 polycrystals, *Cryst. Res. Technol.* 41 (2006) 239–242.

[196] P. Gao, M. Gu, X.L. Liu, B. Liu, S.M. Huang, X-ray excited luminescence of cuprous iodide single crystals: On the nature of red luminescence, *Appl. Phys. Lett.* 95 (2009).

ACKNOWLEDGEMENT

I am grateful to the Head of Department of Physical Chemistry and Materials Science, **Prof. Dr. Ágota Tóth**, for allowing me to carry out my doctoral work at the department.

I would like to thank my supervisor, **Dr. Csaba Janáky** for his help and support during the years spent in the research group. I am also grateful for the opportunity to try myself in several topics beyond my doctoral work, through which I was able to broaden my knowledge, my views. I would also like to thank him for allowing and supporting my participation in international conferences with my professional development in mind.

I am grateful to **Prof. Krishnan Rajeshwar** for his advices and proofreading of the manuscripts during my doctoral work.

I would like to thank **Dr. Balázs Endrődi**, who taught me the various photoelectrochemical techniques at the beginning of my doctoral work and with whom I worked on titanium dioxide electrodeposition. Also, thanks for being available at any time to answer my quick questions.

I would like to thank **Dr. Attila Kormányos** for performing the SEM measurements and for the successful collaboration on the hematite / nanocarbon photoelectrode topic.

I am grateful to **Dr. Saji Thomas Kochuveedu** for her contribution on the mixed metal iodide topic.

I would like to thank **Dr. Gergely Ferenc Samu** for his help with XPS measurements and evaluation and for creating the TEM lamellae during the mixed metal iodide research. Also, thanks for the sometimes lengthy professional conversations, from which I learned a lot.

Many thanks to the former and current members of the research group for all their help and for providing an honest, friendly, and creative working environment. I would like to highlight **Dr. Dorottya Hursán**, **Dr. Ádám Balog**, **Dr. Péter Sándor Tóth, Dr. Gábor Bencsik, Katalin Sziveri, Dr. Ahmed Mohnsen Ismail** who helped me in some way with my work; during some measurements, ordering chemicals, management, or by practicing English with me daily.

I owe thanks to **Prof. Klára Hernádi**, my former supervisor, for introducing me to the world of scientific research, supporting me, and providing opportunities for development during my early university years.

I am also grateful to my partner, **Tamara**, who stood by me throughout my doctoral work, supported and encouraged me even in the hardest moments.

Finally, I owe many thanks to my family: **my parents** and my **sister**. You helped me to always stand on the ground with both feet, and you have given me full support in my decisions. I am especially grateful that you have provided a peaceful environment that I can call my home and where I can retreat to recharge at any time.